Lussac Prestes Maia

Environmental model-based time-reversal underwater communications

University of Algarve

Faculty of Sciences and Technology

2017

Lussac Prestes Maia

Environmental model-based time-reversal underwater communications

PhD. Thesis in Electronics and Telecomunications (Signal Processing)

Developed under supervision of:

Prof. Doutor Sérgio Manuel Machado Jesus

Prof. Doutor António João Freitas Gomes da Silva

University of Algarve

Faculty of Sciences and Technology

2017

Environmental model-based time-reversal underwater communications

Declaração de autoria do trabalho

Declaro ser o autor deste trabalho, que é original e inédito. Autores e trabalhos consultados estão devidamente citados no texto e constam da listagem de referências bibliográficas incluída.

Lussac Prestes Maia

À querida Jorgia

Ao meu filho Theo

&

Aos meus pais

Acknowledgements

I would like to thank all those who somehow helped me to get this research work done. In particular I acknowledge for the contributions of my supervisors Prof. Sérgio and Prof. António. The discussions I had with them over these four years in the UAlg generated valuable advise and guidance, which contributed to my effort to better understand the most important issues of ocean acoustic propagation in the scope of digital communications. Their large experience both in academic subjects as well as in operational tasks at sea helped me to develop this research work. Thank you.

Thanks to my colleagues of the Signal Processing Laboratory, members and ex-members, for your friendship and good talks: Nelson Martins, Ana Bela, Rogério Calazans, Dymtro Maslov, Agni Mantouka, Cristiano Soares, Friedrich Zabel, Paulo Santos, Orlando Rodriguez e Paulo Felisberto. It was great to have been part of the SiPLAB team.

I would like to thank my designation for this course to the Brazilian Navy, whose current commander is the Admiral Eduardo Bacellar Leal Ferreira. I am honored by the trust placed in me to carry out this challenging course.

Thanks to my parents, Décio (*in memoriam*) and Terezinha, for the love and tireless effort to give me and my brothers a happy life. The family structure that you gave me helped me a lot to overcome my obstacles.

Heartfelt thanks to my wife Jorgia and son Theo. Thank you for the tremendous support, love and patience to accept my absence to devote myself intensely to the studies. You made me strong to overcome all the difficulties and to struggle for my goals.

Finally, thank God for this valuable opportunity in my professional life.

This work was funded by the Postgraduate Study Abroad Program of the Brazilian Navy, P.C.Ext., Port.219-09/13/EMA and Port.386/MB-07/13.

Name: Lussac Prestes Maia
College: Faculty of Sciences and Technology
University: University of Algarve
Supervisors: Sérgio Manuel Machado Jesus, Professor at Faculty of Sciences and Technology, University of Algarve
António João Freitas Gomes da Silva, Associate Professor at Engineering Institute, University of Algarve
Thesis title: Environmental model-based time-reversal underwater communications

Abstract

Advances in underwater acoustic communications require the development of methods to accurately compensate channels that are prone to severe double spreading of time-varying multipath propagation, fading and signal phase variations. Assuming the environmental information as a key issue, this work aims to improve communications performance of single-input-multiple-output transmission systems in such channels through the enhancement of their estimates used for equalization. The acoustic propagation physical parameters of the environment between the source and the receivers are considered in the process. The approach is to mitigate noise effects in channel identification for Passive Time-Reversal (PTR), which is a low complexity probe-based refocusing technique to reduce time spreading and inter-symbol interference. The method Environmental-based PTR (EPTR) is proposed that, inspired by matched field inversion, inserts physics of acoustic propagation in the channel compensation procedure through ray trace modeling and environmental focalization processing. The focalization is the process of tweaking the environmental parameters to obtain a noise-free numerical model generated channel response that best matches the observed data. The EPTR performance is tested and compared to the pulse-compressed PTR and to the regularized $\ell 1$-norm PTR. The former is based on classical $\ell 2$-norm channel estimation and the latter, inspired by compressive sensing, uses weighted $\ell 1$-norm into the $\ell 2$-norm estimation problem to obtain improved estimates of sparse channels. Successful experimental results were obtained with the proposed method for signals containing image messages transmitted at 4 kbit/s from a source to a 16-hydrophones vertical array at 890 m range during the UAN'11 experiment conducted off the coast of Trondheim (Norway). The scientific contributions of this work are (i) the understanding of the process of employing physical modeling and environmental focalization to equalize and retrieve received messages in underwater acoustic communications, thus exploiting the sensitivity of environmental parameters in order to adapt a communications system to the scenario where it is used; and (ii) the presentation of a new PTR-based method that focuses environmental parameters to model suitable noise-free channel responses for equalization and whose real data results were successful for a set of coherent signals collected at sea. The proposed method is a step forward to a better understanding on how to insert physical knowledge of the environment for equalization in digital underwater acoustic communications.

Keywords: Underwater acoustic communications, passive time reversal, equalization, coherent communications, physical modelling, environmental focalization.

Nome: Lussac Prestes Maia
Faculdade: Faculdade de Ciências e Tecnologia
Universidade: Universidade do Algarve
Orientadores: Sérgio Manuel Machado Jesus, Professor Catedrático da Faculdade de Ciências e Tecnologia, Universidade do Algarve
António João Freitas Gomes da Silva, Professor Adjunto do Instituto Superior de Engenharia, Universidade do Algarve
Título da Tese: Comunicações submarinas de tempo-reverso baseada em modelo do ambiente

Resumo

Nos últimos anos, as aplicações em comunicações acústicas submarinas, como observatórios oceânicos, veículos submarinos autónomos e controle remoto na indústria de petróleo offshore, entre outros, têm despertado o interesse da comunidade científica. Avanços nessa área requerem o desenvolvimento de métodos que visam compensar os efeitos de distorsão produzidos pelo canal de transmissão submarino no sinal recebido. Essa distorsão é tanto mais importante quanto o cenário de comunicações comporta uma zona de águas pouco profundas, com alcance fonte-receptor de alguns quilómetros e cerca de cem metros de profundidade, os quais são propensos a um severo espalhamento duplo em tempo-frequência devido a propagação de múltiplos caminhos variável no tempo, desvanecimento e variações de fase do sinal. A compensação dessas distorções é necessária para realizar comunicações submarinas com taxas de transmissão de, *e.g.*, mais de 2 kbit/s. Este trabalho tem como objetivos: investigar a influência dos parâmetros físicos da propagação acústica em comunicações submarinas coerentes de alta frequência (∼10kHz-30kHz) em águas pouco profundas, para usar esse conhecimento em prol da melhoria de performance de comunicações com base em modelos físicos e focalização ambiental ou "Environmental Focalization" (EF); e projetar um recetor de tempo-reverso baseado em EF cujo desempenho de equalização com dados reais possa ser superior ao desempenho de um recetor padrão de tempo-reverso.

A abordagem é a de mitigar os efeitos do ruído na identificação do canal para o processador Passivo de Tempo-Reverso (PTR), que é uma técnica de baixa complexidade de retro-focagem para reduzir a dispersão no tempo e a interferência entre símbolos. Para isso, é proposto o método PTR baseado em modelos do ambiente ou "Environmental-based Passive Time-Reversal" (EPTR), o qual usa EF, inspirado em processamento por ajuste de campo ou "Matched Field Processing" (MFP), e insere um modelo de propagação acústica sem ruído no processo para a compensação do canal, esperando com isso eliminar os efeitos de ruído nas estimativas ligando assim o ambiente à resposta do canal. A EF é o processo de ajuste dos parâmetros ambientais para obter uma resposta de canal baseada em modelo numérico sem ruído que melhor corresponda aos dados observados. O método proposto tem um carácter inovador no sentido em que a modelos fisicos, tanto quanto nos é dado saber, não têm sido utilizados em comunicações submarinas.

A influência dos parâmetros físicos de propagação acústica para modelar réplicas do canal de comunicações submarinas tem um papel importante na seleção do espaço de busca "a priori", uma vez que alguns parâmetros físicos são mais influentes na propagação e portanto têm maior efeito sobre as réplicas modeladas. Assim, testes simulados de sensibilidade dos

parâmetros físicos na frequência de 14 kHz foram realizados antes do processamento com dados reais. Embora na faixa de baixa frequência (< 2 kHz) a influência dos parâmetros já seja bem conhecida na literatura, os efeitos desses parâmetros na acústica oceânica em banda de frequência usual de comunicações como, por exemplo, na banda de 10kHz-30kHz, não estão bem documentados. Espera-se com estas simulações obter informações sobre os efeitos da distorção de parâmetros geométricos e geoacústicos, contribuindo para projetar um processador que empregue um procedimento de focagem baseado no modelo do ambiente onde o sistema seja usado.

O uso de um modelo físico livre de ruído provou ser bem sucedido para resolver problemas de MFP com frequência dos sinais usualmente abaixo de 2 kHz como, por exemplo, localização de fontes. Essencialmente, o MFP compara, usando alguma função objetivo, um campo medido com o conjunto de campos acústicos modelados e seleciona a réplica modelada sem ruído com melhor ajuste. Inspirado pelo sucesso do procedimento utilizado em MFP e considerando que as estimativas da resposta impulsiva do canal (CIR) sem ruído podem evitar uma degradação severa do desempenho do PTR, o autor foi motivado a projetar o EPTR que, apesar de usar banda de alta frequência (uma frequência de portador de 25,6 kHz foi usada neste trabalho), produziu resultados experimentais bem-sucedidos através da focalização de um espaço de busca de parâmetros físicos "a priori". A focalização gera como saída uma réplica de resposta impulsiva "a posteriori" sem ruído com melhor aptidão na sua função objetivo. Um processador linear, que correlaciona as réplicas modeladas com uma estimativa de resposta impulsiva, foi usado como função objetivo. Assim, o erro na identificação da CIR causada pelo ruído é substituído por algum erro de modelação, que deverá ser suficientemente pequeno quando a focalização ambiental for bem-sucedida, melhorando o desempenho das comunicações.

As simulações, usando uma frequência de portadora de 14 kHz, mostraram que os efeitos do sub-fundo tendem a ser negligenciáveis devido à severa atenuação , sendo apenas importante a camada superior de sedimentos. Além disso, a velocidade compressional do som nos sedimentos afeta a CIR tanto no espalhamento no tempo como na posição das chegadas, o que é uma característica importante a considerar para escolher candidatos ao espaço de busca "a priori" para focalização, dado que para a compensação do canal a precisão no tempo de atraso de chegada é mais importante do que a amplitude de chegada. O perfil de velocidade do som (SSP) é um parâmetro importante na propagação acústica, por isso é recomendável uma medição *in situ* com equipamento "Conductivity, Temperature, and Pressure" (CTD) para que as réplicas candidatas no espaço de busca sejam baseadas em simulações o mais realísticas possíveis e possibilitem ao método EF gerar um modelo equivalente adequado, *i.e.*, um modelo em que embora os parâmetros físicos não correspondam inteiramente ao parâmetros reais, a compensação entre parâmetros simulados produza uma CIR que seja próxima à resposta real do canal. Os parâmetros geométricos (*i.e.*, a distância fonte-recetores e as suas profundidades) são em princípio os mais importantes, uma vez que causam distorção Doppler severa, muito embora a distorção possa ser significativamente reduzida ao empregar sensores ancorados e técnicas de reamostragem. Para a focalização ambiental, os efeitos devidos ao pequeno comprimento de onda sugerem o uso de alta resolução no espaço de busca de parâmetros; a baixa influência dos parâmetros do sub-fundo sugere excluí-los da otimização, economizando assim custo computacional sem perda significativa de desempenho de comunicações; e, os efeitos da velocidade compressional do som nos sedimentos sugerem aumentar a amostragem do espaço de busca deste parâmetro, visando explorar a característica de mudanças no tempo

de atraso de chegada nos picos da CIR.
Os dados reais modulados digitalmente por comutação-de-fase-em-quadratura (QPSK) recolhidos na experiência de mar "Underwater Acoustic Network'11" realizada em maio de 2011 na costa de Trondheim (Noruega) são utilizados para testar a performance do método de equalização proposto. Várias mensagens moduladas contendo uma imagem de baixa resolução foram transmitidas a 4 kbit/s entre um modem acústico fundeado e uma antena vertical de 16 hidrofones fundeada a uma distância de 890 metros. Os dados são processados com o método EPTR, sendo então comparadas aos métodos PC-PTR padrão e ao RegL1-PTR para análise de performance. Os resultados experimentais mostram que o método proposto supera o PTR padrão, produzindo um ganho robusto (de um total de dez mensagens de 100 mil bits cada, coletadas entre 24 de maio e 27 de maio, sete produziram ganho), em erro quadrático médio. Comparando os desempenhos, o RegL1-PTR mostrou ser o mais estável e efetivo em geral, uma vez que apresentou os maiores ganhos e em todas as mensagens analisadas superou a performance do PC-PTR padrão. O EPTR apresentou os segundos maiores ganhos e em setenta porcento das mensagens analisadas superou a performance do PC-PTR. Em trinta porcento das mensagens o EPTR superou inclusive a performance do RegL1-PTR, gerando o melhor desempenho.
As contribuições científicas deste trabalho são: (*i*) a compreensão obtida no processo de empregar modelos físicos e focalização ambiental para equalização e recuperação de mensagens recebidas em comunicações acústicas submarinas, explorando a sensibilidade dos parâmetros ambientais para adaptar um sistema de comunicação ao cenário onde é usado; e (*ii*) a apresentação de um novo método baseado em PTR que otimiza os parâmetros ambientais para modelar respostas adequadas de canais sem ruído para equalização, cujos resultados usando dados reais foram bem sucedidos para um conjunto de sinais coerentes coletados em experimento no mar. O método proposto contribui para um avanço no sentido de incorporar o conhecimento físico do meio ambiente no processamento para equalização em comunicações digitais acústico submarina.

Palavras-chave: Comunicações submarinas, processamento de tempo-reverso, equalização, comunicações coerentes, modelos físicos de propagação, focalização ambiental.

Contents

List of Acronyms

BER Bit Error Rate

BPSK Binary Phase Shift Keying

CS Compressed Sensing

CIR Channel Impulse Response

CTD Conductivity, Temperature and Depth

DS Doppler Spectrum

DSF Doppler Spreading Function

DFE Decision Feedback Equalizer

EF Environmental Focalization

EPTR Environmental-based Passive Time Reversal

FNO2 Fixed Node 2

FSK Frequency Shift Keying

FsPTR Frequency Shift Passive Time Reversal

BF-FsPTR Beam-forming Frequency Shift Passive Time Reversal

ISI Inter-Symbol Interference

IRLS Iterative Reweighed Least Squares

LASSO Least Absolute Shrinkage and Selection Operator

LARS Least Angle Regression

LE Linear Equalizer

LTI Linear Time-Invariant

LMS Least Mean Square

MIMO Multiple-Input-Multiple-Output

MLSE Maximum Likelihood Sequence Estimator

MP Matching Pursuit

MFP Matched Field Processing

MSE Mean Square Error

MVU Minimum Variance Unbiased estimator

OFDM Orthogonal Frequency Division Multiplexer

PC Pulse Compression

PLL Phase Locked Loop

PTR Passive Time Reversal

16-QAM 16-Quadrature Amplitude Modulation

QPSK Quadrature Phase Shift Keying

RLS Recursive Least Squares

RegL1 Regularized $\ell 1$-norm estimator

RIP Restricted Isometry Property

SIMO Single-Input-Multiple-Output

SNR Signal to Noise Ratio

STU Sub-surface Telemetry Unity

SSP Sound Speed Profile

TL Transmission Loss

TRM Time Reversal Mirror

TVAPM Time Variable Acoustic Propagation Model

UAN11 Underwater Acoustic Network 2011

UANp Underwater Acoustic Network project

uni-SIMO unidirectional Single-Input-Multiple-Output

VLA Vertical Line Array

VLF Very Low Frequency

2D two-dimensional

List of Figures

List of Tables

Chapter 1

Introduction

Preview *In order to contextualize the main issues in equalization of doubly spread channels, this chapter presents an overview of underwater acoustic communications using wireless systems, reviews the state of the art and shows the motivation of the work for developing a channel compensation method based on inserting acoustic propagation modelling and environmental focalization in the equalization process. Section 1.1 introduces the issues involved in shallow water acoustic propagation and the consequent requirement for channel equalization; Section 1.2 reviews equalization for single carrier systems, briefly outlining adaptive equalizers and time-reversal processors. Section 1.3 presents the work motivation and introduces the perspective that leads to the proposed environmental-based time-reversal method; and Section 1.4 presents the thesis outline.*

1.1 Underwater communications and equalization

Underwater communications is a research area of increasing interest to the scientific community, justified by its potential applications to transmit information for remote control of valves in off-shore oil platforms, ocean research data assessment, telemetry for pollution monitoring at sea, communication between divers, control of autonomous underwater vehicles, military underwater communications and underwater acoustic networks, among others.

Cable underwater communication systems are suitable to be used when the transmitter and receiver are assumed static (moored) or when one node is tethered mobile with low spa-

tial coverage as, *e.g.*, in the case of underwater Remotely Operated Vehicles (ROV) which have limited mobility. Alternatively, wireless underwater communications could be advantageously used to extend the spatial coverage of these mobile devices (or of any other device that may require communication without using wires). Wireless acoustic systems designed for ranges greater than few kilometers tend to have easy operation issues in comparison to cabled devices, in general, due to the absence of a long cable in the underwater scenario. Further, depending on the application, cable and wireless systems may be complementary.

Wireless underwater communications systems use the water medium to propagate signals, which are affected by the physics of underwater propagation. In general, the use of acoustic waves is the standard choice for underwater communications because the attenuation is much lower then that of electromagnetic waves and optical waves are affected by water turbidity [1]. Nonetheless, in some cases electromagnetic or optical waves can also be advantageously employed.

Radio underwater communications can be done from terrestrial transmitters to submerged antennas using Very Low Frequency (VLF) band (3-30 kHz), requiring high power land-based transmitters for the signal to cover large maritime areas (few thousands of kilometers) and penetrates in sea water with depth in the order of few tens of meters [2]. The Naval Research Laboratory developed several decades ago a frequency-shift keying system which for the first time permitted automatic operation of the Navy's VLF transmitters at a rate of 60 words per minute with a reasonable degree of reliability for command-control communications with submarines [3]. Since then, systems were significantly improved in terms of data rate although having limited range: for instance, two systems with rate up to 16 kbit/s at distances of 20 meters and rate 1-10 Mbit/s at distances less than 10 meters

were developed by Wireless Fiber Systems [4].

Optical underwater communications can operate with very high-rate (order of megabits) and very short range (less than one hundred meters). A modem projected by WHOI [5, 6] for the transmission of information from an ocean observatory has the potential to transfer rates of up to 10 Mbit/s at distances up to 90 meters in clean water with use of a receiver based on photomultiplier tubes and a laser diode emitter. Other examples include one of the newer versions of the AquaOptical [7] modem that achieves transmission rate of 2.28 Mbit/s in clear water at distances of 50 meters or Blueard systems from Sonardyne [8, 9] based on photo-multipliers.

Acoustic waves can propagate to large distances in underwater unbounded media, depending on the frequency of operation, and therefore are the solution of choice for underwater communications in applications where wired connection is disadvantageous [1]. For instance, acoustic modems are appropriate in scenarios with ranges greater than one hundred meters in both shallow and deep water. However, transmission loss caused by volume spreading and frequency selective attenuation are factors determining the attainable range and bandwidth in unbounded underwater media, limiting the data rate of acoustic transmission. Moreover, channel impulse response with multipath (which causes time spreading on the received signal) and channel impulse response time-variability (which causes frequency spreading of the received signal) may occur, imposing severe limitations on the system performance.

In severe multipath scenarios it is common to achieve data rates of a few hundred bit/s for coherent communications, at best. In scenarios with mild conditions the data rate can be higher, as described, *e.g.*, in [10], which reported an experiment where a Multiple-Input-Multiple-Output (MIMO) Orthogonal Frequency Division Multiplexer (OFDM) sys-

tem achieved a data rate of 125.7 kbit/s over a bandwidth of 62.5 kHz. Two transmitters with 16-Quadrature Amplitude Modulation (16-QAM) and coding were used to reach the results, suggesting that MIMO-OFDM is an appealing solution for high data rate transmissions over underwater acoustic channels. This scenario had mild conditions because the channel impulse responses in such experiment were, in general, with few multipath delays, extending in a time window of less than 4 ms. Shallow water communication, *i.e.*, when the source-receiver range is several times greater than the water depth, may present long delay time spreading, *e.g.*, more than 15 milliseconds, depending of the scenario, thus causing severe multipath propagation distortion.

This work focuses on shallow water acoustic communication channels, where the acoustic waves propagate with multiple interactions with the boundaries, *i.e.*, the seabed and the sea surface, thus forming a natural waveguide. The acoustic field in such environment is characterized by multiple constructive/destructive interferences, yielding a complicated propagation pattern that can be predicted by a physical model as, *e.g.*, ray/beam trace model, normal modes model, parabolic equation model, to cite a few. Since the multipath propagation may form channel impulse responses characterized by several delayed arrivals after the first arrival, severe Inter-Symbol Interference (ISI) may occurs, extending to a significant number of adjacent symbols. Therefore, aiming to reduce the ISI and to reach successful message recovery, it is necessary to compensate for the Channel Impulse Response (CIR) distortion in the underwater waveguide by applying a robust coherent channel equalization method, which should be adaptive when in presence of time-variability.

Techniques for underwater channel equalization to mitigate ISI and improve communications performance can be found in several reports in the literature. However, most of

them are based mainly on adaptive equalizers, such as, *e.g.*, the Decision Feedback Equalizer (DFE) [1, 11] and/or on time-reversal processors, such as, *e.g.*, the Passive Time-Reversal (PTR) [12, 13, 14], which frequency domain version is known as Phase Conjugation. The DFE principle is to track the inverse channel during a training mode operation to design a adaptive filter which compensates for channel distortions during transmission mode. The PTR principle is to employ the reciprocity property of the wave equation through the use of an array of sensors connected to a multichannel receiver that perform conjugate time-reversal filtering and summing over channels, aiming to compensate for multipath distortion. It requires channel estimates for feeding the reverse filters during the message reception period, assuming that the channel is stable in such time interval. More on these techniques are discussed in Sec. 1.2.

Channel identification is a requirement for PTR receivers, where the CIR estimates feed the time-reversal filters. Usually, conventional PTR employs a probe pulse with suitable correlation properties to estimate the channel using pulse compression. However, in real data, the channel estimation with pulse compression method is prone to noise in the received probe signal, decreasing the accuracy of the CIR estimates. The inaccuracy in CIR estimation is an important issue in PTR receivers, that can severely decrease its performance. A different method of channel estimation, that may increase CIR accuracy, is the $\ell 1$-norm regularization. Since the impulse responses in shallow water channels are characterized by arrival paths and considering that a CIR time window extends sufficiently so that there are few paths with large energy and the other arrivals with very low energy, mostly attributed to noise, then the CIR can be assumed sparse. This assumption opens the opportunity to use the Regularized $\ell 1$-norm (RegL1) channel estimator, that explore sparse features for increasing the CIR

accuracy. It is widely employed in compressive sensing theory [15, 16] and can yield cleaner CIR estimates then pulse compression, due to its higher immunity to noise and path side lobes effects.

This work proposes another different method for CIR identification based on a processor that employs an underwater acoustic propagation model and an environmental focalization algorithm, which is driven by physical information of the environment, to generate the CIR replicas that feed the PTR filters. Whether or not this model-based CIR estimate would be suitable for employment in a real channel compensation problem would depend on the degree of accuracy of the model. Acoustic propagation models require as input a set of physical parameters that represent the environment where the acoustic field is to be predicted. Usually, the parameters are the source/receiver positions and bathymetry (also known as geometric parameters), the density, compressional/shear speed and attenuation of the seabed (also known as geoacoustic parameters) and the sound speed profile of the water column. In a strict sense, such physical parameters are unknown in a real environment. In a wide sense, one may roughly estimate those parameters by assuming that a particular area can be represented by the parameters assessed with some samples collected in-situ with dedicated equipment as, e.g., Conductivity, Temperature and Depth (CTD), thermistor chain, bottom grab, echo sounding and pressure gauge. Also, it may be used knowledge from previous measurements, but this must be carefully addressed to avoid over-outdated environmental data being used so as to no longer adequately represent the scenario.

In real data processing, unfortunately the simple employment of a set of physical parameters chosen empirically as input for an acoustic propagation model will hardly represents the actual acoustic field or actual CIR, due to lack of accuracy. It would be necessary to know

the exact parameters that represent the actual environment, which is a hard requirement. However, such requirement can be relaxed through the use of an "a priori" search space of physical parameters which, after optimization, generates the CIR that best matches a noisy observed CIR, in a process named Environmental Focalization (EF). The advantage is to generate a noise-free "a posteriori" CIR replica which, assuming a sufficient accuracy, can substitute the corresponding noisy CIR estimate used as reference during the optimization. As will be shown along this work, to employ the EF method may be a suitable approach to improve the performance of time-reversal communications in shallow water. In this sense, the Environmental-based Passive Time-Reversal (EPTR) is proposed to improve a conventional PTR receiver through the insertion of physical information of the environment in the equalization process, using the EF method for CIR identification. The EPTR will be tested with real data and compared with other PTR based receivers using CIR estimation based on Pulse Compression (PC) and sparse CIR estimation based on Regularized $\ell 1$-norm (RegL1). More on the EF method is discussed in Sec. 1.3 and the EPTR receiver is later described in details in Chap. 2.

1.2 State of the Art

Channel equalization for single carrier systems is reviewed, briefly outlining adaptive equalizers and time-reversal processors, using as starting point for discussion a short historical review in digital acoustic underwater communications. Further, a discussion on environmental focalization and equivalent modelling is done in the context of motivating the need for developing a method that combine acoustic propagation physical modelling and channel equalization.

1.2.1 Short historical underwater communication review

Prior to the 1970's there were a few published reports of acoustic modems. Analog systems were developed as, *e.g.*, an underwater telephone which permitted voice communications between ships and submarines[1], but they had no capability for mitigating the distortion introduced by the highly reverberant underwater channel.

During the 1980's, incoherent systems using Frequency Shift Keying (FSK) modulation were widely employed as the best option in terms of data rate[2]. Since this modulation scheme is incoherent, it does not require capturing the signal phase to recover the message. At that time, the inability to explore the phase brought the research focus to frequency modulation. Although it has high power efficiency, the bandwidth inefficiency inherent to such systems restricts their use to low data rate transmissions, say less then 1 kbit/sec. The inefficiency is caused by the requirement of sufficiently separate the FSK frequency tones with more than the coherence bandwidth (the inverse of the multipath spread), aiming to avoid frequency aliasing [1]. The search for improving bandwidth efficiency induced to the research on coherent modulation [18].

Several works about coherent underwater communications systems have been published since the 1990's, e.g.,[12, 18, 19, 20, 21], given that coherent systems are able to overcome the ISI caused by multipath propagation through the employment of equalization algorithms. This more efficient bandwidth scheme contributed to move acoustic telemetry from the well-behaved vertical deep channel (which is a reduced multipath channel) into the more

[1]The underwater telephone, designated the AN/UQC, was developed by the US Navy, being a suppressed carrier single side band amplitude modulation (SSB) system operating on a carrier frequency of approximately 8 kHz, as described in [17].

[2]In fact, note that FSK is still widely used nowadays in applications at which low data rate, *e.g.* less then 1 kbit/sec, is acceptable.

ill-posed horizontal shallow water channel (which is a severe multipath channel). Most of the coherent modems used a Linear Equalizer (LE) or a Decision Feedback Equalizer (DFE), coupled with Phase Locked Loop (PLL) for carrier synchronization [11, 21]. Also during the 1990's, research on time-reversal were developed [12]. In 1996, Kuperman *et al.*, based on an experiment conducted in the Mediterranean Sea, performed an experimental demonstration of an acoustic time-reversal mirror [19]. After, avoiding the high complexity of DFE, the passive time reversal receiver [14] emerged as a low complexity channel compensation method to reduce ISI due to multipath, based on conjugate time-reverse filtering applied to the signals received in a vertical array of hydrophones spanning the water column.

During the 2000's, time-reversal phase coherent underwater communications was proposed [22] and since then used in several works as , *e.g.*, in [23, 24, 25, 26, 14].

Nowadays, channel compensation for coherent communications in shallow water often relies in the combination of adaptive DFE equalization and PTR methods.

1.2.2 Adaptive equalizers

The adaptive DFE is a standard coherent underwater acoustic communications processor, early employed in single-input-single-output transmissions [21]. It originates from earlier stage non-adaptive equalization that aimed to eliminate ISI by designing an inverse filter to revert the distortion caused by the channel, under the assumption that the channel behaved as a FIR filter with additive noise[3]. As described in [11], this former non-adaptive processor is the so-called Zero-Forcing Equalizer. The implementation of error minimization of the filter coefficients using the MSE criterion leads to the LE [11]. Depending on the tap spacing,

[3]In fact, the linear equalizer is a FIR filter while the DFE is a IIR filter due to contain a feedback part (*i.e.*, a recursive part of a filter) additionally to the forward part.

which could be the inverse of the symbol interval or a fraction of it, the LE is still called, respectively, symbol spaced equalizer or fractionally spaced equalizer.

The LE is a suboptimal detector that minimizes the MSE using a transversal filter. The optimal detector is the Maximum Likelihood Sequence Estimator (MLSE), in the sense that it minimizes the probability of a sequence error. The MLSE can be implemented with the Viterbi algorithm [27]. The DFE is a sub-optimum detector composed by a forward filter and a feedback filter that aims at a better performance than the LE, which uses only a forward filter. The feedback filter aims at removing the part of the ISI of the present estimated symbol caused by previously detected symbols.

In non-adaptive DFE (and LE) the CIR is assumed known in the receiver [11]. However, since in many communications systems the channel characteristics are unknown and the channel is often time-variant in some degree, then the adaptive DFE or adaptive LE were proposed.

Adaptive equalizers may employ the Least Mean Square (LMS) algorithm or the Recursive Least Squares (RLS) algorithm to iteratively perform error minimization, requiring a probe training sequence to adjust the filter coefficients during training mode. After reaching convergence, the processor performs equalization during a direct-decision mode. Also, equalizers that do not use the probe training sequence are proposed in [11], performing the so-called blind equalization.

The standard adaptive DFE is accurate and broadly used in aerial wireless communications. However, in wireless underwater communications a lack in robustness may occur mainly due to error propagation issues, a problem inherent to the iterative algorithm con-

vergence, specially in long frames [28]. Additionally, the DFE can be used in multichannel instead of the standard single channel configuration, aiming to yield more robust equalization, as proposed in [29, 30].

1.2.3 Time-reversal processors

Time-reversal processors use for a vertical array of transducers the reciprocity principle of the linear wave equation. Assuming an acoustic signal being transmitted from a source to the array of transducers, if the received signals are time-reversed and retransmitted, the energy of the retransmitted signals concentrates with constructive interference on the position of the source. This principle drives the active Time Reversal Mirror (TRM) in underwater communications [19, 24]. As described by Kuperman [31], the TRM produces a real acoustic image of the probe source (PS) by converting a divergent wave emitted from the acoustic PS into a convergent wave focusing on the PS. A TRM can be realized by an array of transducers. The incident signal is received, time reversed, and retransmitted from an array of sources collocated with the receivers.

The PTR processor, instead of transmitting the time-reversed signal through the ocean channel from the receiver to the source, performs this operation in a computer to filter the incoming transmitted signal. A description of PTR can be found in [14] and in a large body of work in the literature. Despite its simplicity, PTR requires a sufficiently long and dense array to reduce ISI, avoiding poor sampling of the high-order modes [19, 23, 32]. Also, it requires time stationarity which is inherent to the whole PTR process. CIR estimates are required, being typically obtained by correlating each received distorted probe signal with the transmitted probe signal, resulting in a noisy estimate of the channel Green's function.

Such standard CIR estimation technique is equivalent to the pulse compression, commonly used by radar and sonar to increase the range resolution and the signal to noise ratio. The channel must be nearly time-invariant since PTR can not capture time variability until the next probe.

Further, the PTR has much lower complexity than the adaptive DFE, because the former is mostly based on cross-correlation operation. Also, PTR is more robust than the adaptive DFE because the latter can have algorithm convergence issues when using long frames [28]. However, PTR is less accurate than DFE in the sense that significant residual ISI remains in the PTR output signal, as described by Stojanovic in [33].

A processor derived from PTR is the Frequency Shift Passive Time Reversal (FsPTR), proposed in [32]. Although PTR allows for the implementation of a simple communications system, it loses performance in the presence of geometric mismatch between the probe signal and the actual data symbols transmission. Assuming that geometric mismatch, in depth and range, could be partially compensated by applying an appropriate frequency shift in the PTR operator, real data results are presented in [32] with Binary Phase Shift Keying (BPSK) modulation scheme and carrier frequency 3.6 kHz. A gain is expected for FsPTR over PTR due to the fact that the processor in some degree compensates for the channel variability. The results showed FsPTR achieving an overall gain of approximately 4.11 dB over a conventional PTR processor.

Another PTR-based processor is the Beam-forming Frequency Shift Passive Time Reversal (BF-FsPTR), proposed in [34]. Considering the fact that each multipath wavefront may be assumed independent, the BF-FsPTR apply an independent frequency-shift to each wavefront, aiming to compensate for the channel variability. The wavefront means a surface

containing points affected in the same way by a propagating wave at a given time. It is expected that the BF-FsPTR yields gain over a FsPTR processor because the latter uses just a single frequency shift to all wavefronts, resulting in performance degradation. Real data results are presented in [34], using a frame with bit rate 2 kbit/s and BPSK modulation scheme, showing that the BF-FsPTR, using angular range of the beam-former from -10 to +10 degrees, yielded a mean gain of 2.2 dB over the FsPTR, in terms of mean square error.

A probe-based channel estimation method is required by PTR (and by the methods based on it). In its conventional form, the CIR estimates are obtained using Pulse Compression (PC), which is a signal processing technique performed by transmitting a probe pulse and then correlating the received signal with the transmitted pulse. A theoretical derivation of PC can be done from the Minimum Variance Unbiased estimator (MVU) [35], as described in Appendix A. In case the channel is approximately sparse, where the CIR, in a discrete version, is a nearly sparse vector[4], the classical PC channel estimation (based on $\ell 2$-norm) can be substituted by an approach that includes the Regularized $\ell 1$-norm (RegL1) in the $\ell 2$-norm estimation problem. The advantage is to generate sparse CIR estimates less prone to noise effects, making the channel identification process more accurate. Since PTR is very sensitive to errors or inaccuracies in CIR estimates, the RegL1 is an attractive approach to improve the PTR performance.

Furthermore, using an environmental model-based approach for CIR identification, this work proposes to modify a conventional PTR receiver, replacing noisy CIR estimates by noise-free CIR replicas generated by a physical model and optimized by an environmental focalization algorithm. Such method is next discussed in Sec. 1.2.4.

[4]The vector is assumed sparse whether few elements of the vector have high values and the others have very low values.

1.2.4 Environmental focalization and equivalent model

In the context of incorporate acoustic propagation physical parameters in the process of equalization of shallow water communication channels, the EPTR uses the Environmental Focalization (EF). The form to include physical parameters in underwater acoustics is via numerical propagation models. Although numerical models have not been used in underwater acoustic communications, they have been proven successful in techniques such as matched-field processing (MFP) for source localization, initially proposed by [36] and [37], (see details in [38] and an overview in [39] and references therein); ocean acoustic tomography (OAT) [40, 41]; and matched-field inversion (MFI) for generic environmental parameter estimation [42, 43]. There exists a large body of work, with a variety of processing techniques with their particularities and application fields, but they all have one common feature: they feed environmental information in numerical models and compare the output to experimental data.

The EF is based on the process of tweaking the "a priori" environmental parameters contained in a search space that, after being optimized under the criterion of a particular objective function, generates the "a posteriori" physical parameter that corresponds to the acoustic field replica that best matches the observed acoustic field. In this work, we are interested in obtain the "a posteriori" CIR instead of an acoustic field. By expanding the number of parameters in the search space to include an additional narrow search over parameters previously known "a priori", the EF may reach a better adjustment in the objective function, thus making it possible to reduce mismatch between the CIR replicas and the CIR estimate.

Collins *et. al.* [43] first demonstrated the EF in source localization, showing that the acoustic adjustment was increased if, not only the unknown parameters were included in the parameter space, but also the known parameters, which resulted in that the known ones would vary to slightly different values, improving the acoustic adjustment and thus improving the location of the source. Eventually the search space was adjusted differently to the known and unknown parameters, being more restricted to the first ones and more extended to the second ones.

The EF yields an equivalent model driven by the better combination of parameters that maximizes the acoustic field adjustment. The concept of using a equivalent model is fully described in [44] and essentially consists in employing a set of acoustic propagation physical parameters to generate an environmental model that maximizes a particular objective function, regardless on whether that parameter set in fact represents the actual environment. The environmental model is named "equivalent" in the sense that it better matches with the observed channel under the metrics of the objective function.

The acoustic field is defined by a large set of environmental properties, which vary with space and time. Due to the limitations in observing these quantities with a fine space-time discretization, it is essential to know the degree of dependence of the acoustic field on each of them. Therefore, when aiming to use techniques as matched field processing or environmental focalization, for which the equivalent environmental models are a by product, one of the first steps is to understand the relative importance of each environmental parameter. In this sense, an analysis based on a set of simulations is later performed in Chap. 3 on the sensitivity of physical parameters of the environment.

In EF, one can expect to find some degree of compensation between physical parameters,

since there is a correlation between the effects of some physical parameters on acoustic propagation. For example, a high density on the seabed is expected to occur along with a high compressional sound speed on the seabed, because both are found on a high reflection seabed (see typical geoacoustic parameters in Table 3.2 [45]). Thus, in this sense, the seabed density and the seabed compressional sound speed are correlated. In [44], Martins presents a study quantifying the compensation between several parameter pair for a transect with 5 km source-receiver range and frequencies multi-tones in the 100-1000 Hz band. Such work clearly shows, for low frequency band, that a significant compensation between different acoustic propagation physical parameters may occurs.

Therefore, in order to obtain an accurate CIR replica in a situation of environmental mismatch, the EF must find a set of environmental parameters that, in some degree, compensate for that mismatch. These parameters form the equivalent model obtained from the best combination between the CIR replicas in a given search space and the CIR estimate. Even if this equivalent model does not actually correspond the real environment, the CIR it generates is the closest to the CIR estimate used as a reference for optimization, with the advantage of being noise-free. This noise-free CIR replica can replace a noisy CIR estimate in PTR, and if the former is sufficiently accurate, communications performance can be increased.

1.3 Motivation

The motivation of this work is based on (*i*) the need to perform channel equalization in coherent underwater acoustic communications, specially in shallow water, and on (*ii*) the possibility of including information on the physics of acoustic propagation in the process of

channel equalization, because the physical parameters of propagation severely influence the channel impulse response. It is expected that using the environmental focalization method to obtain noise-free modeled CIR estimates for feeding time-reversal filters, we can lead to improved communications performance, assuming that a low level of modeling error is achieved by the EF processor. The method relies on ray trace numerical modelling to compute the impulse response of shallow water waveguides and on an EF algorithm designed to compute the channel impulse response replica that best matches a channel estimate. Also, the method must be validated by successful results of real data processing from a coherent underwater acoustic communication sea trial.

Taking into account that: (*i*) shallow water communication channels present multipath propagation where the CIR is composed by path delays spread in time, and if not compensated or equalized, such channel severely degrades the communication performance; and (*ii*) inevitably the CIR and its variability in space and time is related to the same variability of the physical parameters of the channel; we formulate the following set of hypothesis: (*i*) the use of a physical model driven by a particular set of physical parameters chosen to represent the actual environment can generate a CIR estimate that is accurate enough to perform channel equalization with real communications data; and (*ii*) the computation of a CIR sufficiently accurate for successful channel equalization can be automatically performed by an optimization algorithm that focalizes, from an "a priori" search space, an accurate "a posteriori" CIR replica to compensate the channel. In this thesis the above hypotheses are extensively tested with the goal of improving communications performance through the inclusion of physical information of the channel, collected from the environment where the system is employed. The Environmental-based Passive Time Reversal (EPTR) processor is

proposed in this context, and its expected advantages are two fold: increase communications performance through noise effects mitigation in CIR estimates; and make the communications system more robust because the physics of the channel where the system is located is included in the equalization process.

1.3.1 Promissory perspective

This work proposes to incorporate physical information of the environment where the communication signals propagate, through the use of physical numerical models, in the process of equalization of shallow water communication channels based on a PTR receiver. The EF (as well as MFP) feeds environmental information in a numerical model and compare the output to real data. In that sense this technique is called as "model-based" as opposed to "data-driven" only.

Many studies carried out with model-based techniques refer the difficulties to favorable compare modeled and experimental data in the high frequency range, say, above 2 kHz. This seems to be the reason why, to the best of the author's knowledge, there are no reports on the usage of physical numerical models to design CIR replicas for channel equalization of real underwater acoustic communications data. In our case we are not interested in physical parameter estimation (as would be the case of MFP), but solely in CIR modeling for the EPTR. The physical models Bellhop and Bounce [46, 47] are used as forward acoustic propagation models for generating CIR candidate replicas search space. EPTR has a drawback of expending more computational cost than PTR. In spite of that, the advantages of EPTR over the conventional PTR are to achieve noiseless CIR estimates and perform channel compensation together with a (secondary) physical parameters assessment. The noiseless

estimates may, if the environmental focalization succeeds to reduce modelling error, improve the performance in time-reversal underwater acoustic communications.

1.3.2 Objectives

The objectives of this work are summarized as follows:

1. To investigate the influence of acoustic propagation physical parameters in underwater communications in order to get understanding on how modelling of shallow water acoustic propagation could be useful for channel equalization;

2. To design an environmental model-based channel equalizer which inserts physical information of the environment in the process of channel compensation, through the usage of acoustic propagation model and environmental focalization algorithm, in order to (i) improve communications performance and (ii) make the system more robust relying in the fact that physical information from the environment where the system is employed is considered during the equalization processing; and

3. To validate the EPTR with real data, comparing its performance with the conventional PTR based on PC channel estimation (PC-PTR) and the PTR based on RegL1 sparse channel estimation (RegL1-PTR).

1.4 Thesis outline

The thesis is structured as follows:

Chapter 2 describes the data model and the various PTR-based methods of channel equalization, *i.e.*, the conventional PC-PTR, the sparse RegL1-PTR and the EPTR driven

by the model-based EF method. Since the latter uses a CIR estimate for focalization, two configurations are presented as PC-EPTR and RegL1-EPTR.

Chapter 3 describes aspects of the underwater acoustic propagation modeling in shallow water and presents simulations of standard time-reversal processing in underwater acoustic communications, testing the system sensitivity to the variability of physical parameters.

Chapter 4 presents the UAN11 sea trial and the results of real data processing with EPTR, including a long term analysis. The EPTR performance obtained from real data results is analyzed and compared to the performance obtained from PC-PTR and RegL1-PTR.

Chapter 5 concludes the thesis, showing the advances in communications performance obtained with the proposed EPTR receiver based on EF method, presents the scientific contributions and, finally, indicates future directions.

Chapter 2

Methodology and data model

Preview *This chapter presents a detailed description of Passive Time Reversal (PTR) and the Environmental-based Passive time Reversal (EPTR), using as channel identification the methods Pulse Compression (PC), Regularized $\ell 1$-norm (RegL1) and Environmental Focalization (EF). The appropriate combination of these methods yields the receiver configurations PC-PTR, RegL1-PTR, PC-EPTR and RegL1-EPTR, which are further tested with real data in chapter 5. Section 2.1 presents the methodology for channel identification in the four cases, and how it is applied to time-reversal filtering; Section 2.2 presents the system data model; Section 2.3 presents the standard PTR; Section 2.4 presents the PC channel estimation; Section 2.5 presents the sparse channel estimation RegL1; Section 2.5 presents the EF channel estimation; and Section 2.6 presents the proposed EPTR based on environmental focalization.*

2.1 Methodology

The methodology adopted in this work is to verify the degree of sensitivity of three channel identification probe-based methods: Pulse Compression (PC), Regularized ℓ1-norm (RegL1) and Environmental Focalization (EF). PC and RegL1 are well-known CIR estimation methods that may be applied in PTR receivers and EF is the proposed model-based estimation method for the EPTR. These methods are described in this chapter in the context of its application in time-reversal communications in shallow water, where CIR present time spreading due to multipath. The degree of accuracy in the CIR estimates generated with each method

will significantly affect the efficacy of the time-reversal filtering in compensating for the multipath channel.

The application of the channel identification methods mentioned above results in the following configurations of time-reverse receivers: (*i*) PC-PTR, using the conventional PC method based on $\ell 2$-norm; (*ii*) RegL1-PTR, using the sparse estimation method based on $\ell 1$-norm regularization; and the proposed EPTR using the EF method based on physical modelling of CIR replicas that best match a channel estimate. Since the Environmental Focalization (EF) uses an estimate as reference in its objective function, then we have two sub-configurations of the EPTR method, that are (*iii*) PC-EPTR and (*iv*) RegL1-EPTR.

Figure 2.1 shows the four combinations of channel estimation methods for time-reversal communications that are tested in this work.

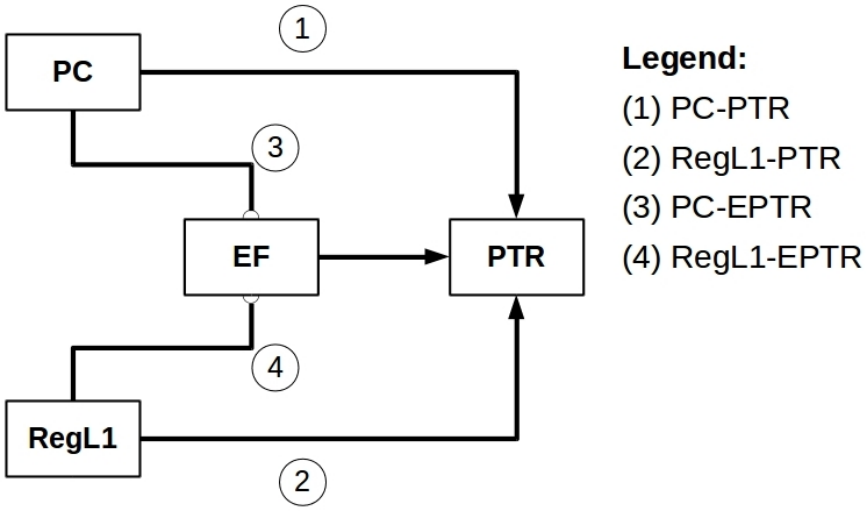

Figure 2.1: Methodology to test EPTR and compare performance with PTR: four possibilities for channel identification applied to time reversal underwater communications: (*i*) PTR with pulse compression (PC-PTR), (*ii*) PTR with $\ell 1$-norm regularization (RegL1-PTR), (*iii*) EPTR with pulse compression (PC-EPTR) and (*iv*) EPTR with $\ell 1$-norm regularization (RegL1-EPTR).

The PC-PTR and the RegL1-PTR are well-known in literature and are used in the present work for performance comparison. The PC-EPTR is the proposed environmental model-

based in its standard form using pulse compression and the RegL1-EPTR is its modified form for comparison to numerical modeled channel replicas for sparse channel estimates.

2.2 Communication system data model

The transmission of a data stream at one single source and received at an array of L receivers Single-Input-Multiple-Output (SIMO) in the ocean is modeled as an input signal $s[n]$ being convolved with the CIR $g_l[n,k]$, which represent the ocean channel between the source location and each individual receiver l and where implicitly the ocean is supposed to be a linear system, added to the noise component $w_l[n]$ assumed as wide sense stationary uncorrelated random noise, to yield the output $y_l[n]$, where the subscript l denotes the l-th channel. Figure 2.2 shows the block diagram of a SIMO system with L channels, in baseband equivalent discrete representation.

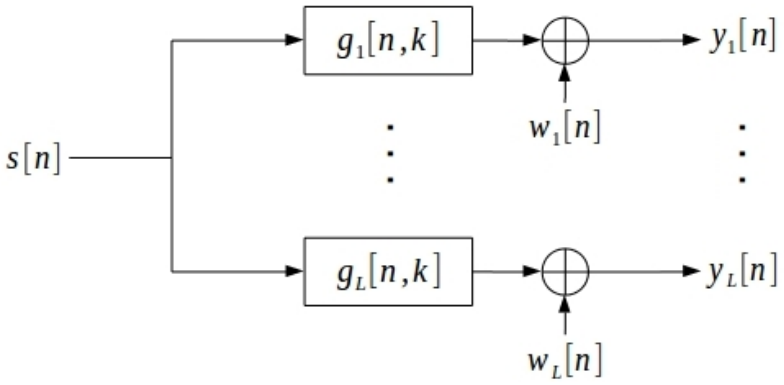

Figure 2.2: Ocean data model as a Single-Input-Multiple-Output (SIMO) system with L channels in baseband equivalent representation. Input signal $s[n]$, discrete CIR $g_l[n,k]$, noise $w_l[n]$ and the output signals $y_l[n]$ for the l-th channel.

The signal $s[n]$ is the baseband equivalent discrete version of the real transmitted pass-band signal $\tilde{s}(t) = Re\left[s(t)e^{j2\pi F_c t}\right]$ heterodyned to the carrier frequency F_c.

A bit stream message $m[i]$ is digitally modulated with a phase shift key scheme to form the symbol sequence $a[i]$, which after being up-sampled with symbol interval T_s and filtered

with a pulse shape raised cosine filter $p[n]$, whose frequency response is designed to have no ISI at the sampling instants, to yield the discrete baseband signal

$$s[n] = \sum_i a[i]p[n - iT_s], \tag{2.1}$$

where the M-PSK modulated symbol sequence message is given by

$$a[i] = e^{j2\pi(m[i]-1)/M}, \quad m[i] \in [1, ..., M] \tag{2.2}$$

with M denoting the symbol map size. The symbol sequence $a[i]$ is assumed to be a random sequence with uniform distribution, thus the baseband equivalent transmitted signal $s[n]$ is also random. Note that the implementation of the PTR requires the transmission of probes for channel identification so, during channel probing, message bearing signal $s[n]$ will be replaced by a probe signal. As it will be seen later on, that probe signal will be required to have a sharp autocorrelation function.

The received signal, in the case of a linear time-invariant system, is assumed to be given by the convolution between the channel impulse response and the transmitted signal. However, in a time-variant system this is not valid. Instead, an integral operation that performs time-variant filtering must be done. The time-variant CIR for a particular source-receiver transect can be represented by the two-dimensional complex baseband variable $g[n, k]$, where the discrete delay-dimension k is the reduced time CIR snapshot coordinate, while several sequential snapshots may be recovered along the discrete true time variable n. Note that each CIR snapshot represents a state of the time-variant channel in a particular time instant and its replica can be modeled by computing the path gain and delay pair generated by an appropriate underwater acoustic propagation model. Thus, assuming hereafter a complex

baseband equivalent representation, the noisy received signal $y[n]$ is given by

$$y[n] = \sum g[n,k]s[n-k] + w[n], \tag{2.3}$$

where $w[n]$ denotes additive random noise.

Equation (2.3) can be rewritten as a function of P CIR snapshots, being the p-th snapshot denoted as the vector $g_p[k]$, which are contained in the two-dimensional time-variant CIR denoted as the matrix $\mathbf{G}$ which entry is n, k, that is $\mathbf{G}_{nk} = g[n,k]$. Using matrix notation, one may assume $\mathbf{s} \in \mathbb{C}^{K\times 1}$, $\mathbf{G} \in \mathbb{C}^{P\times J}$ and $\mathbf{g} \in \mathbb{C}^{J\times 1}$ to form the discrete CIR matrix $\mathbf{G}^T = [\mathbf{g}_1, \mathbf{g}_2, ..., \mathbf{g}_P]$, where $\mathbf{g}_p$ is the p-th CIR snapshot vector, $P = K + J - 1$ is the convolution size and the superscript T denotes transpose. Thus, the discrete time-variant system is given by

$$\mathbf{y} = diag(\mathbf{S}\mathbf{G}^T) + \mathbf{w}, \tag{2.4}$$

with

$$\mathbf{y}^T = [y[0], y[1], ..., y[P-1]], \tag{2.5}$$

$$\mathbf{S} = \begin{bmatrix} s[0] & 0 & \dots & 0 \\ s[1] & s[0] & \dots & \vdots \\ \vdots & \vdots & & 0 \\ s[K-1] & s[K-2] & & s[0] \\ 0 & s[K-1] & & \vdots \\ 0 & 0 & \ddots & \vdots \\ \vdots & \vdots & & \vdots \\ 0 & 0 & \dots & s[K-1] \end{bmatrix}, \tag{2.6}$$

$$\mathbf{G} = \begin{bmatrix} g[1,0] & g[1,1] & ... & g[1,J-1] \\ g[2,0] & g[2,1] & ... & g[2,J-1] \\ \vdots & \vdots & \ddots & \vdots \\ g[P-1,0] & g[P-1,1] & ... & g[P-1,J-1] \end{bmatrix}, \tag{2.7}$$

$$\mathbf{w}^T = [w[0], w[1], ..., w[P-1]], \tag{2.8}$$

where matrix $\mathbf{S}$ has a Toeplitz structure and is computed from zero-padded $\mathbf{s}$ with $\mathbf{S} \in \mathbb{C}^{P \times J}$.

When sufficient compensation for the Doppler effect in $g[n,k]$ is performed, the snapshots are kept nearly invariant along time and $g[k] \simeq g[0,k]$. Thus the received signal becomes

$$y[n] \simeq \sum_k g[0,k]s[n-k] + w_l[n] \simeq \sum_k g[k]s[n-k] + w[n] \simeq s[n] * g[n] + w[n] \tag{2.9}$$

where symbol $*$ denotes convolution. Further, instead of using $g[k] \simeq g[0,k]$ that assumes an initial snapshot to represent the CIR, one may appropriately use the mean along n axis $g[k] \simeq \bar{g}[n,k]$. When an array of hydrophones is being used, the received signal is given by

$$y_l[n] \simeq \sum_k \bar{g}_l[n,k]s[n-k] + w_l[n] \simeq s[n] * g_l[n] + w_l[n] \tag{2.10}$$

where l represents the hydrophone.

2.3 Passive time reversal

When applied to communications the usual data frame of $s[n]$ in composed of a probe signal followed by the data signal, where the probe signal is used to estimate the channel response $\hat{g}[n]$ and the data signal contains the payload, *i.e.*, the baseband version of the symbol sequence message.

Figure 2.3 shows the PTR receiver block diagram, assuming L channels, in baseband equivalent discrete representation and with the use of square root raised cosine filters split between the transmitter and the receiver for pulse shaping [11, 18]. The l-th channel output $y_l[n]$ is the input to the pulse shape $p[n]$ followed by a conjugate-reverse filter $\hat{g}_l^{\dagger}[-n]$ fed by the CIR estimate $\hat{g}_l[n]$, with the superscript † denoting conjugate, yielding the l-th output $z_l[n]$. After summing, the PTR output $z[n]$ is generated.

The PTR is known as a low complexity channel equalizer that uses multichannel probing

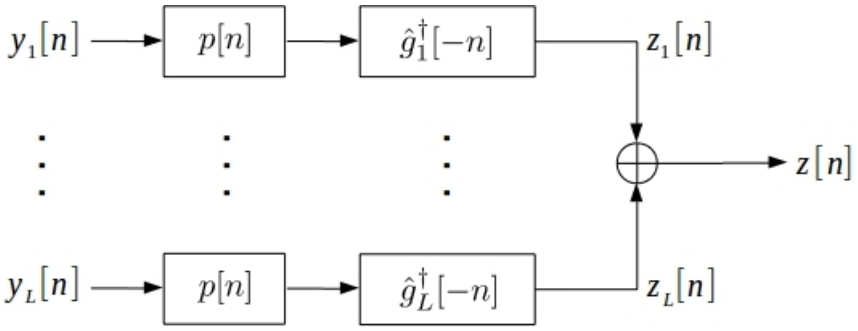

Figure 2.3: The PTR receiver diagram for a SIMO system with L channels in baseband equivalent representation. The received signals $y_l[n]$ are passed through square root raised cosine filters $p[n]$ then through conjugate time-reverse filters $\hat{g}_l^\dagger[-n]$ based on discrete CIR estimates $\hat{g}_l[n]$ and then summed to yield the final PTR output signal $z[n]$.

for time signal refocusing, thus reducing inter-symbol interference caused by multipath propagation. Since the PTR equalizer performs time-reversal matched-filtering of the received signals on each channel with the CIR estimates and assuming that the pulse shape $p[n]$ is a square root raised cosine filter split between the transmitter and the receiver, the PTR output is given by

$$z[n] = \sum_l z_l[n] = \sum_l y_l[n] * p[n] * \hat{g}_l^\dagger[-n] \tag{2.11}$$

Substituting (2.1) in (2.11) yields

$$z[n] = \sum_l a[n] * p[n] * g_l[n] * p[n] * \hat{g}_l^\dagger[-n] + w_l[n] * g_l^\dagger[-n] * p[n] \tag{2.12}$$

The PTR output, disregarding the noisy component of (2.12), may be rewritten as

$$z[n] = \sum_k I[n-k]Q[n] \tag{2.13}$$

with

$$I[n] = \sum_k s[k]R[n-k]; \quad R[n] = \sum_k p[k]p[n-k] \tag{2.14}$$

and

$$Q[n] = \sum_l \sum_k \hat{g}_l^\dagger[k]g_l[n-k] \tag{2.15}$$

The R-function is the auto-correlation of the pulse shape and the I-function is defined as

the convolution of the R-function and the transmitted signal. The Q-function represents the cross-correlation between the estimated and the actual CIR summed over the channels. The Q-function is particularly useful as an indicator of the PTR performance, since an impulse-like shape generally means a successful compensation of the multipath distortion. In real data processing the Q-function computation is precluded because, unlike for simulated cases where the actual Channel Impulse Responses (CIRs) are assumed known and are correlated with the corresponding CIR estimates and summed over the channels, with real data the actual CIRs are unknown and only CIR estimates are attainable. Thus, one may not to check whether the Q-function has impulse-like shape for the analysis of the PTR performance. However, an equivalent criterion can be used for measuring such performance by computing the PTR output power.

In order to obtain the CIR estimate $\hat{g}_l[n]$, the transmitted probe signal and the corresponding received noisy probe signal are required. Such CIR estimate can be contaminated by noise in different degrees depending on the adopted estimator. Sections 3.4, 3.5 and 3.6 present three estimators: Pulse Compression (PC) the classical minimum variance unbiased estimator, Regularized ℓ1-norm (RegL1) for sparse channels and Environmental Focalization (EF) inspired by matched field processing. The latter is the core of the proposed EPTR method.

A detailed description of the time-reversal technique in terms of matched filter approach is presented in [48], describing the Signal to Noise Ratio (SNR) equation for the output of a matched filter, and then extending the concept to the similar cases of Matched Field Processing (MFP) (that employs a modelled channel replica as matched filter) and the time-reversal (that employs a probe-based channel estimate as matched filter). The work concludes that

MFP and PTR may be cast as matched-filters and straightforwardly highlights the difference between MFP and PTR as the type of matched filter employed, which in the MFP case is a noise-free CIR replica and in the PTR case is a CIR estimate contaminated by noise, and therefore is shown to outperform PTR, under no or moderate model mismatch situations.

2.4 Pulse-compression channel estimation

The PTR processing requires a channel estimate, which in its conventional form is performed by pulse compression (PC), that is based on classical $\ell 2$-norm estimation. The PC can be derived from the Minimum Variance Unbiased estimator (MVU), as described in Appendix A.

Assuming a set of linear time-invariant systems corresponding to L hydrophones, with the *l-th* channel impulse response denoted by $\mathbf{g}_l$, the *l-th* received signal is given by

$$\mathbf{y}_l = \mathbf{S}\mathbf{g}_l + \mathbf{w}_l, \tag{2.16}$$

with $\mathbf{y}_l \in \mathbb{C}^{P\times 1}$, $\mathbf{g}_l \in \mathbb{C}^{J\times 1}$, $\mathbf{w}_l \in \mathbb{C}^{P\times 1}$ and $\mathbf{S} \in \mathbb{C}^{P\times J}$. Thus, the MVU estimator is

$$\hat{\mathbf{g}}_l = (\mathbf{S}^H\mathbf{S})^{-1}\mathbf{S}^H\mathbf{y}_l \tag{2.17}$$

and the estimator covariance is

$$\mathbf{C}_{\hat{\mathbf{g}}_l} = \sigma_{w_l}^2(\mathbf{S}^H\mathbf{S})^{-1}, \tag{2.18}$$

where σ_w^2 denotes the variance of additive white Gaussian noise. Note that the autocorrelation and cross-correlation properties of probe signal $\mathbf{s}$ directly affect the estimator performance, where it would be wise to use a probe that makes the matrix inversion in (2.17) to appear close to diagonal. This is because the estimator variance depends on the input signal matrix $\mathbf{S}^H\mathbf{S}$. Thus, aiming at minimizing the estimator variance, the input vector $\mathbf{s}$ must be

chosen to make $\mathbf{S}^H\mathbf{S}$ as near to diagonal as possible.

In the particular case of this matrix being identity, the PC is yielded by a simple cross-correlation solution that for the l-th hydrophone is given by

$$\hat{\mathbf{g}}_l = \mathbf{S}^H\mathbf{y}_l. \tag{2.19}$$

2.5 Regularized $\ell 1$-norm channel estimation

Shallow water communication channels are characterized by arrivals of wavefronts, being the CIR envelope shape generally formed by a few peaks representing path arrivals at particular delays. Thus, if the CIR time window is long enough, a vector representing the discrete CIR will have a few delays with high amplitude (*i.e.*, the arrival paths) and many other delays with very low amplitude. This characteristic leads us to the assumption that shallow water environment CIRs may be considered as sparse.

The concept of sparsity means that the number of significant elements in a vector (or matrix) is much smaller than the total dimensionality of the vector. Observing that the $\ell 0$-norm of a vector $\mathbf{x}$ equals the count of its nonzero elements, *i.e.*, $\|\mathbf{x}\|_0 = \{\#\ of\ n:\ x[n] \neq 0\}$, then the sparsity can be given by $\|\mathbf{x}\|_0 \ll \{\#\ of\ n:\ x[n]\}$.

Therefore, since a shallow water CIR is assumed sparse, its estimation can be done by employing sparse techniques for channel identification instead of classical $\ell 2$-norm-based estimation. In particular, this work employs Regularized $\ell 1$-norm (RegL1) [49] method for sparse channel estimation yielding improved accuracy, with side lobes and noise effects mitigation, due to the enhancement the most significant elements in a discrete CIR vector. It is inspired by Compressed Sensing (CS) theory [15, 50] and find applications in several study fields, among them, communication channel estimation.

The use of ℓ1-norm instead of ℓ0-norm is justified by the advantages of avoiding non-convex optimization problems, which are much harder to solve than convex optimization. The convexity issue can be shortly illustrated in reduced dimension (tri-dimensional basis, for the sake of clarity) by analyzing the ℓ2 hypersphere. Figure 2.4 shows in (a) to (d) the hyper-surfaces for the cases when norm are respectively ℓ0.5, ℓ1, ℓ2 and ℓ10 (the plane for a hypothetical $\mathbf{Ax} = \mathbf{b}$ system is not shown). The first case is clearly non-convex, requiring

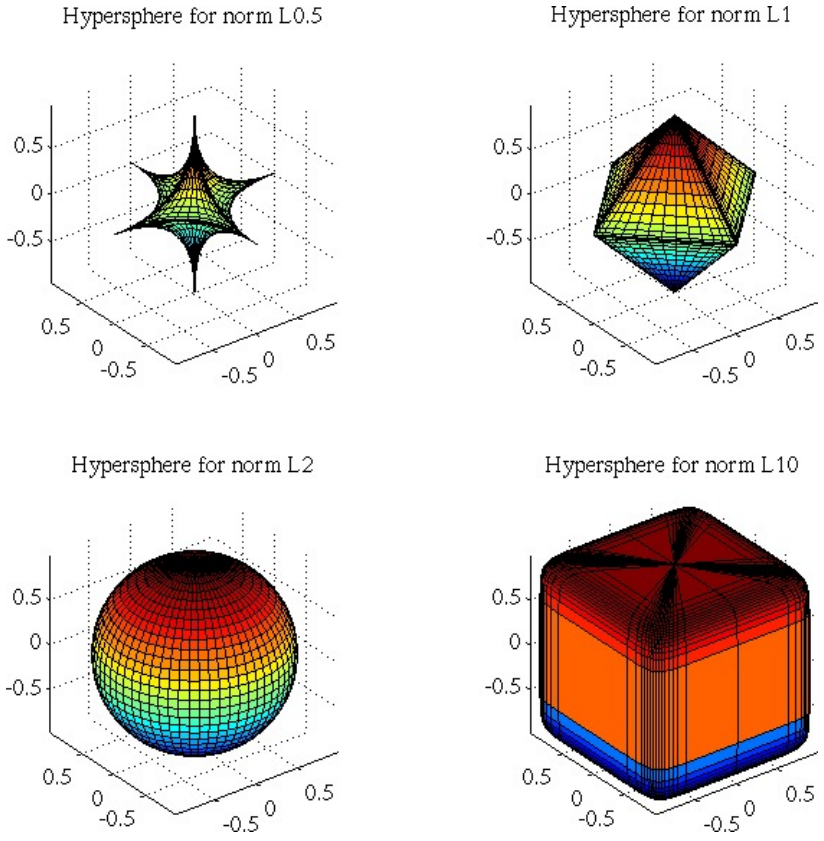

Figure 2.4: Snapshot of the hyper-surfaces for ℓ0.5, ℓ1, ℓ2 and $\ell_1$0-norm.

procedures to reach uniqueness. The other cases are convex and in particular the ℓ1-norm is the smaller norm that is still convex. Observe the expansion of each ℓ_p error sphere centered at origin, that then shall be blown until touching a plane representing the system $\mathbf{Ax} = \mathbf{b}$ (not shown). For the special case of the ℓ1-norm the hypersphere tends to find a solution that touches the plane in some point in the edge, so that the three coordinates of such point have

a particular value to an axis and null value to the other orthogonal axes. Thus, the point tends to be represented by a sparse 3-D vector. Although for higher dimensionality cases representation is not possible, the same idea is extended to the sparsity of higher dimension vectors.

Relaxing the $\ell 0$-norm to the $\ell 1$-norm, a straightforward suboptimal solution is yielded if the Restricted Isometry Property (RIP) described in [51] is accomplished. A method that solves the minimization problem is named Basis Pursuit [52], in which case convex optimization solutions can adopt an interior point method [53] or a greedy algorithm. The methods Least Angle Regression (LARS) [54] and Least Absolute Shrinkage and Selection Operator (LASSO) [55] are solvable with greedy algorithms, where the latter proposes to minimize the least square error subject to the $\ell 1$-norm of the solution vector that should be smaller than some noise threshold ϵ_w . Using an unconstrained optimization approach based on LASSO, the RegL1 estimator is given by

$$\hat{\mathbf{g}} = \arg\min_{\mathbf{g}} \{\frac{1}{2}\|\mathbf{S}\mathbf{g} - \mathbf{y}\|_2^2 + \gamma\|\mathbf{g}\|_1\} \tag{2.20}$$

where the scalar γ is a regularization parameter contained in the interval $[0, \infty)$. The derivation of (2.20) is described in Appendix B.

A suitable algorithm to solve this problem, among other options, is the Iterative Reweighed Least Squares (IRLS) [56]. Assume $\mathbf{G}$ as a diagonal matrix with $diag(\mathbf{G}) = |\mathbf{g}|$, thus we have $\|\mathbf{g}\|_1 \simeq \mathbf{g}^T\mathbf{G}^{-1}\mathbf{g}$. Note that the ℓ_1-norm is showed here as an adaptively-weighted version of the squared ℓ_2-norm. With this approximation, the problem to be solved is

$$\hat{\mathbf{g}} = \arg\min_{\mathbf{g}} \{\gamma\, \mathbf{g}^T\mathbf{G}_{k-1}^{-1}\mathbf{g} + \frac{1}{2}\|\mathbf{S}\mathbf{g} - \mathbf{y}\|_2^2\} \tag{2.21}$$

Since this problem does not have a closed form solution as is the case for the $\ell 2$-norm-based methods MVU and PC, it will require an iterative numerical algorithm. Thus, the quadratic optimization problem in (2.21) is solvable using linear algebra as shown in Table 2.1 [57].

Table 2.1: Procedure of IRLS for solving the quadratic optimization problem (2.21).

Initialize the iteration $k = 0$, set the initial approximation (chosen arbitrarily) $\mathbf{g}_0 = \mathbf{1}$ and set the initial weight matrix $\mathbf{G}_0 = \mathbf{I}$.
Achieve the main iteration with the increment of k by 1, and apply these steps:
1. Execute regularized least-squares to approximately solve the linear system $(2\lambda \mathbf{G}_{k-1}^{-1} + \mathbf{S}^T\mathbf{S})\mathbf{g} = \mathbf{S}^T\mathbf{y}$ iteratively (several conjugate- gradient iterations may suffice), producing result $\mathbf{g}_k$;
2. Update the diagonal weight matrix $\mathbf{G}$ using $\mathbf{g}_k$, with $G_k(j,j) = \lvert g_k(j)\rvert + \epsilon_w$; and
3. Verify the stopping rule in such form that if $\lVert g_k - g_{k-1}\rVert_2$ is smaller than some predetermined threshold, stop, or otherwise, apply another iteration.
The generated $\mathbf{g}_k$ is the RegL1 output.

2.6 Environmental focalization channel estimation

The environmental focalization processor aims at generating noise free channel replicas for time-reversal matched-filtering implementation of the PTR. This focalization is done over a given number of environment candidates and selects those that best match the PC or RegL1 CIR estimate extracted from the observed data.

In PC-EPTR mode, the PC estimated CIRs are used to select the "a posteriori" replicas from within an ensemble of possible channel responses generated from an "a priori" search space defined through a set of environmental parameters. This process of tweaking the environmental parameters to obtain a noise-free numerical model generated CIR that best matches the observed channel, is termed "environmental focalization" (EF). In RegL1-EPTR

mode, the process is the same except that RegL1 estimated CIRs are used instead of the PC estimated CIRs.

The details of the EF block section is given in the diagram of Fig. 2.5. The "a priori"

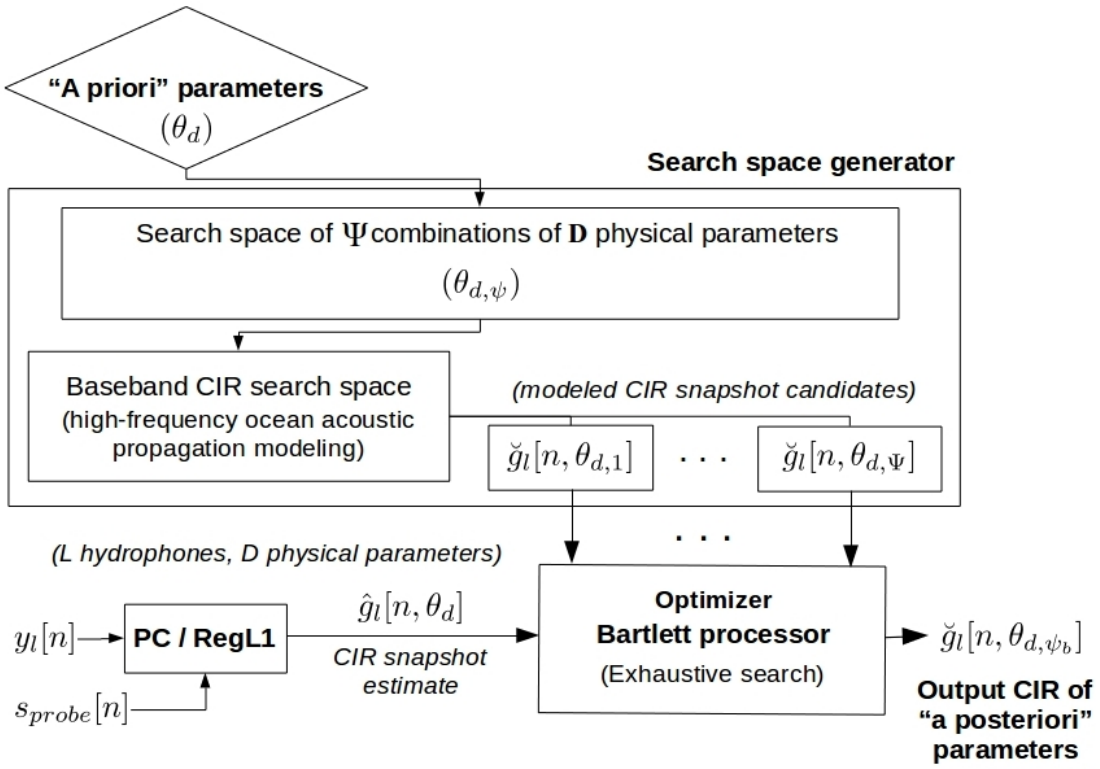

Figure 2.5: Block diagram of the environmental focalizer for EPTR implementation, which is used for obtaining the CIR replica from an "a priori" search space that best matches a CIR snapshot estimate. A set of "a priori" parameters are used to generate the search space of model-based CIR replicas which are optimized, in the sense of best match a CIR estimate, using exhaustive search with a Bartlett processor. The output are the "a posteriori" parameters and the corresponding noise-free CIR replica generated from these parameters.

physical parameters are provided by the user to the focalization block, in which the core optimization is performed. A search space generator creates Ψ combinations of D physical parameters where $\theta_{d,\phi}$ is the d-th physical parameter related to the ψ-th candidate replica in the search space. Thus, the corresponding ψ-th baseband equivalent modeled CIR snapshot with a particular set of parameters is generated for the l-th channel as $\breve{g}_l[n,\theta_{d,\phi}]$. After optimization by exhaustive search using the Bartlett processor [38] as objective function

that compares the replicas with the observed CIR estimate $\hat{g}_l[n, \theta_d]$ (obtained, *e.g.*, from PC or RegL1), the best match identified by the ψ_b replica is output as $\breve{g}_l[n, \theta_{d,\psi_b}]$.

In general, it is important to note that environmental focalization results depend on an appropriate choice of "a priori" search space data. For instance, the use of a search space too large can generate ambiguity and an unrealistic set of "a posteriori" CIRs, making the channel compensation to fail due to excessive mismatch in the output of the objective function optimization. On the opposite, a too narrow search space would not allow enough degrees of freedom for the model, potentially leading to severely biased CIR estimates.

In this work, the Bellhop and Bounce models [46] are jointly employed to simulate model-based CIRs. The scenario declared a priori can be a range dependent ocean waveguide with a layered seabed. The Bounce model computes the reflection coefficients of the layered bottom to be used as input for the Bellhop model which computes amplitudes and delays of arrival paths.

Successful results depend, in some degree, on an appropriate choice of the search space, which can be obtained by prior environmental assessment of the area of interest based on in-situ measurements or by using background historical data. The choice of the set of environmental parameters to be included in the search space is a compromise between a meaningful CIR model to mimic all CIRs during a given time frame and the computational load to run the optimization. A high number of optimization parameters may become quickly computationally prohibitive, due to the use of exhaustive search that compares all the replicas in the search space, thus requiring an appropriate search space size (*e.g.*, few thousand replicas). These two objectives converge to selecting environmental parameters along a hierarchical list from the most to the least influential parameters on the output

modeled acoustic field. This hierarchy is known to put on top of the list the geometrical parameters as for example source depth, source-receiver range, and receiver depth, and down on the list the geoacoustic parameters, in particular the density and compressional attenuation.

The optimization is performed using a Bartlett objective function to select a small set of refined CIR candidates that best correlate with the pulse-compressed or RegL1 estimated observed CIR. The objective function employed in this work is defined in time-domain by

$$B(\psi) = \frac{\breve{\mathbf{g}}_l^H[n, \theta_{d,\psi}]\, \mathbf{C}[n, \theta_d]\, \breve{\mathbf{g}}_{l,p}[n, \theta_{d,\psi}]}{\|\mathbf{g}_l(n, \theta_d]\|\, \|\breve{\mathbf{g}}_l(n, \theta_{d,\psi})\|}, \tag{2.22}$$

with the covariance matrix of observed data being

$$\mathbf{C}[n, \theta_m] = \frac{1}{P} \sum_{p=1}^{P} \mathbf{g}_{l,p}[n, \theta_d] \mathbf{g}_{l,p}^H[n, \theta_d], \tag{2.23}$$

where $\breve{\mathbf{g}}$ denotes the predicted CIR data, $\mathbf{g}$ denotes observed CIR data, P is the number of observations, the subscript l is the hydrophone number, H denotes conjugate transpose, θ_d is the *d-th* physical parameter in the CIR estimate and $\theta_{d,\psi}$ is the d-th physical parameter of the ψ-th CIR model-based replica generated in the search space. Using the maximum a posteriori criterion, the best fitness candidate is computed by performing $B_{MAP} = \max_{\psi \in \Psi} B(\psi)$, where Ψ is the set of all CIR replica candidates generated in the search space.

2.7 The Environmental-based Passive Time-Reversal

In this section the Environmental-based Passive Time Reversal receiver with model-based environmental focalization is presented. The conventional time-reversal receiver is modified to include the environmental focalization algorithm presented in the last section that employs a forward ray tracing model.

Figure 2.6 shows the block diagram of the communication receiver based on the EPTR processor. The figure shows the transmitted probe signal and the received pre-processed

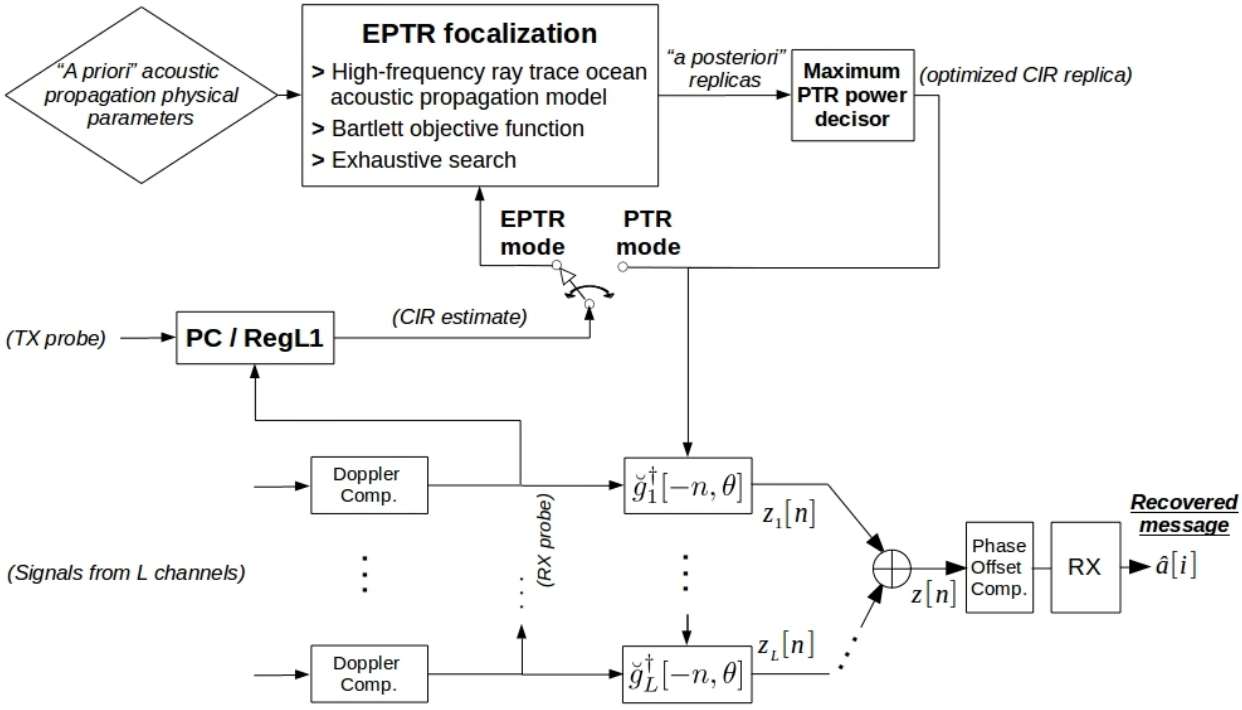

Figure 2.6: Block diagram of a single-input-multiple-output coherent communication receiver allowing for the implementation of either the standard pulse compressed Passive Time-Reversal or the Environmental-based Passive Time Reversal processors (see text for detailed explanation of the role of each block).

probe signals feeding the channel estimation processor (PC/RegL1) to yield the CIR estimate for each channel (*i.e.*, the observed CIR data). The pre-processing is relative to the Doppler compensation by appropriate resampling to remove the main Doppler trend and/or frequency clock drift impairments between transmitter and receivers. The Doppler analysis can be done by observing the Doppler Spreading Function (DSF) and the Doppler Spectrum (DS). In this context, the EPTR employs an algorithm to reject sensors in which the Doppler compensation failed. This procedure to block outliers sensors based on DS is described in Appendix C.

Also, the "a priori" physical parameters are given as input to the EPTR that then

performs environmental focalization using the EF algorithm, whose output is given by few "a posteriori" CIR replicas (configured in the present work to be ∼3 replicas). Such replicas feed the Maximum Power Decisor, which is employed to test those replicas under the criterion of maximize the PTR output power, aiming to optimize the Q-function (Eq. 2.15). The maximum power parameters set ψ_{mp} is given by

$$\psi_{mp} = \arg\max_{\psi_{output}} \frac{1}{N} \sum_{n=0}^{N-1} \mid \sum_{l} \breve{g}_l[n, \theta_{d,\psi_{output}}] * y_l^{\dagger}[-n] \mid^2, \tag{2.24}$$

where $*$ denotes convolution, $\dagger$ denotes conjugate and ψ_{output} denotes the set of parameters obtained as output of the inversion. Thus, the EPTR output signal is

$$z[n] = \sum_{l} \breve{g}_l[n, \theta_{d,\psi_{mp}}] * y_l^{\dagger}[-n]. \tag{2.25}$$

The maximum PTR power "a posteriori" CIR finally feeds the time-reversal filter of the particular channel. After summing, the time-reversal output is generated and after phase offset compensation the receiver performs the message recovery.

Chapter 3

Physical parameters sensitivity in simulated underwater communications

Preview *This chapter presents simulation results for physical parameter sensitivity tests in order to understand the influence of such parameters in shallow water time-reversal communications and further in environmental focalization processing. Section 3.1 discusses aspects of shallow water channels; Section 3.2 deals with the scenario for the parameters sensitivity testing; Section 3.3 presents the geoacoustic parameters simulations; and Section 3.4 presents the geometric parameters simulations for the sensitivity tests in a time-reversal receiver.*

3.1 Shallow water acoustic propagation

Shallow water acoustic propagation is introduced in this section aiming to highlight the main issues usually found in underwater communications that cause severe inter-symbol interference. Namely, the multipath, that causes CIR time spreading, and the time-variability, that causes CIR frequency spreading, are discussed. In addition, the bottom influence and the underwater unbounded channel bandwidth are briefly analyzed, before beginning the simulations in the following sections.

Consider an underwater source transmitting to a receiver in a scenario where the range is much larger than water depth such that the transmitted signal strongly interacts with the boundaries – the so-called waveguide effect or waveguide propagation. Figure 3.1 illustrates a

simplified overview of the general behavior of propagation in an underwater waveguide. The upward propagating rays are reflected on the free surface with inversion of phase; downward propagating rays are reflected in the bottom in two regimes: (i) those with grazing angles bellow the critical angle, defined as $\theta_c = \arccos(c_w/c_b)$, where c_w is the water sound speed near the boundary and c_b is the bottom sound speed; and (ii) those with grazing angles above the critical angle [58]. In regime (i), the rays penetrate the seabed with high slope and, at high frequencies, most of them vanish or are severely attenuated. In regime (ii), the rays have specular reflection keeping high energy in the water column, thus producing waveguide bound signal propagation.

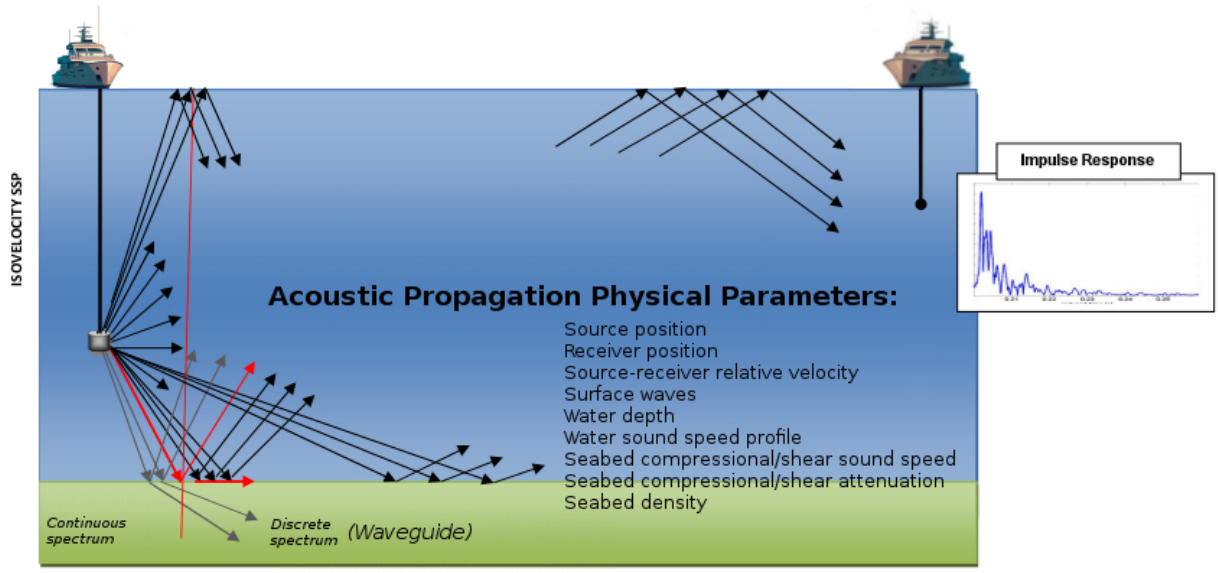

Figure 3.1: Simplified overview of the acoustic propagation regimes in shallow water forming a waveguide channel after the critical angle and the acoustic propagation physical parameters that affect the waveguide propagation. The envelope of an hypothetic channel impulse response is shown at right.

The physical processes in range-independent acoustic propagation are influenced by a set of physical parameters, which can be in general classified by a sound speed profile and two groups of parameters, namely the geometric parameters and the geoacoustic parameters.

The geometric parameters are: source depth, receiver depth, source-receiver range and water depth (that is a single value in the case of a range-independent transect or a set of values defined by the bathymetry in the case of a range-dependent transect). The geoacoustic parameters are: bottom density, compressional speed and compressional attenuation, if the seabed is assumed as a fluid layer, and additionally shear speed and shear attenuation, if the seabed is assumed as a viscoelastic layer. The seabed model can also assume a layered bottom, being usual to consider a fluid sediment layer with a particular thickness (*e.g.*, from a few meters to a few tens of meters) over a viscoelastic bottom infinite half-space. All the above physical parameters affect, in some particular degree, the channel impulse response (CIR), which can be defined as the output signal that results of the Linear Time-Invariant (LTI) system formed by source, underwater channel and receiver when an impulse is applied as input signal. The CIR is the Green's function solution of the wave equation and allow us to predict what the system's output would look like in the time domain by employing the convolution theorem for LTI systems. Furthermore, the accurate knowledge of the CIR is essential for channel compensation in underwater communication systems. In particular, PTR receivers are directly dependent of accurate CIR estimation or modelling.

The most important aspect in shallow water acoustic propagation is the formation of a waveguide channel. This means that propagation of the transmitted signal follows multiple paths, being some paths direct between source-receiver and other paths reflected in the boundaries, which can be modelled as the eigenrays of the ray tracing solution, which interfere with each other forming a complex acoustic field. The direct consequence is the CIR being characterized by a set of delayed arrivals each with a particular amplitude. Therefore the received signals are severely affected, specially if their duration is longer than

the time delay between two consecutive CIR arrivals. Others issues on acoustic propagation are the Doppler effect mainly caused by source-array motion or (unavoidable) sea surface motion, the bottom loss, the bathymetry effects and the bandwidth limitation mainly due to frequency-dependent attenuation. Figure 3.2 shows an overview of a shallow water modeled scenario of multipath propagation, showing the eigenrays connecting one source to multiple receivers, as it may happen in a unidirectional Single-Input-Multiple-Output (uni-SIMO) type of communication. The eigenrays' structure, *i.e.*, a series of ray paths connecting the source and the receivers are shown in magenta. Also, a few text boxes are shown in the figure to indicate the main issues that affect shallow water propagation. The wavefronts arriving at the vertical array of hydrophones are shown on the right, in a representation of hydrophone depths in the vertical axis versus delays in horizontal axis. Note the wavefronts of the several delayed peak arrivals as consequence of the multipath propagation. The next subsections presents a short description of the ray model and discusses the main issues affecting shallow water propagation (shown in the gray boxes of Fig. 3.2).

3.1.1 Waveguide multipath propagation

Shallow water waveguide channels are prone to multipath propagation due to multiple reflections in the upper free surface and the seabed. A pattern of multiple interferences occurs with the propagating rays, which can be modeled by one of the several options of physical models available in specialized websites (*e.g.*, [59, 60]), each one using a particular method to solve the wave equation, having particular accuracy and complexity.

Despite of the several model options, in underwater communications the ray tracing method is appropriate due to the use of high frequency asymptotes and the suitability to

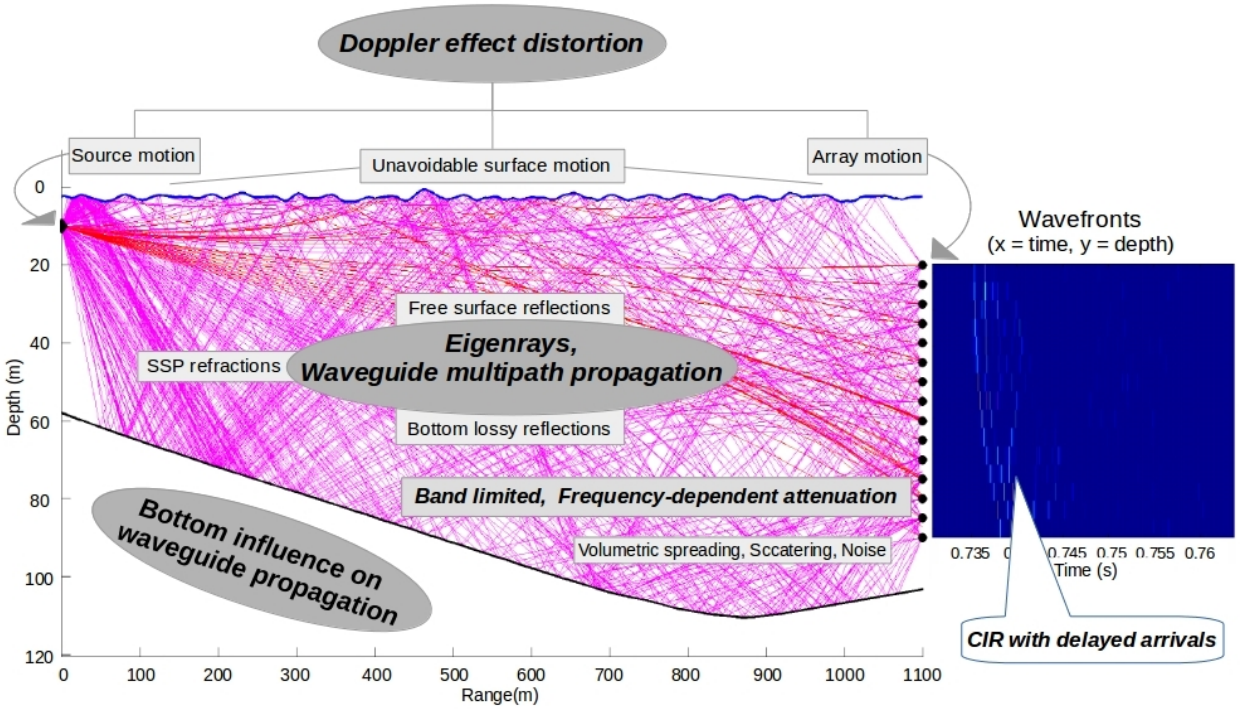

Figure 3.2: Main issues that affect the propagation in underwater acoustic waveguide channels. The scenario and its multipath structure (paths in magenta) are shown on the left. The wavefronts are shown on the right (color-plot in blue), showing the hydrophones depth in the vertical axis and time-delayed path arrivals in horizontal axis.

broadband signals. The channel model use physical parameters of the environment (*e.g.*, water sound speed profile, bottom sound speed, density and attenuation) and geometric parameters related to the sensors location (*e.g.*, source depth, receiver depth and source-receiver range) for computing the acoustic field. It can be used to compute path amplitudes and arrival times for simulating time-invariant snapshots of channel impulse response replicas. Also, using a set of sequential snapshots, one may obtain a two-dimensional time-variant channel impulse response, with the time window of impulse response in the horizontal axis and the evolution in time of the sequential CIR snapshots in the vertical axis.

Next we briefly describe (*i*) the ray tracing numerical solution of the wave equation that can be used to compute a time-invariant CIR snapshot in a particular instant and (*ii*) the time-variant CIR obtained from several sequential snapshots.

Ray tracing numerical solution of the wave equation

The ray trace model is appropriate for underwater acoustic communications systems, *e.g.*, employing frequencies in the band 10 kHz to 30 kHz, due to the high-frequency approximation inherent to its design [61]. This fact justifies the choice of the ray model to be used in this work as the forward model for environmental focalization. Furthermore, as described in [58], ray methods are used extensively for operational tasks where computation speed is a critical factor and environmental uncertainty poses severe constraints on the attainable accuracy.

The ray solution in an unbounded underwater media for a source located at $\vec{r_0} = (r_0, z_0)$ transmitting to a receiver at position $\vec{r} = (r, z)$, assuming two-dimensional Cartesian coordinates, can be obtained from the frequency domain version of the wave equation – the Helmholtz equation – as follows

$$\left[\nabla^2 + \omega^2/c(\vec{r})^2\right] \psi(\vec{r}, \omega) = -\delta(\vec{r} - \vec{r_0}), \tag{3.1}$$

where the angular frequency is ω and ψ is the potential displacement, whose relation to acoustic pressure $p(\vec{r}, t)$ in time domain and mean water density ρ is $p(\vec{r}, t) = -\rho \dfrac{\partial}{\partial t} \psi(\omega, t)$. Assuming plane wave approximation, it can be stated the ray series solution as follows

$$p(\vec{r}, \omega) = e^{-i\omega\tau(\vec{r})} \sum_{j=0}^{\infty} \frac{A_j(\vec{r})}{(i\omega)^j} \tag{3.2}$$

with $\tau(\vec{r})$ representing travel time and $A(\vec{r})$ representing envelope amplitude.

The travel times and complex amplitudes of the ray series are well-known in the literature, being solved by the Eikonal and Transport equations. The ray trace theory and numerical model is described in details in [58]. The inputs to the model are the physical parameters describing the channel, *i.e.*, the location and frequency regime of the source, the receivers location, the water sound speed profile and the geoacoustic parameters of the bottom (sound

speed, attenuation and density). Also, the model parameters "step", used to compute successive parts of the ray trajectories, and the "ray launching angles" must be given as initial condition for the model. The eigenrays, *i.e.*, the ray paths that connect the source and the specified receiver positions, are searched over a high number of rays computed by setting a large amount of ray launching angles. As described in [58], mathematically this is a root-finding problem, for which some solution methods are proposed, as, *e.g.*, interpolation and bending method, among others. Thus, the ray trace model output can be given by a set of travel times and complex amplitudes, each one corresponding to a path arrival of the linear time-invariant CIR.

Time-variant channel impulse response

Time-variability in underwater acoustic channels may be caused by unavoidable movement of the sea surface or by movement of source and receiver sensors. One may want to check if the channel variability along a transmission is too large, aiming to choose an appropriate equalization strategy. For instance, in the case of the PTR described in Chap. 2, the basic assumption is that the channel may be considered reasonably stable, since the method can not track channel variability. Thus, the time along which the PTR CIR estimate obtained from a single probe signal is valid will depend on the degree of channel variability along the transmission time. In other words, the channel coherence time, *i.e.*, the time duration over which the CIR is considered to be stable must be as large as possible.

The time-variability of the channel can be checked with using a two-dimensional (2D) CIR representation, which may be generated through the usage of a sequence of probe signals along the transmission time, aiming at computing a sequence of time-invariant snapshot CIR estimates that, in a discrete version, are organized as a matrix, where the horizontal axis

denotes the reduced time dimension at which path arrival delays are observed and the vertical axis denotes the snapshot time dimension at which the sequence of snapshots are observed.

Figure 3.3 shows an example of 2D CIR representation, obtained from real data of the UAN11 sea trial in May 24, 2011 (described in details later in Chapter 4), where a sequence of 20 probe transmissions with 2 kHz bandwidth centered at carrier frequency 26.5 kHz is used to estimate the channel in a 890 m range shallow water range-dependent transect with water depth between 30 and 100 m, for a source at 28 m and a hydrophone at 34 m. A 16 ms time window is used for each snapshot CIR and the time duration of the whole sequence of snapshots is 20 s.

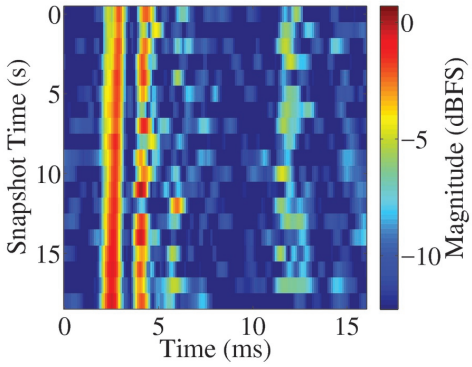

Figure 3.3: CIR in 2D representation, obtained from real data of the UAN11 sea trial in May 24, 2011, showing 20 snapshots of time-invariant CIR estimated with the classical method of pulse compression, each one with a 16 milliseconds duration. Multipath propagation effects are observed as the delayed arrivals along the horizontal time axis.

The 2D CIR estimate presents a strong arrival path at 3 ms, that is nearly stable along the 20 s duration of the sequence of snapshots (in fact, one may note a very slight trend in the travel time of this path along the transmission), followed by a smaller amplitude arrival path at 4 ms, with significant fading along the transmission, and a vanishing delayed arrival path at approximately 12 ms.

3.1.2 Doppler effect distortion

The movement of surface waves and transducers cause time-variability in an underwater channel, which in turn causes a Doppler effect due to the low speed of sound in water. In underwater communications the Doppler effect can be severe because even small movements are Doppler relevant due to the signal frequency and low wavelength. The receiver must compensate for the Doppler distortion before demodulation, being an usual procedure to employ resampling techniques.

Surface waves motion is mainly driven by the wind strength and causes Doppler effect due to the reflection of rays in moving scatter points. The main consequences are fading, random oscillating Doppler distortion and scattering loss. Surface displacement can be assumed to be a random process and, *e.g.*, the Pierson-Moskowitz wavenumber spectrum can be used to compute events of statistical representation of the sea surface [62]. At low frequencies the sea surface may be regarded as smooth, with total reflection of intensity at the specular angle [63]. However, at frequencies greater than approximately 2 kHz, this is no longer the case and the reduction of energy intensity must be taken into account for the sound scattered from the surface at non-specular angles. A model for both periodic-like and stochastic sea surfaces at short ranges is proposed in [64], considering a real shallow water range dependent waveguide.

Transducers motion often causes significant Doppler effect. Even in the case where the sensors are moored, small horizontal oscillations still occur and are relevant in underwater communications due to the use, in general, of high frequency signals (>8 kHz). In the case of existing intentional source-receiver movement, as *e.g.* when operating an autonomous

underwater vehicle, severe Doppler effects occur.

In shallow water waveguides, in presence of time-varying multipath propagation, each path is affected by a Doppler effect with a particular time compression or dilation factor, yielding frequency shift and spectrum distortion [65]. A simplified time-variant multipath with a single boundaries' reflection may be represented by the bi-scattering geometry model, which determines for a direct path between source and receiver and for a path reflected in a scatter point, the corresponding Doppler compression (or dilation) factor. The bi-scattering geometry model is briefly described in Appendix D.

For the analysis of the Doppler effect in underwater channels, one may want to use the Doppler Spreading Function (DSF) [66]. The DSF is obtained from the 2D CIR representation applying a Fourier transform over the snapshot time axis, thus yielding a frequency axis that allows to determine frequency shifts or spectrum distortion. In a discrete version, the DSF is a matrix where the horizontal axis denotes the reduced time dimension at which path arrival delays are observed and the vertical axis denotes the Doppler frequency. To obtain the discrete DSF, one may assume a 2D CIR $g[n,k]$, where n denotes time along snapshots and k denotes the delay time (see the example shown in Fig.3.3), and apply the discrete Fourier transform with respect to n, yielding the DSF $S[\phi,k]$, where ϕ denotes Doppler frequency, as follows

$$S[\phi,k]=\sum_{n=0}^{N-1} g[n,k]e^{-j(2\pi\phi n)/N} \tag{3.3}$$

Figure 3.4 shows an example of a DSF computed from a time-variant CIR estimate of 20 s duration containing 20 CIR snapshots of 16 ms, of Fig. 3.3. The environment is the same as that described in the previous section for the case of the 2D CIR.

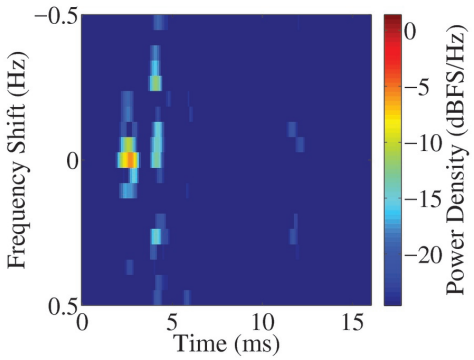

Figure 3.4: Example of DSF computed from the time-variant CIR, generated with 20 snapshot CIR of 16 ms, of Fig. 3.3.

The example in this figure presents a DSF with a strong arrival path at 3 ms, which has low Doppler shift, followed by an arrival path at 4 ms with significant Doppler shifts of +-0.3 Hz and a vanishing delayed arrival path at 12 ms with Doppler shift at 0.1 Hz and -0.3 Hz.

3.1.3 Bottom influence

The simplest seabed model is a range independent water column over an infinite half-space fluid bottom, which seldom represents realistic scenarios. A more elaborated seabed model may be obtained assuming a variable range-dependent bathymetry over a layered seabed where there are, *e.g.*, a fluid sediment layer over a viscoelastic half-space.

The bottom influence on waveguide acoustic propagation can be modeled in terms of reflection coefficients in the water-bottom interface. This procedure is particularly useful to represent a layered bottom and can be employed in the Bellhop ray trace acoustic propagation model [46], using a reflection coefficient table as input. Such table can be previously computed with the Bounce model [47]. The joint usage of these two models is used in this work to simulate a layered seabed assumed as a sediment layer over a bottom half-space.

In the case of a fluid sediment layer over a viscoelastic bottom half-space seabed, the

reflection coefficients can be calculated as a function of the acoustic impedance in water ($Z_{p,1}$), the acoustic impedance in fluid sediment layer ($Z_{p,2}$) with thickness h_2, the viscoelastic bottom compressional/shear impedances ($Z_{p,3}$ and $Z_{s,3}$), the corresponding incidence angles ($\theta_{p,i}$, $i = 1, 2, 3$ and $\theta_{s,3}$, relative to horizontal), the angle-dependent vertical phase delay for a path crossing the sediment layer ϕ_2 and the Rayleigh roughness parameter Γ due to a random rough surface. As described in detail in [58], the reflection coefficient for such three layer model (i.e., water column, fluid sediment layer, viscoelastic bottom half-space) is given by

$$R = \frac{Z_{p,2}(Z_{tot,3} - Z_{p,1} - i(Z_{p,2}^2 - Z_{p,1}Z_{tot,3})\tan\phi_2}{Z_{p,2}(Z_{tot,3} + Z_{p,1} - i(Z_{p,2}^2 + Z_{p,1}Z_{tot,3})\tan\phi_2} e^{-0.5\Gamma^2}, \tag{3.4}$$

where the total acoustic impedance in the viscoelastic layer is

$$Z_{tot,3} = Z_{p,3}\cos^2(2\theta_{s,3}) + Z_{s,3}\sin^2(2\theta_{s,3}), \tag{3.5}$$

the compressional and shear acoustic impedances are given respectively by

$$Z_{p,i} = \rho_i c_{p,i}/\sin\theta_{p,i},\ i = 1, 2, 3; \qquad Z_{s,i} = \rho_i c_{s,i}/\sin\theta_{s,i},\ i = 3, \tag{3.6}$$

the angle-dependent vertical phase delay for a path crossing the sediment layer is

$$\phi_2 \approx 2\pi \frac{h_2}{c_{p,2}} f sin\theta_{p,2}, \tag{3.7}$$

and the reflection angles calculated with the Snell's law are given by

$$\theta_{p,i} = \arccos\left(\frac{c_{p,i}}{c_{p,i-1}}\cos\theta_{p,i-1}\right),\ i = 2, 3; \qquad \theta_{s,2} = \arccos\left(\frac{c_{s,2}}{c_{p,i-1}}\cos\theta_{p,i-1}\right),\ i = 3. \tag{3.8}$$

The density is denoted by ρ and compressional and shear sound speed are c_p and c_s, respectively, f denotes frequency and h_2 denotes the sediment layer thickness.

Also, a critical angle occurs when the cosine of the incidence angles $\cos\theta_{p,1}$ become

negative and $c_{p,2} > c_{p,1}$. This critical angle is computed by

$$\theta_{p,i} = \arccos\left(\frac{c_{p,2}}{c_{p,1}}\right). \tag{3.9}$$

The bottom loss is given by $BL = -10\log|R|^2$. It is useful for the physical analysis of communication channels to verify the bottom loss behavior in medium-high frequency regime (greater than ∼8 kHz) and compare it to the low frequency regime (up to 2 kHz) usual in classical acoustic propagation problems.

Figure 3.5 shows the bottom loss calculated from the reflection coefficients computed by the Bounce model for the low-frequency band, from 0.5 kHz to 2 kHz (a and c), and for the high-frequency band, from 2 kHz to 30 kHz (b and d). It was assumed a sediment layer of 2 m thickness to generate the sub-figures in the top row (a and b) and a sediment layer of 5 m thickness for the sub-figures in the bottom row (c and d). The geoacoustic parameters used in this simulation are shown in Table 3.1.

Table 3.1: Geoacoustic parameters used to compute the bottom loss of Fig. 3.5.

	Geoacoustic parameters		
Layer	Sound speed (m/s)	Attenuation (dB/λ)	Density (g/cm^3)
Water	1484 ($98m$ depth)	0.0	1.0
Sediments layer	1550	0.2	1.5
Bottom half-space	1800	0.5	2.0

These figures show two distinct behaviors of the bottom reflection loss in terms of grazing angle: a region before the critical angle (which is identified in the figure by the abrupt change in bottom loss value) and a region after the critical angle. The former region represents the far field where the bottom reflection is high (low bottom loss), being identified as the red region in the figures. The latter region represents the near field where the bottom reflection is low, identified as the blue region.

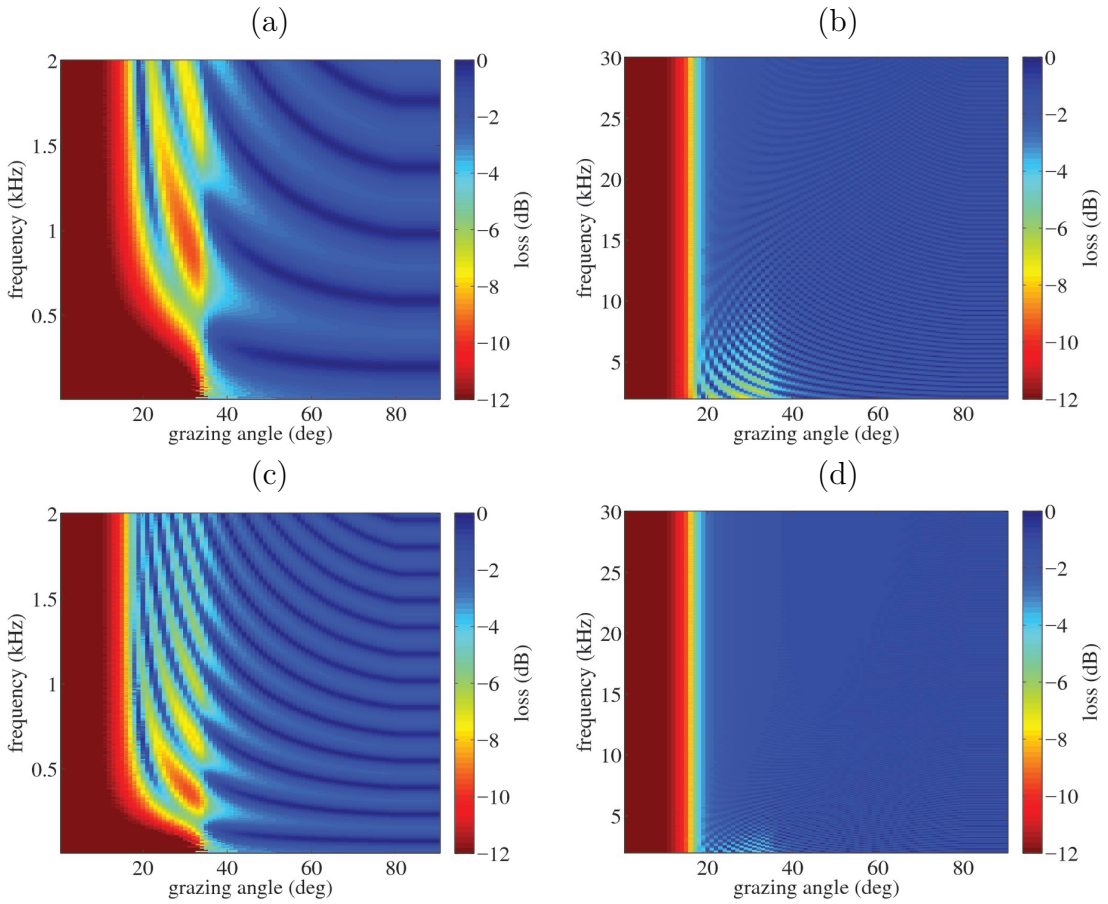

Figure 3.5: Bottom reflection loss calculated with parameters of Table 3.1 for a low-frequency regime (a and c) and a high-frequency regime (b and d). Sediment layer with 2 m thickness (a and b) and 5 m thickness (c and d).

In the results with the low-frequency band showed in Fig. 3.5 (a) and (c), the critical angle occurred in the interval between 19 and 38 degrees and there is an oscillating behavior of bottom loss in the near field. For the test using the high-frequency band (>8kHz) showed in Fig. 3.5 (b) and (d), the critical angle occurred at ∼19 degrees and the bottom loss has a flat behavior both for the far and for the near field. The oscillations in the near field found in the low-frequency band can be explained by the component $tan\ \phi_2$ in (3.7), where the angle-dependent vertical phase delay ϕ_2 for a path crossing the sediment layer is directly proportional to the frequency, to the sediment layer thickness and to a sinusoid driven by the incident angle due to the component $sin\theta_{p,2}$ in (3.7). Thus, large values of layer thickness

and/or frequency take $tan\ \phi_2$ to a nearly constant region of the tangent function, which makes the oscillation of the dumped sinusoid in (3.7). These figures indicate that at very short range (*i.e.*, in the near field where the grazing angles relative to horizontal are greater than the critical angle) the energy is severely attenuated without oscillations in magnitude for frequencies greater than 8 kHz exactly those usually employed in underwater acoustic communications.

3.1.4 Bandwidth limitation in unbounded acoustic propagation

In the ocean the attenuation of acoustic waves is frequency-dependent and approximately proportional to the square of the signal frequency [11]. Frequency selective attenuation limits the channel bandwidth, which makes the maximum data rate to be limited as well since the pulse bandwidth must be designed to have smaller bandwidth than the channel.

The limited channel bandwidth requires the choice of an appropriate carrier frequency and pulse interval. A short pulse interval is chosen to increase data rate but must satisfy the channel bandwidth limitation. In addition, note that the smaller the pulse time interval chosen for a communications system increased data rate, the better the system's ability to avoid loss of coherence due to channel variability. The implications that time variability in multipath channel bears on the high-speed communication system design are twofold, as Stojanovic describes [67]: signaling at a high rate causes many adjacent symbols to interfere at the receiver, requiring sophisticated processing to compensate for the ISI; nonetheless, as pulse interval becomes shorter, channel variation over a single symbol interval becomes slower. Therefore, there is a compromise between ISI distortion and channel coherence, that one should be concerned with, when designing the system data rate. Low data rate

(large pulse interval) decreases distortion due to ISI but increase distortion due to channel variation (channel tends to have less coherence); and high data rate decreases distortion due to channel variation but increase distortion due to ISI.

Carrier frequency and pulse bandwidth should be designed accordingly to the requirements imposed by the underwater channel[1]. Depending on frequency and range, the expected losses for unbounded propagation caused by volume attenuation (composed by volume scattering and absorption), volume spreading and ambient noise can be computed, giving an approximation of suitable regions to set the carrier frequency and pulse bandwidth.

Volume attenuation can be computed by an expression for the frequency dependence of the attenuation, as follows [58]

$$\alpha = 3.3 \times 10^{-3} + (0.11f^2)/(1 + f^2) + (44f^2)/(4100 + f^2) + 3 \times 10{-}4f^2 \tag{3.10}$$

with frequency f in kHz and attenuation factor α in dB/km. The volume spreading of a point source transmitting in an unbounded media is given by spherical spreading, *i.e.*, with losses proportional to the inverse of the square range. Ambient ocean acoustic noise can be man-made shipping noise, usually near harbors, or natural, caused by wind, waves, earthquakes or biological. A well-known summary of the spectrum of noise was compiled by Wenz [68, 58] indicating that noise have weaker sound pressure level at high-frequency due to ocean acoustic propagation and that the most influent component is wind noise, which is usually parameterized according to wind force. Figure 3.6 shows a simulation of the Transmission Loss (TL) in a unbounded media as function of range in km and frequency in kHz, using as input the inverse product of volume attenuation of (3.10), spherical volume

[1]In fact, there are also other practical requirements as, *e.g.*, transducer characteristics, size, power consumption, but they are out of the scope of this analysis.

spreading and ambient noise (spectrum of Wenz). Thus, in dB scale the curves are given by $TL = -(\alpha + 20logR + NL)$, where α is the volume attenuation in given by (3.10) in dB, R denotes range in m and NL is the sound pressure level of ambient noise in dB given by the Wenz's table [58].

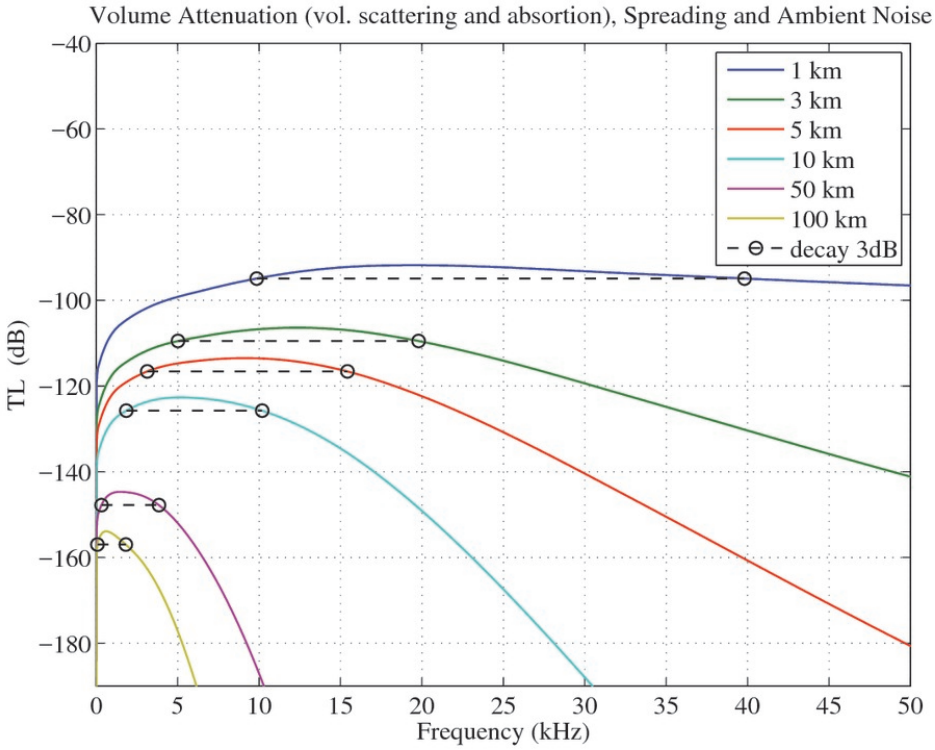

Figure 3.6: TL (dB) for unbounded media propagation as function of frequency and parametrized by source-receiver range.

For this particular case, of unbounded propagation, the most appropriate region in terms of reduced loss are indicated for each curve with a dashed line that denotes -3 dB decay, *i.e.*, half energy in linear scale. Therefore, assuming *e.g.* a source receiver range of 1 km in unbounded media, an appropriate carrier frequency could be some value between 10 and 40 kHz.

Note that the above computation is for an unbounded media instead of a shallow water waveguide. In shallow water multiple paths interaction causes a complicated pattern of

interferences, and the TL must be determined by a physical acoustic propagation model.

3.2 Scenario for parameter sensitivity testing

This section presents the scenario that is employed for all the simulation tests, considering that in the next sections simulations for sensitivity to geoacoustic and geometric parameters are performed aiming to reach physical knowledge useful for the environmental focalization in the EPTR.

A QPSK unidirecional-Single-Input-Multiple-Output (uni-SIMO) link with carrier frequency 12 kHz is simulated for a waveguide scenario with water depth 84 m range-independent transect, where a source at 40 m depth transmits to a 14 hydrophones vertical array positioned at 3 km range. Figure 3.7 shows the scenario with the channel physical parameters and the communications parameters. Figure 3.8 shows the sound speed profile for the simulated scenario, that is based on a real CTD profile.

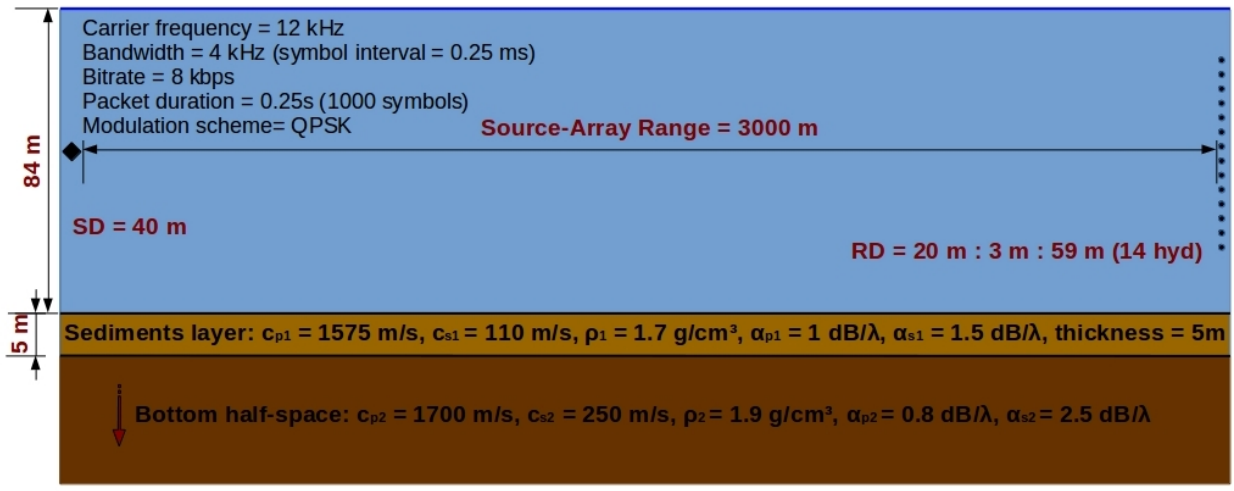

Figure 3.7: Simulation scenario with the channel physical parameters and the system setup parameters.

Each geometric and geoacoustic parameter varies separately for a series of model runs,

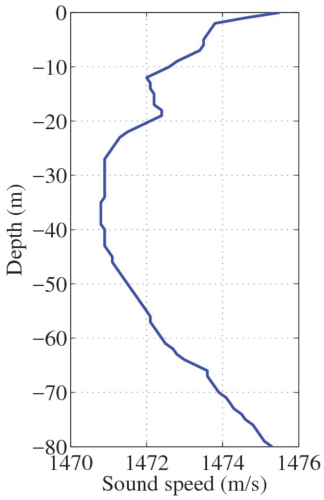

Figure 3.8: Sound speed profile relative to the scenario for parameter sensitivity testing.

in a procedure that aims to represent the influence of each parameter on the high-frequency acoustic field. The received signals constellation after being processed with a standard time-reversal receiver are also generated along the tests to observe the corresponding effects.

The approach for the parameters' sensitivity testing is to use a physical model to simulate the actual CIR assuming a set of parameters and to simulate several estimated CIR computed by assuming several mismatch values of a particular parameter that is being tested. These CIR estimates are used in the time-reversal filtering.

The standard PTR processing is performed and its output is, after appropriate down-sampling and demodulation, presented in a constellation diagram of the demodulated symbols to check the effects caused by the physical parameter mismatch. The CIR representing the actual channel is modeled according to the scenario of Fig. 3.7.

The parameters' sensitivity tests are performed for communication channels simulated with the Bellhop ray tracing model [46], which is used to compute amplitudes and delays of arrival paths of the time-invariant CIR. A fluid sediment layer is included in the bottom

model, as shown in Fig. 3.7, aiming at obtaining a more realistic scenario. To include the layered bottom, a set of equivalent reflection coefficients are computed with the Bounce model [47] and then the generated coefficients table is then used as input to the Bellhop model. The constellations are generated as output of a standard time-reversal receiver.

3.3 PTR sensitivity to geoacoustic parameters

The geoacoustic parameter simulations in high frequency propagation is divided in two stages. In the first stage, each geoacoustic parameter of the sediment layer is separately varied to observe the effects over the channel as well as the effects in the time reversal output due to using the mismatch CIR replicas as the CIR estimates that feed the time-reversal filters. In the second stage, typical seabed with realistic geoacoustic parameter combination are used to simulate the CIR, and thus the effects in the time-reversal receiver are checked in the same manner done in the first stage of the testing.

From a physical viewpoint the distortion of a particular seabed parameter without changing the others parameters is non-realistic, since, in some cases, there is correlation between bottom parameters, so one can not vary independently from the others. However, this procedure is still useful to indicate on how each physical parameter affects the acoustic field and thus the coherent signal demodulation. For inversion and focalization, the understanding of the influence of each parameter may help to generate an appropriate setting of the "a priori" parameter search space for optimization.

3.3.1 Sensitivity to the compressional speed in the sediment layer

The compressional sound speed (c_p) in the sediment layer is tested for a range of values published by Hamilton in [45], which is summarized in Table 3.2 for a series of typical

bottom types.

Table 3.2: Geoacoustic properties of continental shelf and slope environments [45].

Bottom type	ρ (g/cm^3)	c_p (m/s)	α_p (dB/λ)
Clay	1.5	1500	0.2
Silt	1.7	1575	1.0
Sand	1.9	1650	0.8
Gravel	2.0	1800	0.6
Moraine	2.1	1950	0.4
Chalk	2.2	2400	0.2
Limestone	2.4	3000	0.1
Basalt	2.7	5250	0.1

Table 3.3 shows the range tested for the compressional speed in the sediment layer from 1570 to 3030 m/s, equally spaced at $\Delta c = 20$ m/s.

Table 3.3: Sediment compressional sound speed for the sensitivity simulated test.

Parameter	**Lower limit**	**Upper limit**	**Step**
c_p (m/s)	1570	3030	20

Figure 3.9 shows the reflection coefficient for a low value 1570 m/s and a high value 2140 m/s of sediment sound speed in (a) and (b), respectively, with magnitude (blue) and phase (green). The figure clearly indicates that the compressional speed in the sediment is directly related with critical angle and magnitude of the reflection coefficient. The phase angles increase before the critical angle in both cases (a) and (b), and practically don't change after it. The critical angle is identified in (a) and (b) by an abrupt change in magnitude and phase (like a threshold effect) as the grazing angle increases.

Figure 3.10 shows the simulated CIR for a low value 1690 m/s (a), a medium value 1990 m/s (b) and a large value 2770 m/s (c). It clearly indicates that CIR time spread increases with sediment sound speed. This behavior causes changing in the position of the path delays

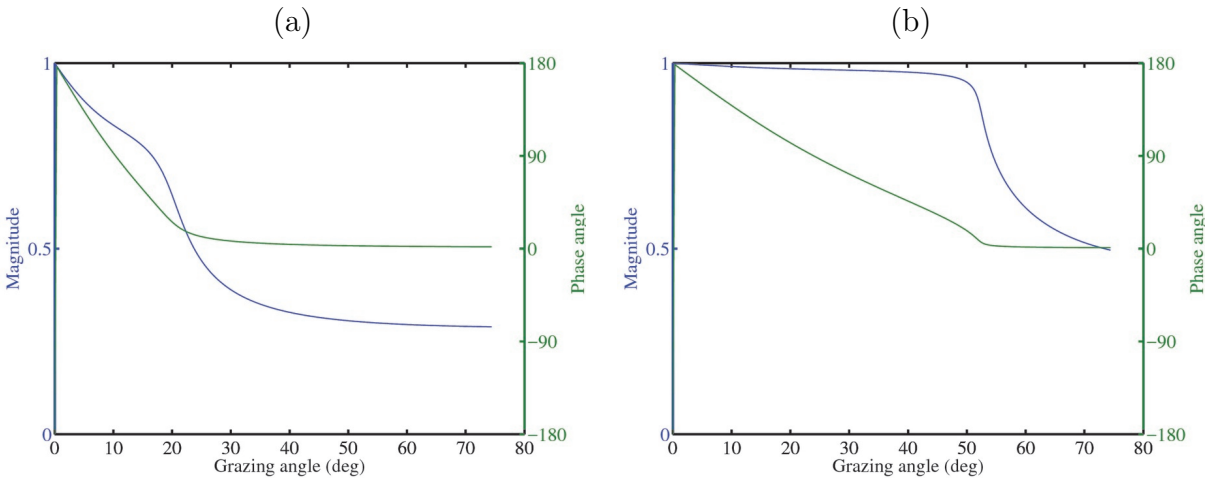

Figure 3.9: Sediment sound speed effects. The reflection coefficient for a low value (a) and a high value (b) of sound speed in the sediment layer.

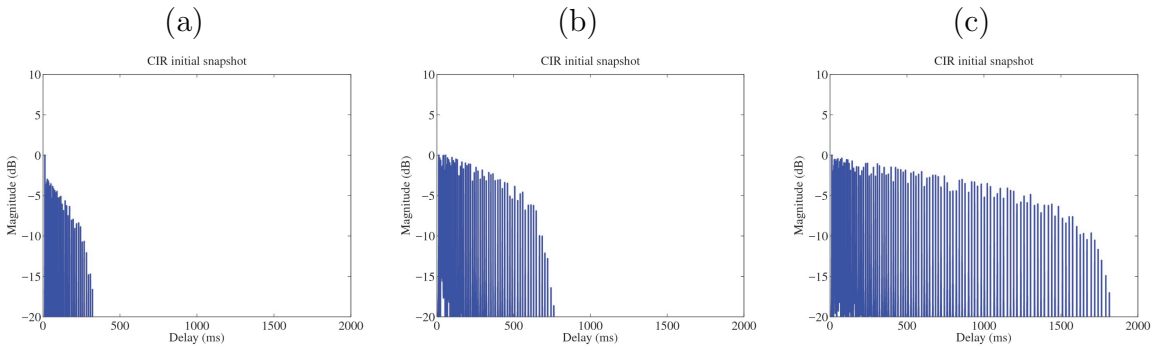

Figure 3.10: Simulated channel impulse responses for a low value 1690 m/s (a), a mean value 1990 m/s (b) and a high value 2770 m/s (c) of sediment sound speed.

along the time axis.

Figure 3.11 shows a brief representation of the most significant trends observed in the sensitivity test for compressional sound speed in the sediment, in terms of reflection coefficient, CIR snapshot and constellation diagram. This figure indicates that when the sediment compressional speed increases the following effects occur: (i) the critical angle increases, as expected, given that it depends of the sediments sound speed through the relation $\theta_c = \arccos(c_{water}/c_{sed})$; ($ii$) the magnitude of the reflection coefficient increases, due to the higher sediment compressional speed relative to the water sound speed, making the corresponding impedance (given by $Z_{sed} = \rho_{sed} c_{sed}$) to be higher than in the water; (iii)

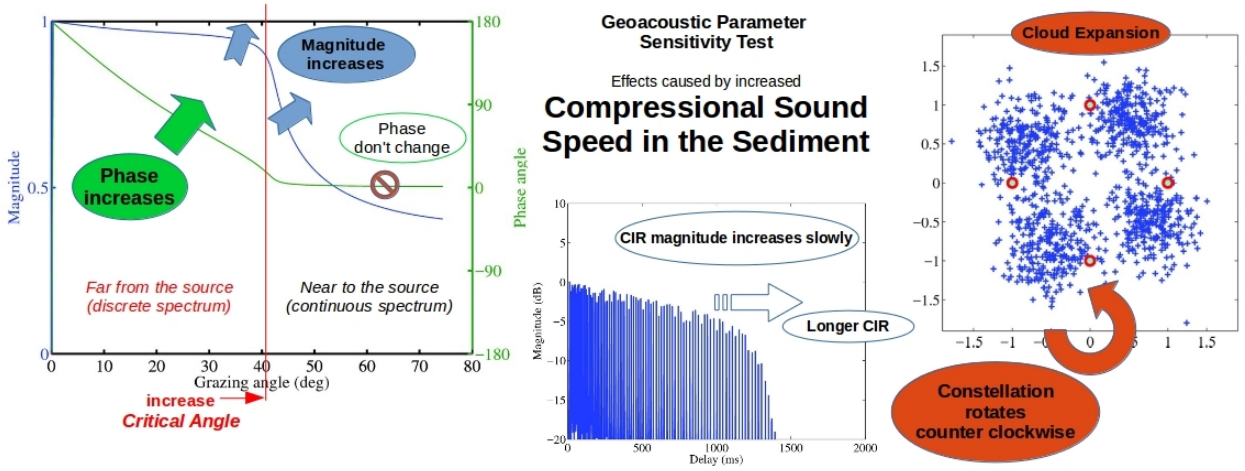

Figure 3.11: Variation of compressional sound speed in sediment layer ($5m$) over bottom half space (case of $c_{p1} = 1990$ m/s shown).

the reflection coefficient phase increases in the far field (*i.e.*, before the θ_c); (*iv*) the time duration of the CIR increases due to the higher level of reflection (explained in *ii*); and (*v*) the received constellations, after being processed by a standard time-reversal tend to rotate counterclockwise expanding slightly the symbol clusters. The clusters rotation and expansion may be explained by the fact that when we vary c_p to higher values, the physical model generates a bottom more reflective, where the CIR spreads and thus path distortions occur in amplitude and delay shift. Consequently, these distortions in the CIR estimates used for PTR filtering cause mismatches with the actual CIR in the PTR Q-function (given by the cross-correlation between the CIR estimate and the actual CIR, summed over all the channels) that yields phase shift and amplitude changes in the PTR output demodulated symbols. Such distortions of amplitude and delay shift are observed as cluster expansion and rotation in the QPSK constellation diagram.

To shortly illustrate the mismatches expected in the Q-function due to the path delayed CIR caused by variations in c_p, Fig. 3.12 shows on the left column the hypothetic actual

CIR 1 and its tap-delayed versions CIR 2 and CIR 3, representing effects of varying c_p; and on the right column the auto-correlation of CIR1 (in reference to an ideal Q-function with no mismatch between CIR estimate and the actual CIR) and the cross-correlation of CIR1 with CIR2 and of CIR 1 with CIR3. These cross-correlations clearly indicates that there

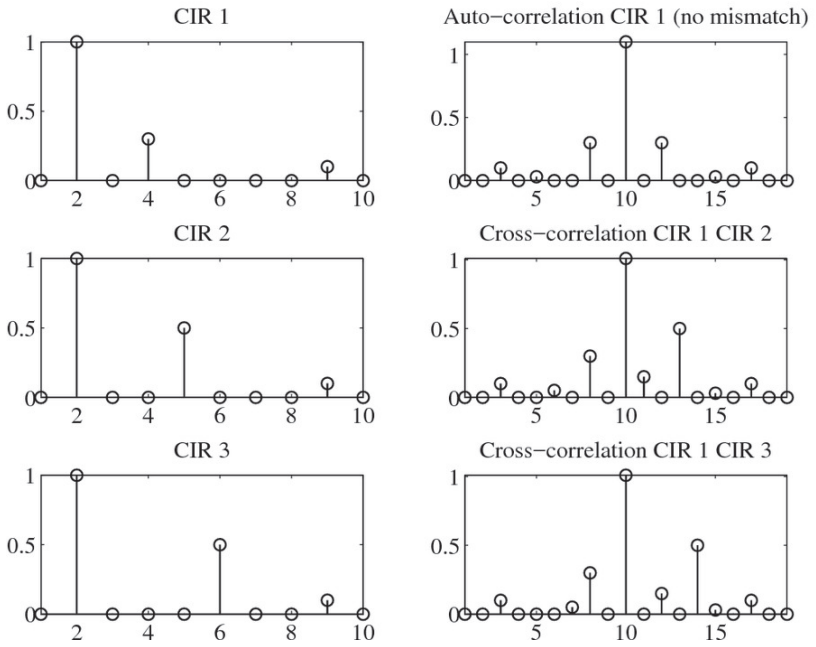

Figure 3.12: On the left column are shown an hypothetic CIR, named "CIR 1" and its tap delayed versions "CIR 2" and "CIR3". On the right column are the auto-correlation of "CIR 1" and its cross-correlation with the tap delayed "CIR 2" and "CIR 3". The CIR mismatch caused by delayed taps generates a cross-correlation with delayed side lobes, suggesting that some delayed residual side lobe may eventually occurs in the Q-function of PTR. Delayed side lobe in the Q-function would cause phase rotation in the PTR output.

is a path shift caused by the mismatches of CIR 2 and CIR 3 relative to CIR1, suggesting that the PTR Q-function will have a delay shift that causes phase shift in the PTR output demodulated symbols.

Therefore, the sediment compressional sound speed variation causes significant changes in the CIR in terms of delays of arrival paths, which is a remarkable feature for PTR. The accuracy with which such delays are modeled is an important issue in channel estimation

for PTR communications affecting directly channel compensation performance. In a model-based channel compensation processor, the importance of that parameter among the other sediment parameters is high. In environmental focalization, this feature can be explored to "a priori" select an appropriate set of CIR candidate replicas as input to the focalization processor through the increase of the resolution of this parameter, *i.e.*, giving a dense number of values of the parameter as input, in comparison to the others prior physical parameters.

3.3.2 Sensitivity to the density

Following, sediment density (ρ) testing performed for a range of realistic values is shown in Table 3.4 , based on those of Table 3.2.

Table 3.4: Sediment density variation range for the sensitivity simulated test.

Parameter	**Lower limit**	**Upper limit**	**Step**
ρ (g/cm^3)	1.70	2.65	0.05

Figure 3.13 shows the reflection coefficients for the minimum 1.70 g/cm^3 and maximum 2.65 g/cm^3 values of the sediment density in (a) and (b), respectively, where it can be observed that the magnitude increases after the critical angle, the phase slightly decreases before the critical angle and otherwise remains approximately unchanged. Also, the critical angle is constant at approximately 20 degrees.

Fig. 3.14 shows the significant trends observed in the present results for variation of density in sediment. The results obtained for the physical model in this test indicate that when the sediment density increases: (i) the critical angle do not change, as expected, because it is a function of c_p, as shown in (3.9), and thus independent of ρ; (ii) the magnitude of the reflection coefficients increases, which can be explained by the acoustic impedance (Z)

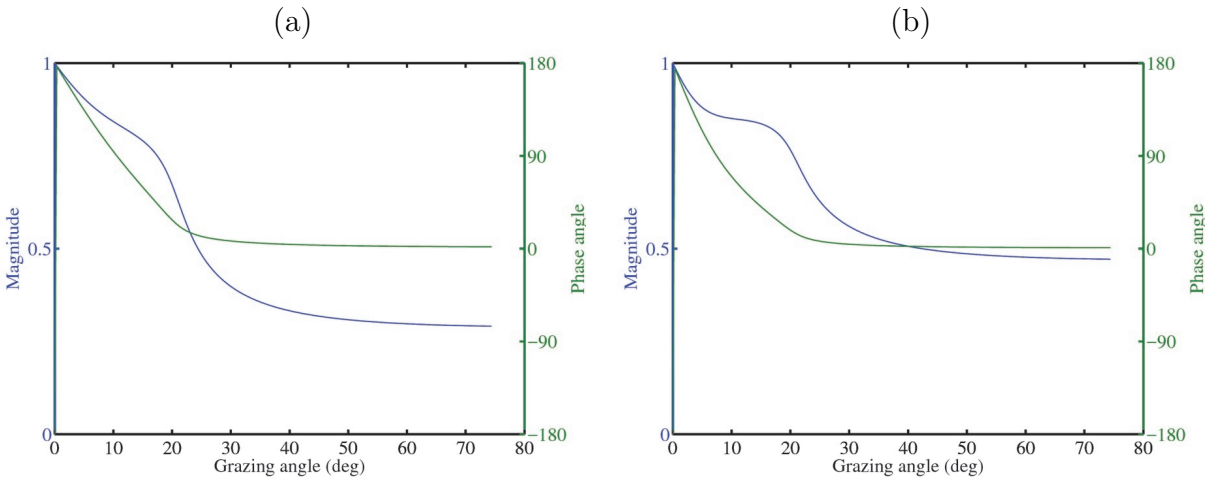

Figure 3.13: Reflection coefficient versus grazing angle for the minimum 1.70 g/cm^3 (a) and maximum 2.65 g/cm^3 (b) values in the range for the sediment density parameter.

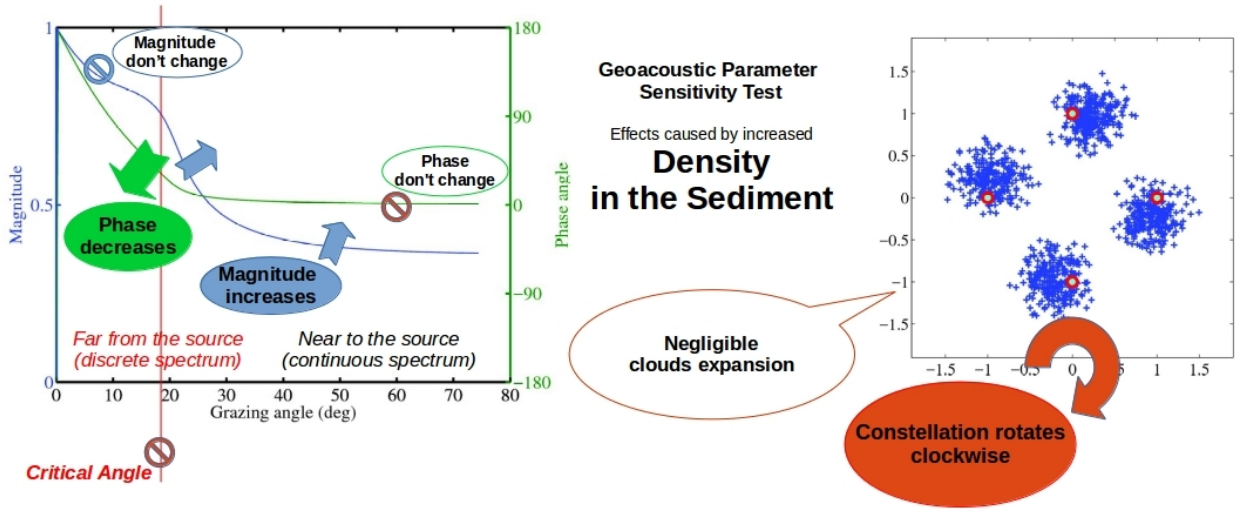

Figure 3.14: Density in sediment layer $(5m)$ over bottom half space testing.

being directly proportional to the density ($Z = \rho c_p$) and thus the reflectivity increases when the density increases; (iii) the reflection coefficient phases do not change in the near field, which is an effect less obvious than that the reflection coefficient magnitude, being obtained as a solution of (3.4) ; (iv) the CIR time spreading does not change significantly (not shown); and (v) the received PTR compensated constellation rotates clockwise and expands slightly. The reason for ρ to cause slight constellation rotation may be due to slight effects of delay shift in the CIR paths, in a process with the same nature than for the compressional speed

c_p but in small scale, since both c_p and ρ are directly proportional to Z, which affects the bottom reflectivity.

The varying of density in sediment layer is less important to the environmental focalization than the compressional speed since the CIR mostly changes path magnitude and have small effect on the path delays. Nonetheless, even the small effect on the path delays may be the probable cause of the slight constellation rotation which indicates that, although small, an influence still occurs in the acoustic field and it should be considered in the choice of search space for environmental focalization.

3.3.3 Sensitivity to the compressional attenuation

Table 3.5 shows the range of variation of compressional attenuation (α_p) used for this simulation sensitivity test.

Table 3.5: Compressional attenuation variation range for the sensitivity simulated test.

Parameter	**Lower limit**	**Upper limit**	**Step**
α_p (dB/λ)	0.10	1.05	0.05

Figure 3.15 shows the reflection coefficients for the minimum 0.10 dB/λ and maximum 1.05 dB/λ values of the compressional attenuation parameter in (a) and (b), respectively. One can observe that the magnitude decreases decreases for angles smaller than the critical angle and otherwise the magnitude and phase remains approximately unchanged, as well as the critical angle.

Figure 3.16 shows the significant trends observed in the present results for variation of attenuation in sediment. The results for the compressional attenuation of the physical model indicate that when it increases: (i) the critical angle does not change, as expected, due to

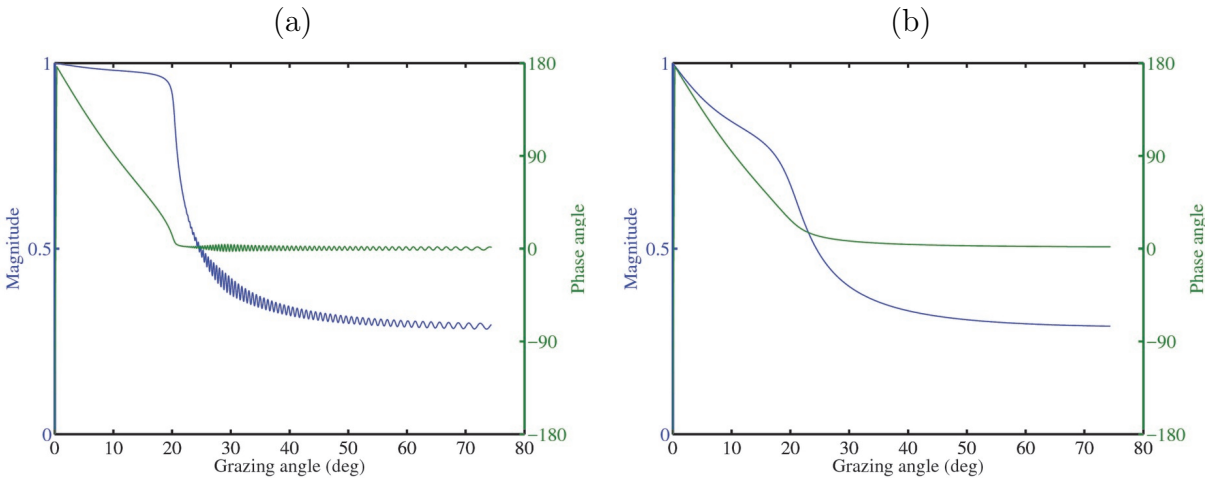

Figure 3.15: Reflection coefficients versus grazing angle for the minimum 0.10 dB/λ (a) and maximum 1.05 dB/λ (b) values in the range for the compressional attenuation parameter.

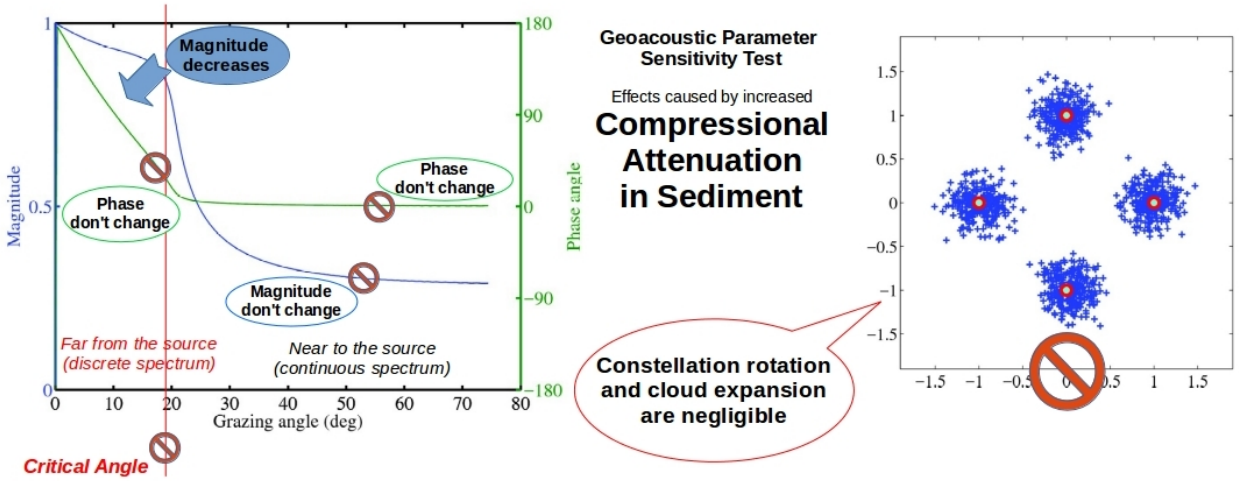

Figure 3.16: Compressional attenuation in sediment layer ($5m$) over bottom half space testing.

the same reason explained for ρ, *i.e.*, the critical angle is independent of α_p as shown in (3.9); (ii) the reflection coefficients magnitudes decrease for grazing angles smaller than the critical angle because the high reflectivity in this far field is decreased by the increasing of attenuation; (iii) the reflection coefficient phase do not change significantly; (iv) the CIR time spreading does not change significantly, only the path amplitudes (not shown); and (iii) the received PTR compensated constellation does not rotate because path delay shifts are negligible.

The variation of compressional attenuation in sediment layer have a low impact in the environmental focalization since the constellation do not change for all the range of compressional attenuation tested. This fact suggests that the selection of a search space for environmental focalization may consider the compressional attenuation parameter with a low resolution, or even may assume it negligible to the time-reversal communications system, which implies to exclude it from the search space of environmental focalization, thus saving computational cost without significant loss of communications performance.

3.3.4 Summary of individual parameter variability effects

Beyond the sediment layer parameters, the half-space bottom parameters were also tested (not shown), but the results indicate that the effects on the time-reversal receiver output bellow a $5m$ sediment layer are negligible. This can be explained by the fact that high attenuation occurs in the seabed for high frequency signals and there is no significant interaction with the region deeper than the sediment layer.

Table 3.6 summarizes the effect of a 5 m thickness clay sediment layer over medium sand bottom half-space. The geoacoustic parameters are on the left, where c_p denotes compressional sound speed, ρ denotes density, α_p denotes compressional attenuation, the under-script 1 denotes sediment layer and the under-script 2 denotes bottom half-space. The legend on the right shows the trend or general behavior of the reflection coefficient, the received constellation after being processed by the standard PTR and the critical angle.

These results indicate that, from an environmental focalization viewpoint, the relevance of the parameters for a time-reversal underwater acoustic communications system with the underwater scenario of the present test are classified in ascending order as follows:

Table 3.6: Test for thin sediment layer over half space bottom parameters.

Criterion / Geoacoustic Parameter	Reflection Coefficient		Reflection Coefficient		Received Constellation	Critical Angle
	MAG.	PHASE	MAG.	PHASE		
c_{p1}	↑	↑	↑	↑	↻	↑
α_{p1}	↓	↑	↓	×	×	×
ρ_1	↑	~	↑	↓	↻	×
c_{p2}	×	~	×	×	×	↓
α_{p2}	×	~	×	~	×	×
ρ_2	×	~	×	×	×	×

Legend

- ↑ Increasing
- ↓ Decreasing
- ↺ Counterclockwise rotation
- ↻ Clockwise rotation
- × No changing
- ~ Oscilating

compressional sound speed in sediment, density in sediment, compressional attenuation in sediment, compressional sound speed in bottom-half-space (if the thickness is < 2 m). The influence of density and compressional attenuation bottom-half-space are negligible.

Compressional speed is the more important geoacoustic parameter for the EPTR because its variation influences the CIR arrival path delay, which is an important feature to be set on the replica candidates of the environmental focalizer search space. This feature makes the search space generate CIR candidates with slight shifts of delay paths, which helps the processor to scan path delays positions in order to seek a better match between a CIR candidate and the estimated CIR.

The density in the sediment causes some constellation rotation, but the effect is relatively small, indicating a smaller degree of importance for the time-reversal system. Further, the compressional attenuation causes negligible effects in the constellation, being thus the least important of the geoacoustic parameters analyzed in the present simulation tests.

3.3.5 Joint geoacoustic parameters mismatch test

Geoacoustic parameters are not independent in the sense that when one parameter varies in a given direction the others vary accordingly. For instance, if the compressional speed increases then, in general, the density also increases and the attenuation may decrease. The present simulations aim at identifying the effect of creating a geoacoustic parameter mismatched channel and applying a standard time-reversal system. The approach is to use a particular type of bottom (sand) to be the "actual" channel and then use a channel replica generated from other types of bottom to be the channel estimate for the time-reversal filters. The objective is to observe the effects of a realistic bottom type variation over the constellation, caused by a controlled mismatch. It is important to note that the idea is not to track a new bottom along the transmission. The goal is to understand what are the consequences of using a wrong model to build a channel replica equalizing the channel with time-reversal technique.

Bottom types are chosen according to the parameters for typical materials found in realistic seabed shown in Table 3.2, *i.e.*, clay, silt, sand, gravel, moraine, chalk, limestone and basalt. To illustrate the wide range of reflectivity conditions encountered for such types of bottom, the reflection coefficients are computed. Figure 3.17 shows the reflection coefficient versus grazing angle computed for all those bottom types. Figure 3.18 shows the CIR corresponding to each type of bottom. Figure 3.19 shows the corresponding PTR output constellations obtained after the received signal that crossed through a sand bottom modeled channel be processed by PTR using CIR estimates modeled from each type of bottom in Table 3.2. These figures serve to illustrate the wide range of general reflectivity conditions

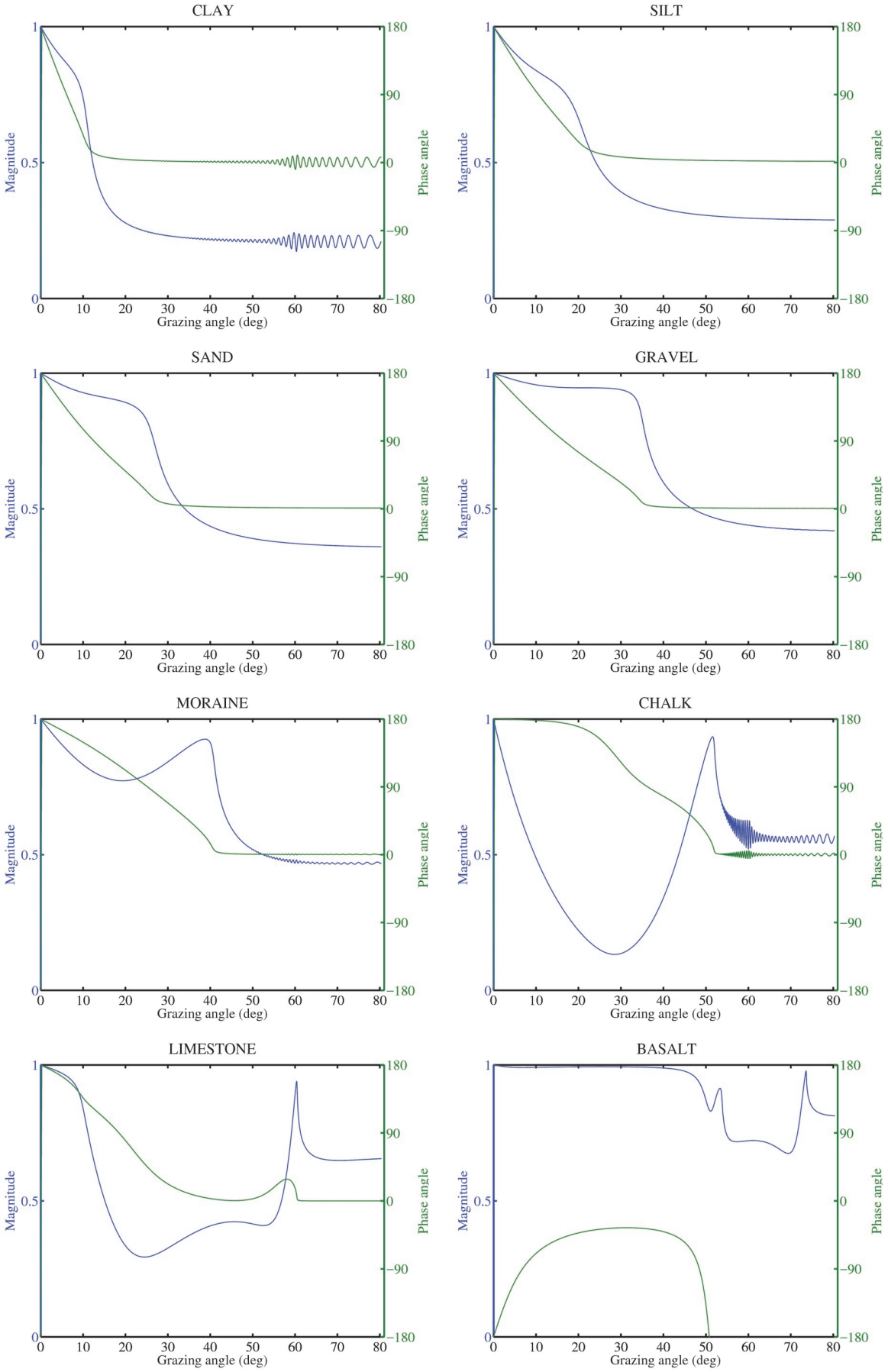

Figure 3.17: Reflection coefficient for bottom types: clay, silt, sand, gravel, moraine, chalk, limestone and basalt, with properties set according to Table 3.2.

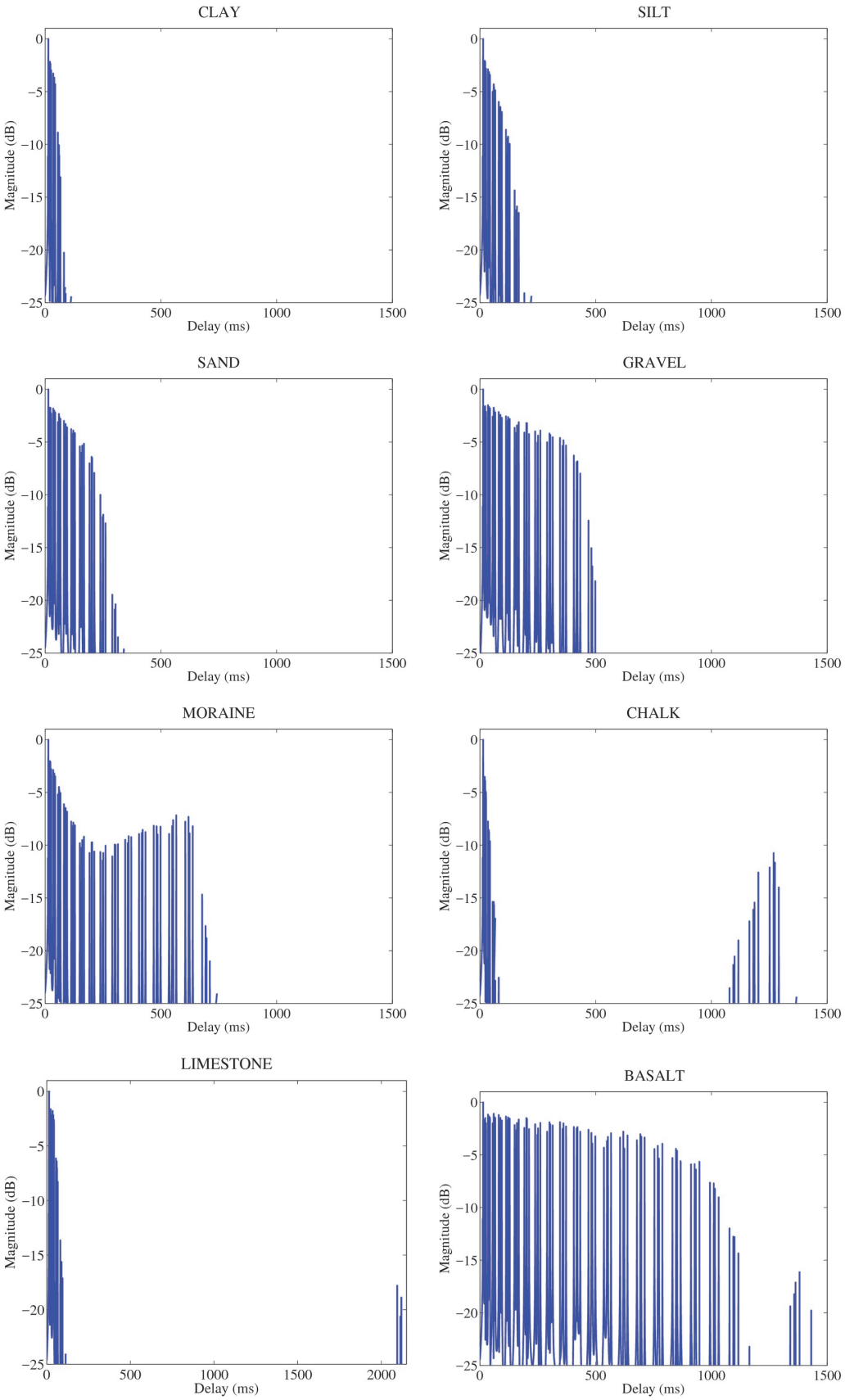

Figure 3.18: CIR generated assuming reflection coefficients of Fig. 3.17 for the scenario described in Sec. 3.2 and for bottom types: clay, silt, sand, gravel, moraine, chalk, limestone and basalt, with properties set according to Table 3.2.

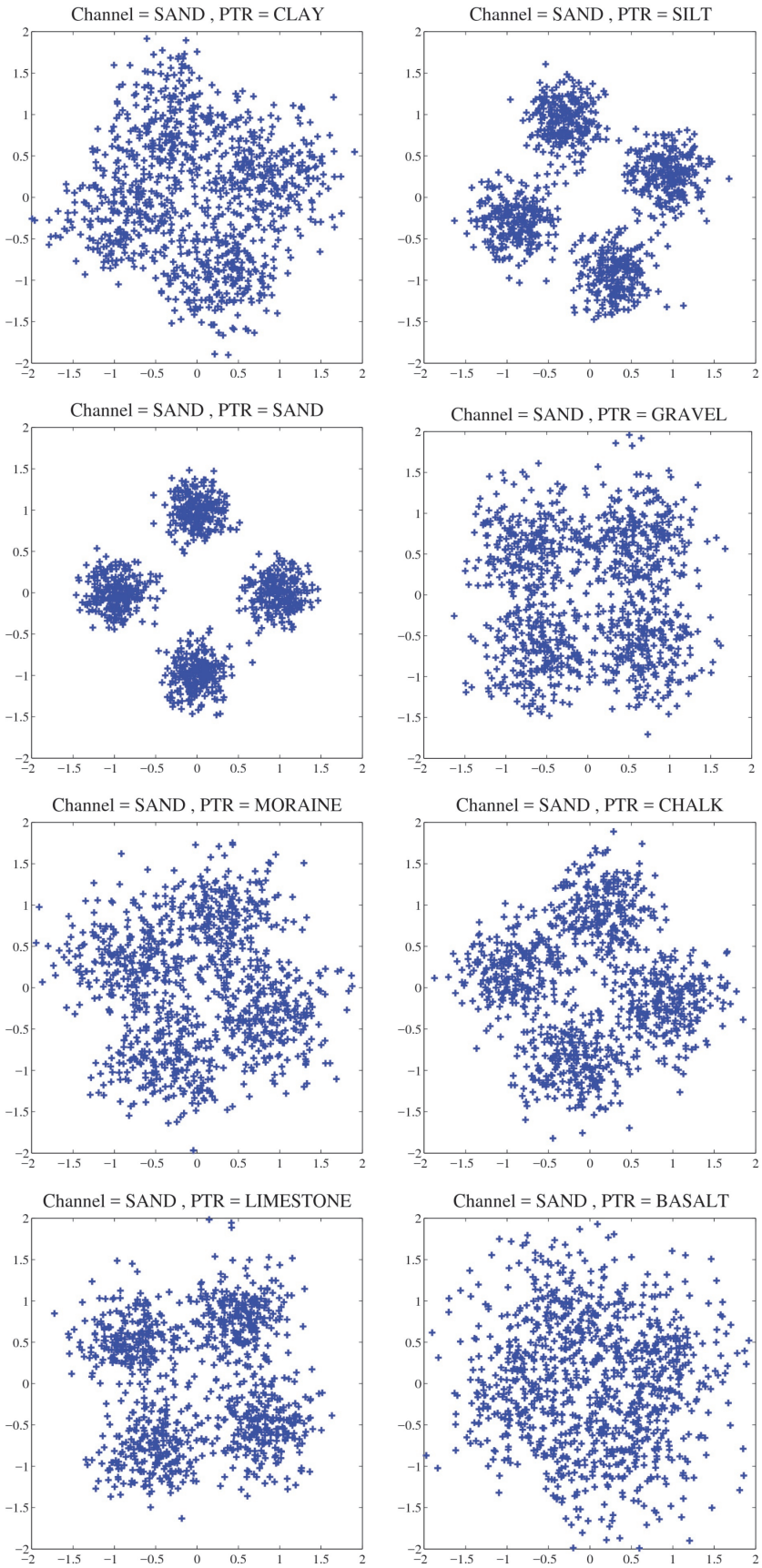

Figure 3.19: Receiver constellations computed in a noiseless channel assuming the mismatch between the reference "actual" CIR from sand bottom and each CIR "estimate" of Fig. 3.18 from the reflection coefficients of Fig. 3.17 for bottom types: clay, silt, sand, gravel, moraine, chalk, limestone and basalt, with properties set according to Table 3.2.

encountered for realistic bottoms. In the reflection coefficients figure, the low-angle reflection coefficients have small variation for bottoms with high reflectivity such as basalt, gravel and sand. For bottoms with poor reflectivity such as clay and chalk, the low-angle reflection coefficients show a severe decay.

In the CIR figures, the effects of the geoacoustic parameters variability in group over the amplitudes, delays of arrival paths and CIR time spread are presented, indicating quite different behavior in terms of CIR shape and time spreading for each type of bottom. In general, harder bottoms, *i.e.*, those with high density and compressional speed, tend to have a CIR with large time spread, which is explained by the increase in reflectivity. Such general behavior is observed in the CIR figures shown for all bottom types, except for chalk and limestone, which have the particular behavior of generating two short time-spread groups of path arrivals separated by a long time interval without paths. The reason for separation of path arrivals in two time-spread groups may be explained as being a consequence of the two separated high magnitude peaks of reflection coefficient (see Fig. 3.17) occurring the first at grazing angles ∼0-10 degrees and the second at grazing angles ∼50-60 degrees, with severe attenuation for the other grazing angles. These peaks of reflection coefficient magnitude are formed as result of the process given by (3.4) to compute a bottom loss model for a layered seabed, as described in subsection 3.1.3.

The most important results of this test are given in terms of received time-reversed constellations, since it is indicated how each mismatch in the CIR estimate affect the time-reversal performance. Figure 3.19 shows receiver constellations computed assuming the mismatch between the reference "actual" CIR from sand bottom and each CIR "estimate" of Fig. 3.18 from the reflection coefficients of Fig. 3.17 for bottom types: clay, silt, sand,

gravel, moraine, chalk, limestone and basalt, with properties set according to Table 3.2.

The sand-sand case shows the constellation diagram with dense clouds and no rotation, as expected, since this is the mismatch free case. One may note that even with an ideal matching between the "actual" CIR and the "estimated" CIR (since both are generated from sand bottom), there is some cluster variance. This effect may be explained by the existence of residual ISI caused by multipath in the PTR Q-function (see 2.15) due to poor spatial resolution of the array. A 14-hydrophones vertical line array spanning from 20 to 59 m depth, equally spaced of 3 m, are used in these simulations, as previously described in Sec. 3.2. Note that the PTR simulations were done for noiseless channels aiming to make it clear the possible trends in the results.

The constellation result for the sand-silt case (*i.e.*, the actual CIR is generated with sand bottom and the estimated CIR is generated with a silt bottom) present similar features than the sand-sand case, except for a slight cluster expansion and very low rotation. This fact may be explained by the sand bottom and the silt bottom have similar reflectivity conditions and the CIR in this simulation has a good match. This fact is interesting for the use of environmental focalization because if the optimization use the parameters of silt bottom instead of sand bottom, or the opposite, then it is expected not occur severe CIR mismatch in the PTR filtering, thus having low influence in the PTR output.

The constellation results for the other types of bottom show a severe cluster expansion and significant cluster rotation. The worse results in what regards constellation expansion are obtained with basalt and clay, indicating that they have strong differences relative to the sand bottom.

These tests of PTR sensitivity to geoacoustic parameters were done for the particular shallow water scenario described previously in Sec. 3.2 (*i.e.*, 3 km source-receiver range, 84 m water depth, source at 40 m, 14 hydrophones spanning from 20 to 59 m, 3m equally spaced, and 12 kHz carrier frequency) generating results that suggest the points discussed above, that are an useful knowledge for environmental focalization in time-reversal communications. However, to reach more consistent conclusions it is suggested to perform other simulations in different waveguide scenarios and frequency bands to check if the trends observed above test are still verified from a general viewpoint.

3.4 PTR sensitivity to geometric parameters

Geometric parameters, as source and receiver positions, are expected to cause severe influence in the underwater acoustic field, because the different positions can have particular multipath structure and, mainly, the relative source-receiver movement causes Doppler effect that must be compensated in coherent communications, otherwise the demodulation is severely affected by frequency shift and phase rotation. A test of geometric parameter sensitivity can be found for low frequency in [69], in a context of checking sensitivity of objective functions in MFP to the parameters variability, obtaining results that suggest a higher sensitivity to source-receiver range and receiver depth than to other parameters. In [70], physical modelling is used in a high frequency band, from 2 to 10 kHz, to test the transmission loss sensitivity to geometric parameters. It used Monte Carlo simulations to vary geometric parameters, according to a uniform distribution law within plus or minus 10 percent from the initial value in a range-independent environment, yielding results that suggested the geometric parameters to have a significant influence on transmission loss.

This section presents a geometric parameter sensitivity test in the context of underwater communications, generating results in terms of CIR and time-reversed demodulated symbols. First some considerations on multipath structure changes due to varying the source-receiver range are given. Then, a test is proposed in Sec. 3.4.1 to vary the source-receiver range during the transmission time, assuming a particular source horizontal velocity in a time variable acoustic propagation model, and thus the Doppler Spreading Function (DSF) and the constellation diagram of a standard time-reversal receiver output are checked.

At first glance, a Doppler effect on the received signal is obviously expected to be observed, since movement is imposed to the source. But the degree of distortion caused by particular values of source velocity over a QPSK constellation output of a time-reversal receiver in a shallow water scenario is unknown, and it can be observed in the results, reaching some sensibility in terms of constellation rotation.

One may note that the expected Doppler effect is not simply over a direct path. The waveguide scenario brings an additional complexity to the Doppler distortion of received signals because there are also boundary reflected paths, subject to a particular distortion on each path according to a corresponding Doppler compression or dilation factor. Such factor is appropriately described in the simplified scenario named bi-scattering geometry model [65], which present the propagation from a transmitter to a receiver through an indirect path reflected in a scatter point. A brief description of the path Doppler effect in a waveguide is presented in Appendix D.

An issue that may occur due to varying the source-receive range is the modification of the multipath structure such that a new eigenray path may arise. To illustrate this issue Fig. 3.20 shows an example of the path structure changing in a simplified waveguide, where the

Bellhop ray trace model [46] simulates few eigenrays for a source-receiver range of 190m and 193m. The hypothetic waveguide is a range-independent transect with 70 m water depth, isovelocity sound speed profile (1500 m/s), 20 m source depth and 50m receiver depth. The launching rays is limited to 10 degrees in both cases for the sake of clarity of the eigenrays figure.

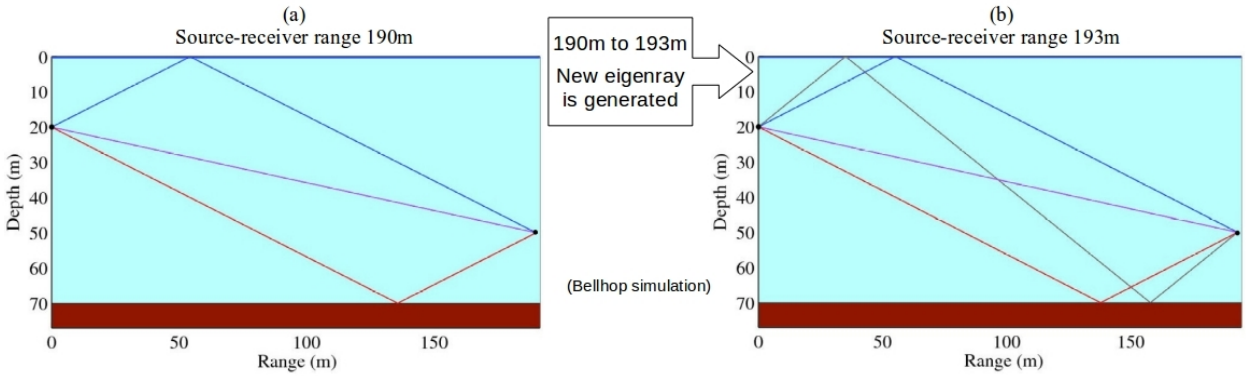

Figure 3.20: Example of the path structure changing in a simplified waveguide. Bellhop model eigenrays simulation (launching rays limited to 10 degrees) for source-receiver range of 190 m (a) and 193 m (b). Range-independent transect with 70 m water depth, 1500 m/s isovelocity sound speed profile, 20 m source depth and 50m receiver depth.

On the left are the modeled eigenrays for the 190 m source-receiver range and on the right are the modeled eigenrays in the same conditions except for the source-receiver range of 193 m. The normalized channel impulse responses corresponding to the multipath scenario of Fig. 3.20 (a) and (b) are shown in Fig. 3.21 (a) and (b), respectively.

The comparison of the tho cases clearly indicate that there is a new significant path in Figures 3.20 (b) and 3.21 (b), for source-receiver range 193 m, that is not in Figures 3.20 (a) and 3.21 (a), for source-receiver range 190 m, showing thus a change in the multipath structure, which is confirmed by the corresponding CIR of Fig. 3.21 (a) and (b). Nonetheless, this effect is not continuous in the sense that a small change in source-receiver range not necessarily generates the waveguide conditions to emerge a new eigenray. In some cases, the

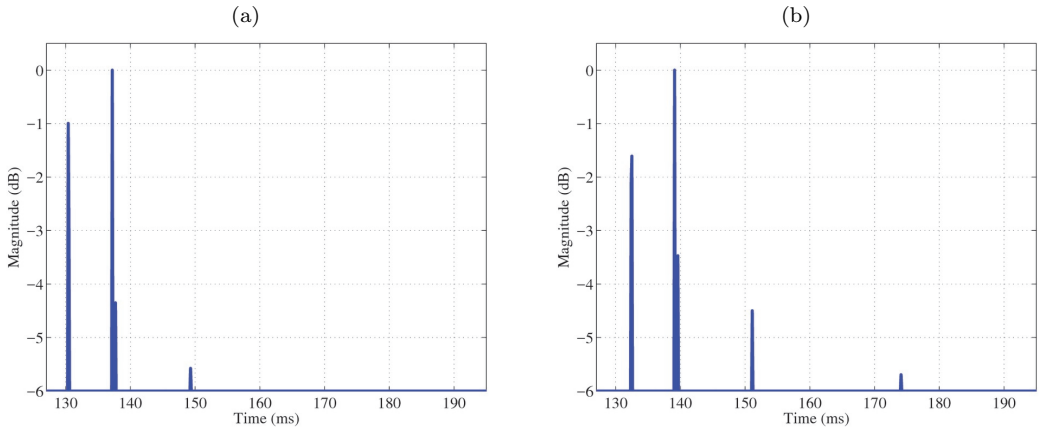

Figure 3.21: Normalized CIR modeled for source-receiver range of 190 m (a) and 193 m (b), with the parameters used in the multipath scenario shown in Fig. 3.20.

number of eigenrays remains the same and only their positions change slightly.

3.4.1 Sensitivity to the source horizontal velocity

The ray trace model is adopted for modelling time-invariant snapshot CIR. But when in presence of a variation of position during the transmission period a time-variant system is required. The Time Variable Acoustic Propagation Model (TVAPM) [71] is used to compute the time-variant channel. The Time Variable Acoustic Propagation Model (TVAPM) aims at simulating underwater acoustic propagation in time-variant channels, using sequential runs of the Bellhop model and time-variant filtering [60, 59]. Required inputs to dynamic propagation simulations with TVAPM are: a transmit signal is specified as input; linear velocities can be attributed to both source and array and the corresponding positions are updated progressively along transmissions.

The time-reversal filter for each channel in this simulation is the CIR in the initial state (initial CIR snapshot). Thus, it is possible to observe the effects of the constant variation of the source position (*i.e.*, constant velocity) along the transmission over the time-reversal

output constellation.

Figure 3.22 on first column (a,c,e,g and i) shows the Doppler Spreading Function and on second column (b,d,f,h and j) the PTR output constellation diagram for a moving source with velocities 0.0 m/s (a,b), 0.3 m/s (c,d), 0.6 m/s (e,f), 0.9 m/s (g,h) and 1.2 m/s (g,h) in the waveguide scenario described in Sec. 3.2.

The DSF figures on the left column indicate a Doppler frequency shift increasing trend, as expected, corresponding to each particular increase of source speed, where the vertical axis denotes the frequency-shift in Hz and the horizontal axis denotes time in ms. The constellation of the received signals, simulated with TVAPM, after being processed by a standard time-reversal processor are presented on the right column. These results clearly indicate that there are phase rotation distortion. These results are explained by the fact that the Doppler compression factor causes a resampling effect in the received signal, changing the phase of the QPSK symbols which thus causes a constellation rotation along the transmission time. In the frequency domain the compression factor causes frequency shift and spectrum distortion [65]. In coherent communications, which uses the signal phase to carry information of a data message, it is essential to compensate (or avoid) such type of distortion, otherwise the message recovery is severely degraded.

Also, one may note that small velocities as, *e.g.*, 0.6 m/s, are sufficient to severely distort the constellation of the received signal after being processed by PTR. Resampling techniques are often required to undo the compression or dilation distortion caused by the Doppler effect, employing short probe sequence to capture the compression factor and then resampling to compensate it in the received signal.

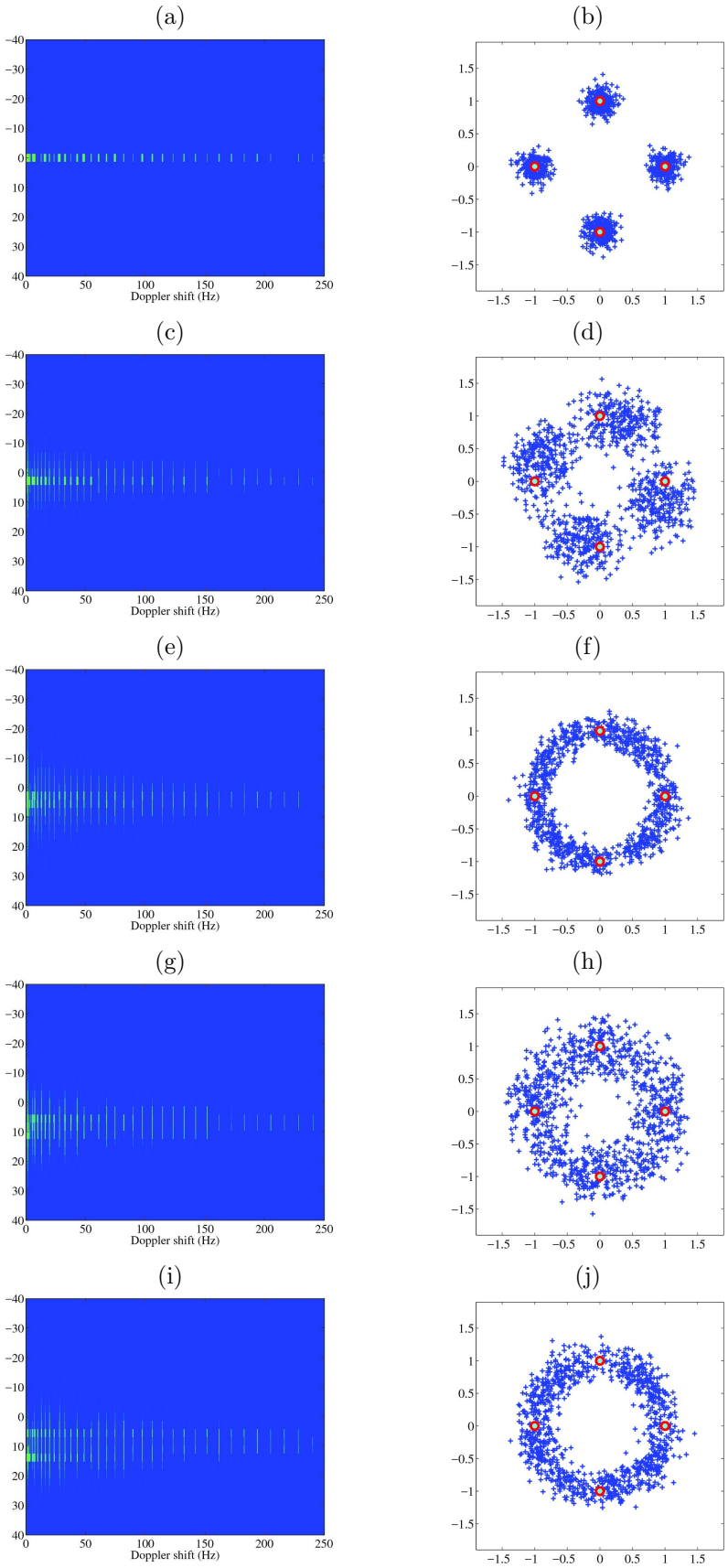

Figure 3.22: DSF (a,c,e,g and i) and PTR output constellation diagram (b,d,f,h and j) for a moving source with velocities 0.0 m/s (a,b), 0.3 m/s (c,d), 0.6 m/s (e,f), 0.9 m/s (g,h) and 1.2 m/s (g,h) in the waveguide scenario described in Sec. 3.2.

Figure 3.23 shows a short presentation of the more significant trends observed in results for source horizontal velocity, in terms of Doppler Spreading Function (DSF) (see equation 3.3) and received time-reversed constellation.

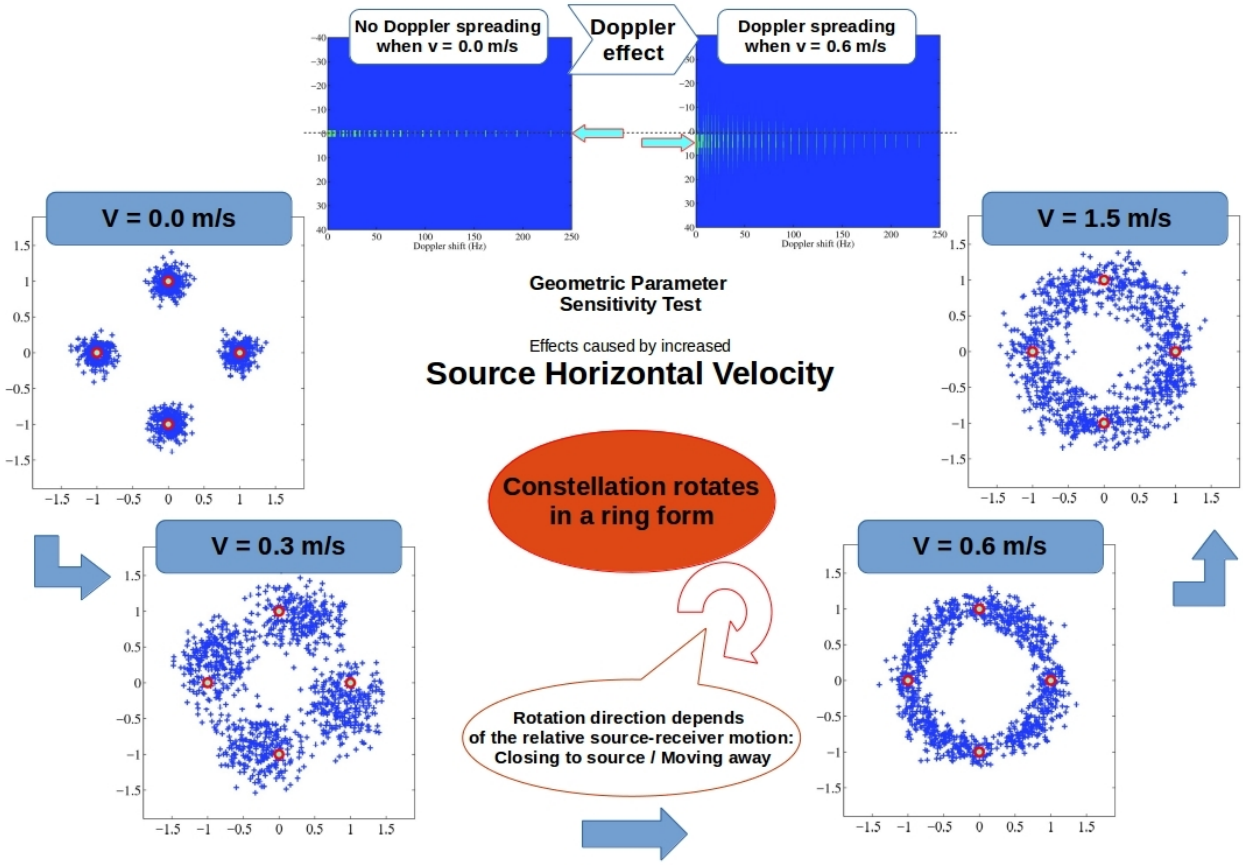

Figure 3.23: Trends observed in the results for source horizontal velocity sensitivity testing.

The constellation results show that for source velocity 0.0 m/s the signal recovery is successful, for velocity 0.3 m/s is sufficient CIR mismatch to generate small constellation rotation and a modest amount of errors and for velocities greater then 0.6 m/s severe distortion occurs, with the clusters tending to form a ring shape, precluding the correct demodulation of the received symbols.

3.5 Discussion

The concepts on waveguide acoustic propagation and simulations for parameters sensitivity presented in this chapter suggest that a set of physical parameters related to the environment and the geometry between source and receivers severely influence the behavior of acoustic propagation, affecting the CIR and consequently the received communication signals.

The knowledge obtained of the present sensitivity testing indicates that the geoacoustic parameters are important to shallow water communications, being the compressional sound speed in sediment layer the most important due to straightforward affecting the CIR path delays. An equalization processor may need to deal with the issue of finding the path delays that better represent the actual channel and use this information to design filters for compensating channel distortions. The other geoacoustic parameters still affect the propagation but, in general, have a less important role. The geometric parameter source-receiver range is fundamental for shallow water communications, since its variation along the transmission causes changes in the multipath structure and severe Doppler effect that must be mitigated, otherwise the communications performance may be significantly affected. Also, the sound speed profile (simulation not shown) is very important to shallow water communications since it determines the rays refractions along the water column. The understanding of such processes are used in the proposed EPTR (tested with real data in Chap. 5), namely by giving a higher resolution to the most important physical parameters for shallow water communications. In this context, an appropriate "a priori" search space in EPTR is chosen by selecting as input sets of physical parameters with better chance to generate realistic CIRs for a successful environmental focalization.

Chapter 4

Experimental results

Preview *This chapter presents experimental results of time-reversal communications based on channel identification with pulse compression, $\ell 1$-norm regularization and environmental focalization. The data sets were acquired between May 24 and May 27, 2011, during the UAN'11 experiment in the Strindfjorden, Trondheim (Norway). The results show that the proposed environmental-based time-reversal method, which employs physical modelling, outperforms the standard pulse-compressed time-reversal system for coherent underwater acoustic communications. Section 4.1 gives a brief description of the "Underwater Acoustic Network'11" sea trial; Section 4.2 compares results of the PC-PTR and PC-EPTR for two data sets collected on May 24 and on May 27; Section 4.3 introduces the Reg-L1 in the comparison tests; and Section 4.4 presents results of the PC-PTR, RegL1-PTR and PC-EPTR for a long term performance analysis of ten data sets covering a elapsed time of 250 s and containing five hundred thousand symbols.*

4.1 The "Underwater Acoustic Network'11" sea trial

The UAN11 experiment took place in the Strindfjorden, Trondheim (Norway) in May 2011. During this experiment a network composed of several nodes, including both mobile (AUV mounted) and fixed (moored) transmitters/receivers, was deployed and operated during the whole period. Every node of the network was equipped with modified Kongsberg cNODE Mini modems and one of the nodes included a receiving only vertical array with 16 channels - the Sub-surface Telemetry Unit (STU). Detailed characteristics of the environment and the signals transmitted during the seal trial are presented in [72] and briefly in the following

sections.

4.1.1 General aspects

The UAN11 experiment was part of the Underwater Acoustic Network project (UANp), whose objective was to conceive, develop and test at sea an innovative wireless network integrating submerged, terrestrial and aerial sensors for the protection of off-shore and coastline critical infrastructures.

The experiment should, among other goals, serve to determine the performance characteristics (*e.g.*, bandwidth, achievable bit rate, resilience/delay time) of digital transmission over acoustic underwater channels as a function of transmission frequency, signal modulation and environmental characteristics (including sound speed, bathymetry and channel geometry driven by source/receivers depth and range). Also, a high data rate point-to-multipoint communication link used to transfer sizeable data was considered in the project, part of which is the data analyzed in this thesis. See further objectives and details of the experiment in [72].

4.1.2 Environmental data

Bathymetry and source / receiver-array geometry

Figure 4.1 shows the bathymetry of the UAN11 sea trial in the eastern part of the Strindfjorden with the network nodes' positions superimposed. Various fixed nodes (FNO), the hydrophone array fiber optic connected to shore (STU), the pier and two mobile nodes (OBJ) are shown. This work considers the data obtained on the transect between source node FNO2 and the receiving multichannel array STU between May 24 and May 27.

The source is at 28 m depth and 890 m away from the STU, a vertical line array of

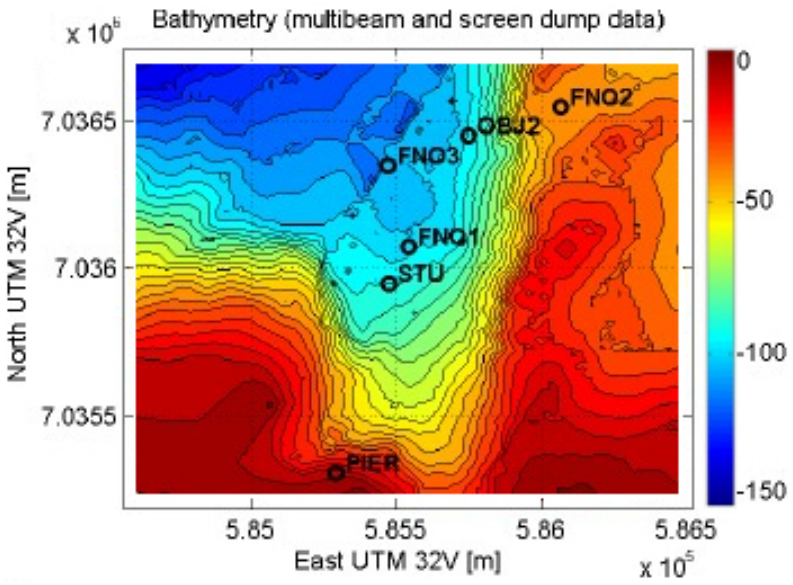

Figure 4.1: UAN'11 network node position superimposed on the bathymetry map of the area: FNO# denotes fixed nodes, STU is the Sub-surface Telemetry Unit multichannel array and OBJ# denote AUV mounted mobile nodes. The transect between FNO2 and the STU is 890 m long, and is range-dependent attaining a maximum depth of 100 meters.

16 hydrophones 4 m equally spaced, spanning from 14.1 to 74.1 m depth. Both the source and the receiving array are moored at the marked positions, therefore sensor movement is expected to be reduced. In addition, the tide variation at the experiment site is less than 2 m, considered small relative to the water depth of about 38 m at the source position and 98 m at the receiving array position.

Sound speed profiles for days May 24 and May 27, 2011

Several Conductivity Temperature Depth (CTD) casts were made during the UAN11 sea trial. The measurements made on May 24 and on May 27 with CTD#4 located near the STU are used in this work. The two Sound Speed Profiles (SSP), are shown in Fig. 4.2. The figure shows upward refracting profiles bellow ∼40 m, downward refracting profiles above ∼40 m and an initial formation of a mixed layer above ∼20 m on May 27, that was not present on May 24.

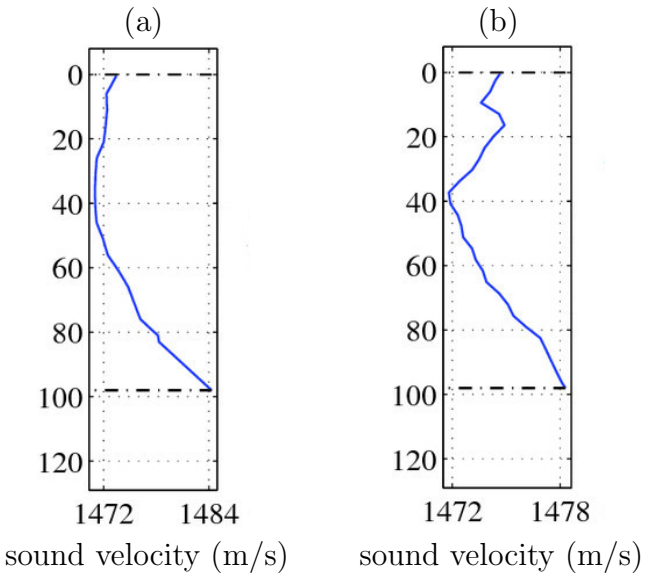

Figure 4.2: Sound velocity profiles measured with CTD#4 near the STU location on May 24 (a) and on May 27, 2011 (b).

Transect scenario and seabed geoacoustic properties

Figure 4.3 shows an idealized scenario of the FNO2 - STU 890 m transmit-receiver leg during the UAN11 sea trial, based on bathymetry information and on historical data for the seabed parameters.

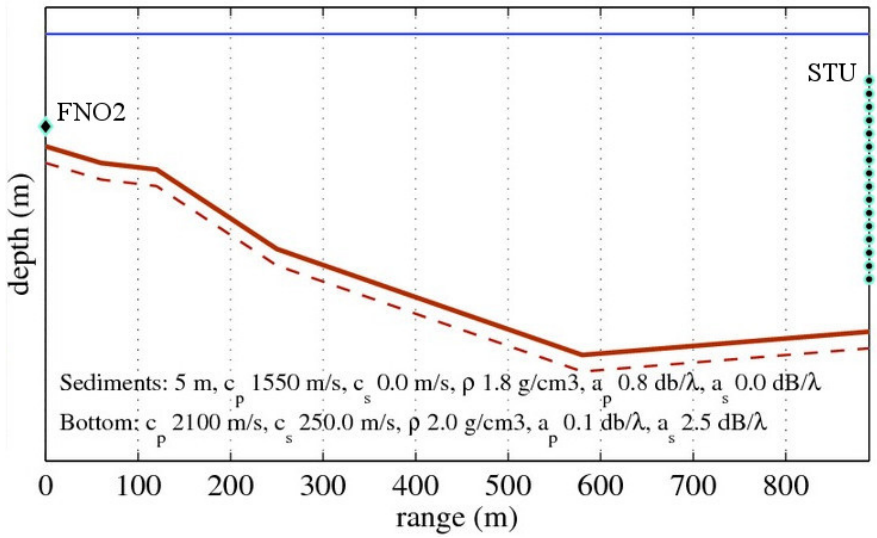

Figure 4.3: FNO2 - STU transmit-receiver leg during the UAN11 sea trial: range-dependent transect ($890m$), source depth $28.2m$, 16 hydrophones VLA $4m$ equally spaced from $14.1m$ to $74.1m$, $5m$ fluid sediments layer with c_{p1} 1550 m/s, ρ_1 1.8 g/cm^3 and α_{p1} 0.8 dB/λ, over viscoelastic bottom half-space with c_{p2} 1550 m/s, c_{s2} 250 m/s, ρ_2 2.0 g/cm^3, α_{p2} 0.1 dB/λ and α_{s2} 2.5 dB/λ.

The transect is strongly range-dependent with water depth varying between 38 and 98 m. The bottom parameters were derived from historical information of the area: a "rock bottom covered by mud or clay", using the Hamilton relations [45] and also using the information in [72]. The adopted environmental model is composed of a 5 m thick sediment layer over a bottom half space. The typical seabed parameters are shown in Fig. 4.7 and are described in Table 4.1.2. These values are used as reference for determining the search space for environmental focalization.

Table 4.1: Typical geoacoustic parameters in UAN11 area.

	Geoacoustic parameters		
Layer	Sound speed (m/s)	Attenuation (dB/λ)	Density (g/cm^3)
Sediment layer	1550	0.8	1.8
Bottom half-space	2100	0.1	2.0

4.1.3 Equipment

The data set used in this work were transmitted by the Fixed Node 2 (FNO2) and received on a Vertical Line Array (VLA) of sensors connected to a moored telemetry system (the STU), forming a single-input-multiple-output acoustic transmission.

The Sub-surface Telemetry Unity (STU) was used in the UAN11 experiment to acquire multiple received signals via the VLA [73]. It was positioned at location 63.4417°N and 10.7135°E, from where the received signals were then sent through a fiber optic cable to a shore laboratory. The STU is additionally equipped with a KM cNode modem and a 12 sensors thermistor chain. The STU recorded the QPSK modulated acoustic signals at sampling frequency 60 kHz, with synchronization pulses at the start-end of each frame of acoustic data set, as described in the next subsection.

The FNO2 containing the acoustic source was moored at location 63.4470°N and 10.7261°E. The Konsberg Maritime (KM) modem is the source considered in this work, being deployed at 28.2 m depth. The specifications of this modem is given as the cNODE-Mini modem transponder model 34-180 provided by Kongsberg Maritime (KM, Kongsberg, Norway), specifically adapted to tasks of the UAN'11 experiment [72]. This acoustic modem is described in detail in [74] and has a 180 beam pattern transducer at a center frequency of 25.6 kHz, with a bandwidth of 8 kHz and an emitted power between 173 and 190 dB re 1μPa@1m. Figure 4.4 shows on the left a picture of the KM modem used for single-input-multiple-output acoustic transmissions and on the right the scenario of one transmit-receive leg of the UAN11 sea trial where the KM modem was employed.

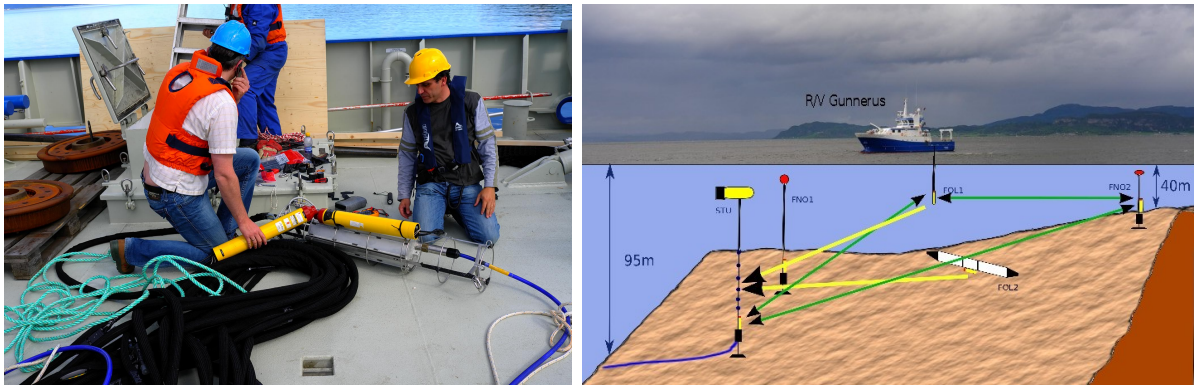

Figure 4.4: Modem Kongsberg cNode-Mini used for single-input-multiple-output acoustic transmissions (left) and a scenario of one transmit-receive leg of the UAN11 sea trial where the modem was used (right). The vertical line array with a yellow subsurface float is the STU and the source near the shore is the FNO2.

4.1.4 Acoustic data

Random sequences and images were transmitted with the KM modems, with symbol rate up to 4000 symb/sec using BPSK and QPSK digital modulation schemes at a carrier frequency of 26.5 kHz. Next, the data frame structure and the group of data sets processed in this work are described.

Data frame structure

During days May 24 and 27, the message data were the pixels of a gray image, converted into a bit stream QPSK modulated at a data rate of 4000 bit/s. The signals processed in this work follow a fixed frame containing a payload bit stream that corresponds to the converted pixels of a low resolution gray image. Figure 4.5 shows the transmitted image.

Figure 4.5: Image message used as payload for some of the signals transmitted during the UAN11 experiment. The QPSK modulation received signals at 4000 bit/s are processed in this work.

The data frame structure is shown in Table 4.2 and has a total size of 50000 symbols, thus containing 100000 bits.

Table 4.2: Frame structure of the transmitted data (size and generator polynomial of m-sequences).

Type	Preamble m-seq.	Header	M-seq.+Message slot	Postamble m-seq.
Nr. of symbols	511	40	20×(127 + 1873)	511
Gen. poly.	110011000	-	1000001	110001001

The structure of this data frame is organized (in order) as a preamble m-sequence with 511 symbols, an header with 40 symbols, a payload and postamble m-sequence with 511 symbols. Further, since the bit stream length is variable according to a particular message or set of image pixels and the frame size is fixed (50000 symbols), a constant stream of symbol 1 is positioned at the end of the payload with the length needed to complete the frame size. Fig. 4.6 shows the spectrogram of a signal received at the deepest STU array

hydrophone where the constant stream is seen as a tone at the carrier frequency after the payload end and before the final postamble, between seconds 20 and 25.

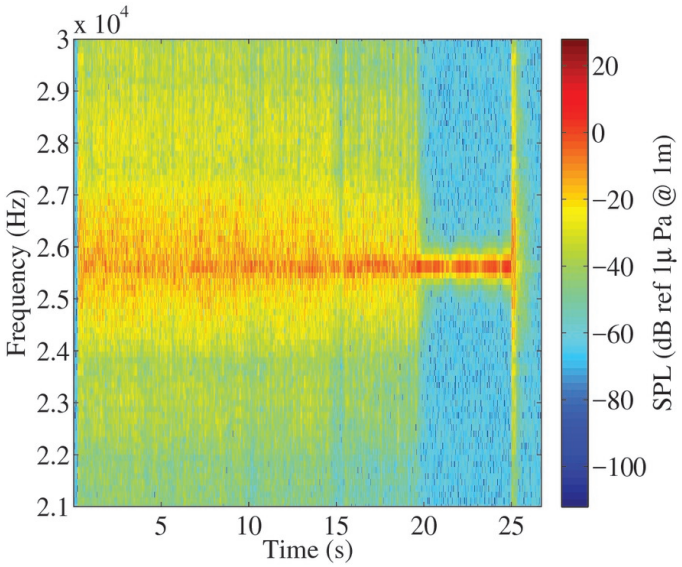

Figure 4.6: Spectrogram of a signal received at hydrophone 1 (deepest, at 74.1 m), with sound pressure level (SPL) in decibel referred to $1\mu Pa$ at $1m$. Carrier frequency 25.6 kHz. The constant stream of 1's is filling the data packet between seconds 20 and 25.

The preamble and postamble are used to perform time compression/dilation compensation, aiming at removing clock synchronization impairments between transmitter and receiver and a possible Doppler trend. The payload contains the bit-stream message corresponding to the image pixels and a sequence of 20 short m-sequences with 127 symbols each, which are inserted every second for channel tracking. In the following section , these short m-sequences will be used for CIR estimation through PC and environmental focalization, respectively. The final channel matched-filter for the time-reversal receiver is performed with the mean CIR over the 20 short m-sequence estimate, both for PC-PTR and EPTR.

Data set

The data set processed in this work are composed by ten QPSK frames collected in the UAN'11 sea trial. They form a reasonably large amount of data, totaling five hundred

thousand symbols (thus, 1 million binary digits) collected between May24 at 20h35m and May 28 at 00h05m. Each frame has sufficient size of payload to contain all the pixels of the gray image of Fig. 4.5.

Table 4.3 shows for each frame the identification number (left column), the transmission date (middle) and the transmission start time (right).

Table 4.3: Transmission start times of each UAN11 data frame processed in this work.

Frame ID number	**Date**	**Start time**
241	May24	20h35m59s
271	May27	22h52m03s
272	May27	22h55m30s
273	May27	23h06m02s
274	May27	23h08m25s
275	May27	23h20m02s
276	May27	23h27m02s
277	May27	23h45m44s
278	May27	23h54m05s
279	May27	23h59m45s

4.2 Experimental results I: comparison of PC-PTR with PC-EPTR

This section compares the results obtained with conventional PC-PTR and PC-EPTR on real data records acquired in two days of May 2011 during the UAN'11 experiment. The first data set was collected on May 24 with identification number 241 and the second was collected om May 27 with identification number 275. The choice of these data sets is justified by the the fact that they were collect in different days, thus with different sound speed profiles, and therefore to check the ability of the EF algorithm to perform in two different environmental settings.

The results will show that PC-EPTR clearly outperformed the conventional PC-PTR by an amount of 1 to 4 dB in mean-square error (MSE) and bit error rate (BER). The results also show that environmental model-based methods may be used with success on real data underwater communications.

4.2.1 Environmental focalization setup

The adopted environmental model is composed of a 5 m thick sediment layer over a bottom half space, which characteristic parameters are listed in column "Reference" of Table 4.4. This table also shows in the last two columns, the search interval and number of discretiza-

Table 4.4: Environmental physical parameters for propagation modeling and focalization

Physical parameter	**Unit**	**Reference**	**Search**	**Size**
Water column				
Source-receiver range	(m)	890	870 - 910	5
Source depth	(m)	28.1	26.50 - 29.50	5
Array depth	(m)	14.1	13.10 - 15.10	5
Sound speed profile	(m/s)		(see Fig. 4.2)	
Sediment				
Thickness	(m)	5	-	-
Comp. speed c_{p1}	(m/s)	1550	1480 - 1620	10
Comp. attenuation α_{p1}	(dB/λ)	0.8	0.60 - 1.00	2
Density ρ_1	(g/cm^3)	1.8	1.30 - 2.30	2
Bottom				
Comp. speed c_{p2}	(m/s)	2100	-	-
Shear speed c_{s2}	(m/s)	250	-	-
Comp. attenuation α_{p2}	(dB/λ)	0.1	-	-
Shear attenuation α_{s2}	(dB/λ)	2.5	-	-
Density ρ_2	(g/cm^3)	2	-	-

tion intervals, respectively, for those parameters included in the environmental focalization procedure discussed below.

The environmental focalization was performed with exhaustive search optimization based on the Bartlett processor for a search space with 5000 replicas. This size is obtained by the

product of all the discretization intervals in the last column of Table 4.4, *i.e.*, the search space size is given by $5^3 \times 10 \times 2^2 = 5000$, which represents the combination of all "a priori" parameter values. Note that the exponential nature of the search space size , with the number of parameters and their discretization, causes the very fast increase in the number of candidate replicas if an excessive number of discretization intervals are declared. Thus, a careful choice of the "a priori" parameters must be done aiming to generate an appropriate search space and avoid an exaggerated computational cost. An alternative procedure to reduce computation time, but that was not tested in this work and may be suggested for future work, is to use a global optimization technique, such as simulated annealing or genetic algorithms.

In order to obtain a glimpse of the possible propagation conditions for an acoustic transmission between FNO2 and the STU, Fig. 4.7 shows the Bounce/Bellhop model computed eigenrays between the source location and each of the vertical array receivers along the transect with the following path color coding: direct (magenta), surface reflected (blue), seabed reflected (red) and surface-bottom reflected (gray).

One can see that there are very few bottom-reflected rays (in red) reaching the hydrophones 6 to 9, in comparison to the surface-reflected rays (blue) that reach all hydrophones. This occurs due to a low slope bottom near the source followed by a high slope bottom, creating a shadow zone for bottom-reflected rays. For this reason, it is expected that the CIR will have a second arrival path with a higher frequency spread (due to free surface motion) than the first arrival path.

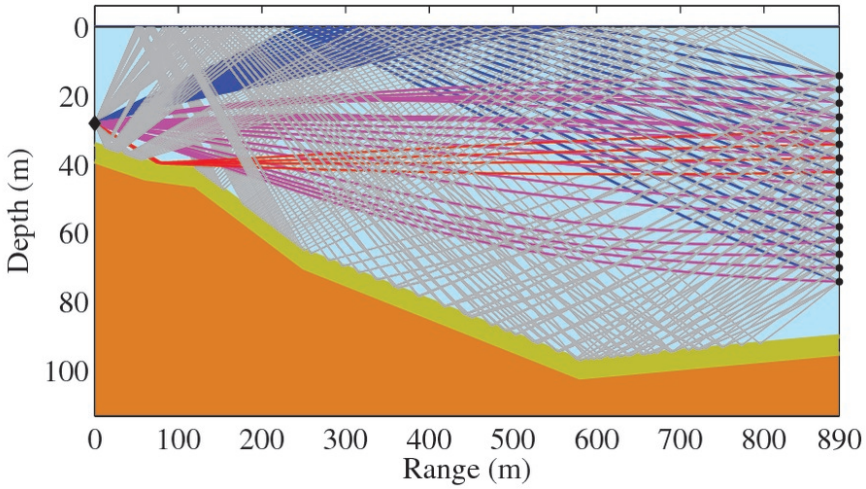

Figure 4.7: Scenario for the transmitter-receivers transect (FNO2-STU): range-dependent 890 m long transect, source depth 28.1 m, 16 hydrophones vertical array 4 m equally spaced from 14.1 m to 74.1 m depth, maximum water depth 100 m, 5 m sediment layer (in dark-yellow color) over bottom half-space (in orange color). The eigenrays are color coded as follows: direct paths in magenta, surface-reflected paths in blue, bottom-reflected paths in red, and surface-bottom-reflected paths in gray.

4.2.2 "A posteriori" physical parameters

The physical parameters that generate the CIR replicas that best match the PC estimated CIR are obtained as the output of the acoustic focalization algorithm after an exhaustive search over the parameter space defined in columns "Search" and "Size" of Table 4.4. The dimension of the search space which results from Table 4.4 is 5000. Although the focus of this work is not on environmental inversion, the obtained "a posteriori" physical parameters can be seen as a by product of the PC-EPTR communication system. The geometric parameters denote the physical parameters directly related to the source and receiver positions, *i.e.*, source-array range, source depth and the receiving array depth (using the shallowest hydrophone as reference).

Figure 4.8 shows for snapshots 1 to 20 the evolution of the combination of the geometrical physical parameters source-receiver range, source depth and array depth (using the shallowest

hydrophone as reference) that generated the three best CIR replicas for the data set #241 collected on May 24 (a) and the data set #275 collected on May 27 (b): the best fitness maximum "a posteriori" parameter estimates (dash blue-circle), the second best fitness parameters (dash red cross) and the third best fitness data (dash green cross). It can be seen that there is a reasonably good agreement between the three candidates for each geometric parameter, even though the data set #275 shows a higher variation than the data set #241. In addition to the parameters shown in Fig. 4.8, the geoacoustic parameters of the sediment layer shown in Table 4.4, are also used in the focalization process.

Figure 4.9 shows for snapshots 1 to 20 the evolution of the combination of the geoacoustic physical parameters sediment compressional sound speed, sediment density and sediment compressional attenuation that generated the three best CIR replicas for the data set #241 (a) and the data set #275 (b).

For the scope of this work that aims at generating an appropriate CIR for increasing the performance of time-reversal communications, the accuracy of the "a posteriori" parameters is a secondary issue. The most important issue is that the physical parameters in the search space should improve the adjustment between CIR replicas and observed CIR, during the objective function optimization, through environmental focalization.

Further, since there are physical parameters not inverted for, *i.e.*, parameters with fixed values along the optimization, it is expected to observe variability on the output inverted parameters that is not only due to their actual physical variability, but also due to the their ability to compensate those fixed parameters not considered for optimization. This procedure that divides the channel parameters in two component groups, one fixed and the other variable, is usual in matched-field inversion [75].

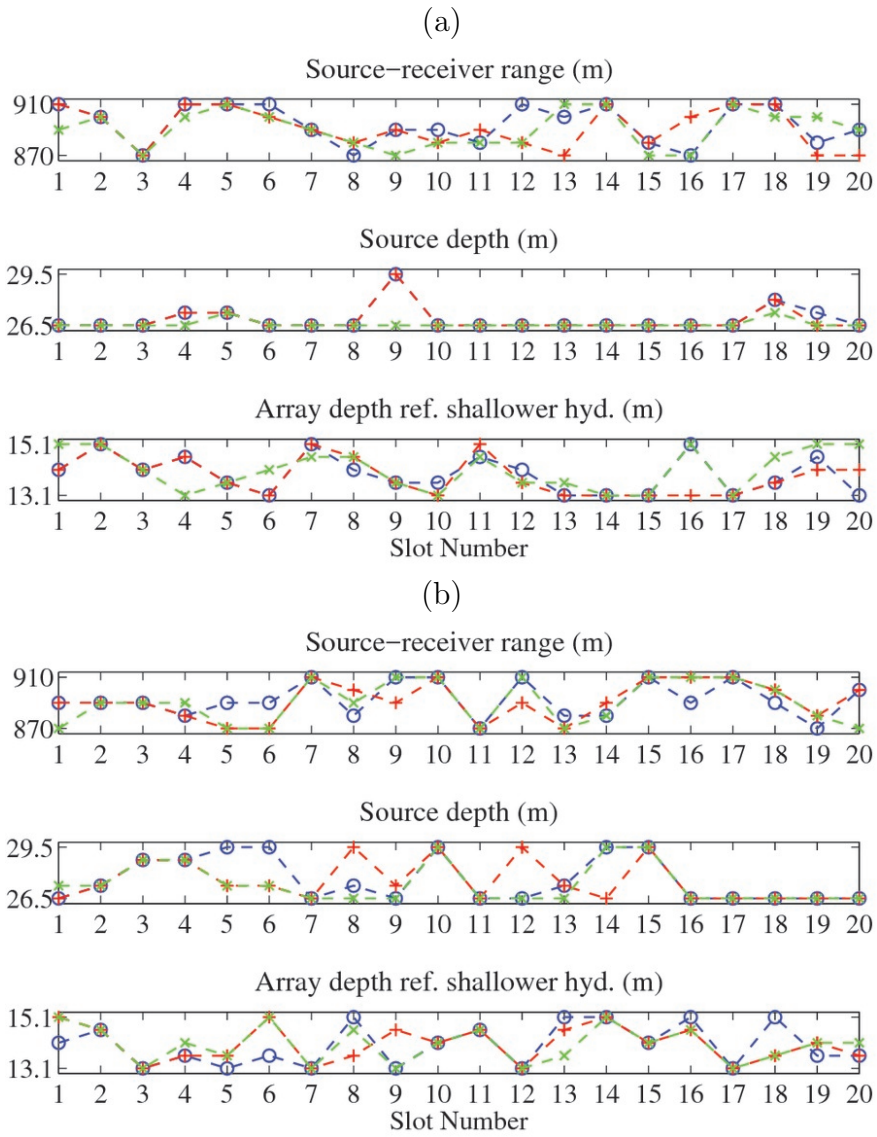

Figure 4.8: Maximum a posteriori geometric parameters source-receiver range, source depth and array depth (using the shallowest hydrophone as reference) obtained through environmental focalization for each slot of the data set #241 received on May 24 (a) and #275 received on May 27 (b). The three best fitness set of parameters are shown: maximum "a posteriori" set (blue circles), second maximum set (red cross) and third maximum set (green cross).

The compressional sound speed in the sediment repeatedly reaches the lower boundary of the search space along the time slots (not shown). At first, one is tempted to decrease the lower boundary of the search space, but since its value is 1480 m/s, already lower than the mean water sound speed, it was decided to maintain the search interval in order to avoid generating an excessively non-realistic environment.

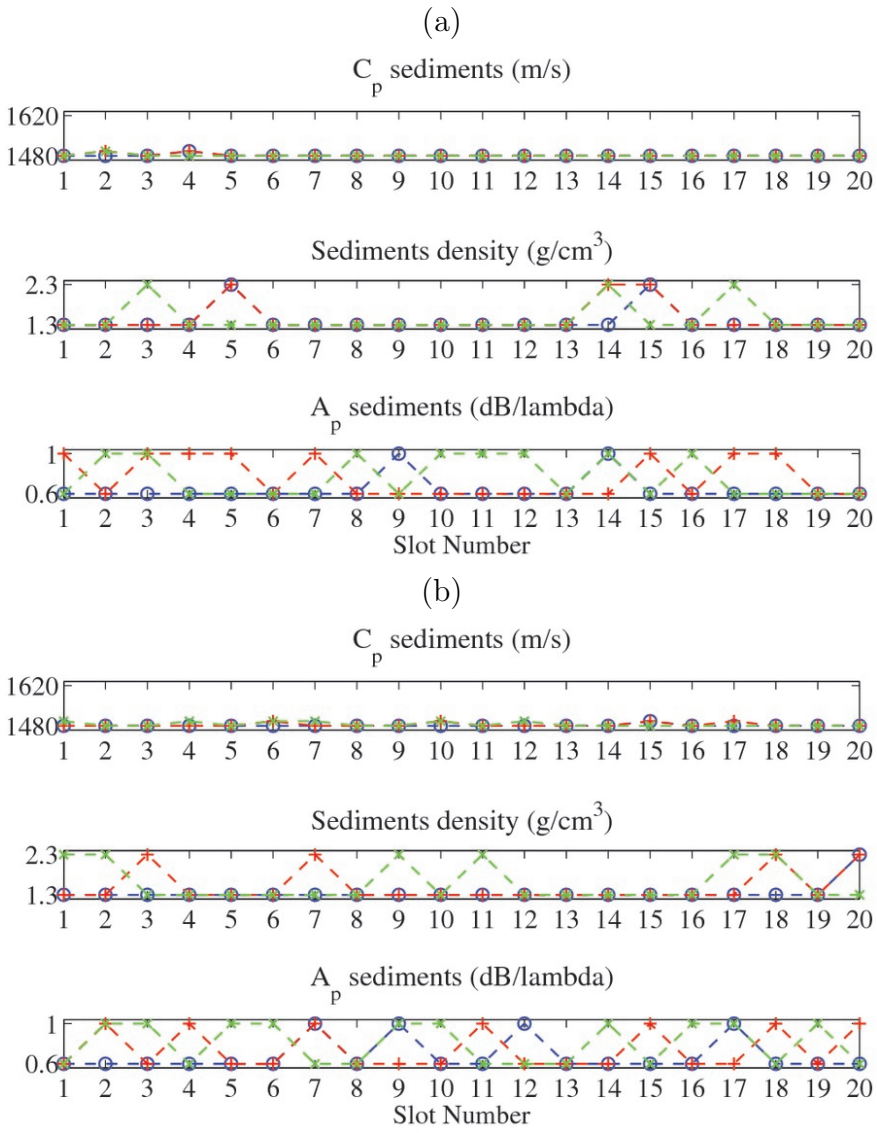

Figure 4.9: Maximum a posteriori geoacoustic parameters sediment compressional sound speed, sediment density and sediment compressional attenuation obtained through environmental focalization for each slot of the data set #241 received on May 24 (a) and #275 received on May 27 (b). The three best fitness set of parameters are shown: maximum "a posteriori" set (blue circles), second maximum set (red cross) and third maximum set (green cross).

The environmental focalization yields an equivalent environmental model [76, 44] as by product. The equivalent model consists in the employment of a set of acoustic propagation physical parameters to generate a environmental model that maximizes an objective function, not regarding if that parameter set in fact represents the actual environment. Therefore, some degree of compensation between particular "a priori" parameters may occurs in the

process to optimize the "a posteriori" parameter set that generate the output CIR of the environmental focalizer, which we use here for channel equalization.

In this work the bottom half-space parameters were not optimized for because it is expected that at this high-frequency regime (carrier frequency at 26.5 kHz) the propagating signals have very small interaction with that region, due to strong attenuation on the seabed and rays refraction occurring only in the sediment layer.

More controversial is that, also the SSP was not optimized for during the focalization process. Instead, the profiles taken nearby to the STU receiving array of Fig. 4.2 were used. However, the SSP is an important modeling parameter since it directly influences the refraction of the propagating rays in the water column and its time variability has a certain impact on the CIR. The reason for not including the SSP in the search space was twofold: one is that there was no sufficient ground truth information on previous SSP in the source-receiver transect location; and two it would substantially increase the search space and therefore the computational cost. The SSP difference between the two days makes data set #241 (May 24) a much benign channel than data set #275 (May 27), with a diagram constellation with low cluster variance and better performance, as it will be shown in the next subsection.

4.2.3 Analysis of time-variant CIR data

In this subsection we will analyze the time-variant CIR, whose estimate may be obtained by PC of the received signals using the transmitted probes or by environmental focalization based on noise-free physical modelling, after polyphase resampling for removing of an eventual Doppler trend.

Figure 4.10 shows the wavefronts estimated with PC (a) and modeled after environmental focalization (b) for the data set #241 (see Table 4.3), in a 16 ms time window. The PC and EF based on PC, described in detail in Chap. 2, are used to compute the wavefronts shown in Fig. 4.10 (a) and (b), respectively. The wavefronts show that the two first arrivals

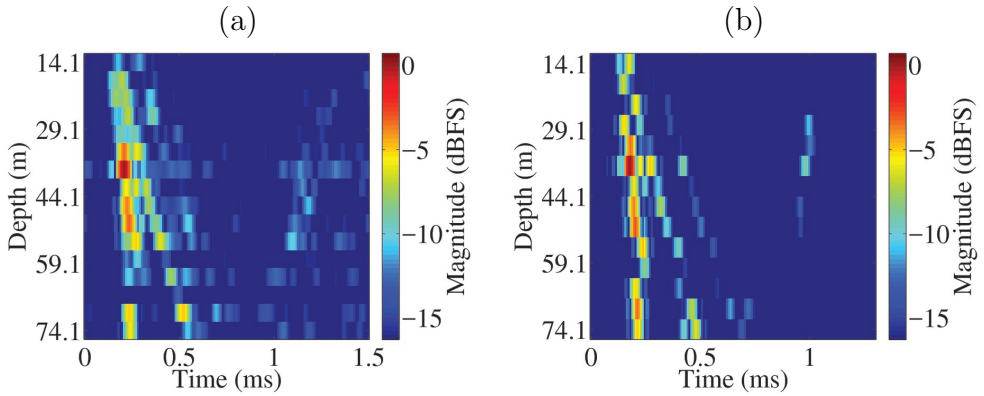

Figure 4.10: Wavefronts estimated by PC (a) and by EF based on PC (b) for data set #241 The colorbar shows magnitude in decibel referred to full scale (dBFS).

are clearly distinguished with a good match between data and model. The first wavefront has a maximum of energy at the minimum of the sound speed while the second wavefront is downward propagating. Clearly the wavefronts estimated with PC are noisy while those obtained with EF are noiseless and therefore much better defined.

Figure 4.11 shows, for the data collected on May 24 at the hydrophone 6 (54.1 m depth), the CIR estimated with PC in time-delay representation along the 20 seconds (a), the mean CIR estimated power (b), the CIR modeled by EF in time-delay representation (c) and the mean CIR modeled power obtained by EF (d). Comparing plots 4.11 (a) and (c), a good match is clearly visible between path arrival times and amplitudes. There is a considerable amount of noise , of about -10 dB, on the PC estimated CIR, which tends to obscure the secondary paths with smaller magnitude. As expected, comparing the first and second rows of Fig. 4.11, the noise reduction is clearly noted.

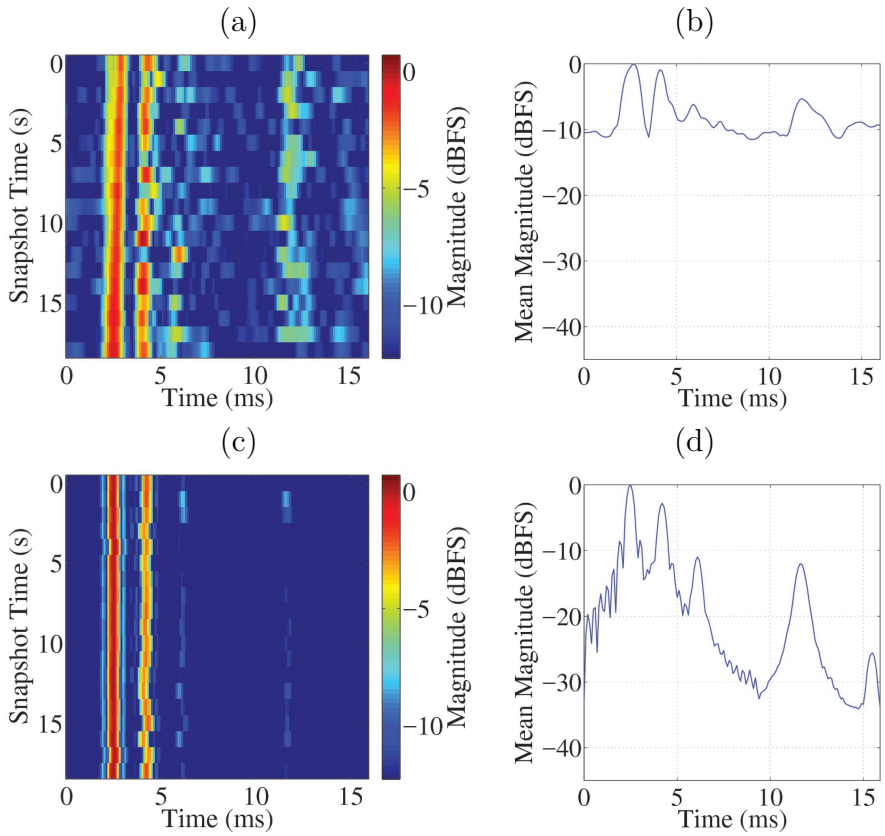

Figure 4.11: CIR for the data collected on May 24 for the data set #241 at hydrophone 6 (54.1 m depth) estimated by pulse compression (a) and (b) and modeled through environmental focalization (c) and (d). Time-delay CIR representation (a) and (c) and average magnitude CIR (b) and (d). The colorbar shows normalized magnitude in dBFS.

Figure 4.12 shows the same type of plots as Fig. 4.11 but for the data set #275 of May 27. Again in this case and despite the very different sound velocity profiles (see Fig. 4.2), the capture of the overall path arrival structure as well as the small scale variability is obtained in the modeled data of Fig. 4.12, plots (c) and (d), when compared to plots (a) and (b), respectively. Note, however, a discrepancy on the mean arrival time of the late path at around 14 ms delay when comparing plots (b) and (d). Despite the fact that EF generates noise-free CIR replicas to replace the noisy CIR estimates in the time-reversal processing, these replicas may have modelling errors that tend to appear in the weaker paths, as shown in Fig. 4.12 (b) and (d). Even so, if the EF succeeds, the modelling errors are sufficiently small and thus the communications performance is improved.

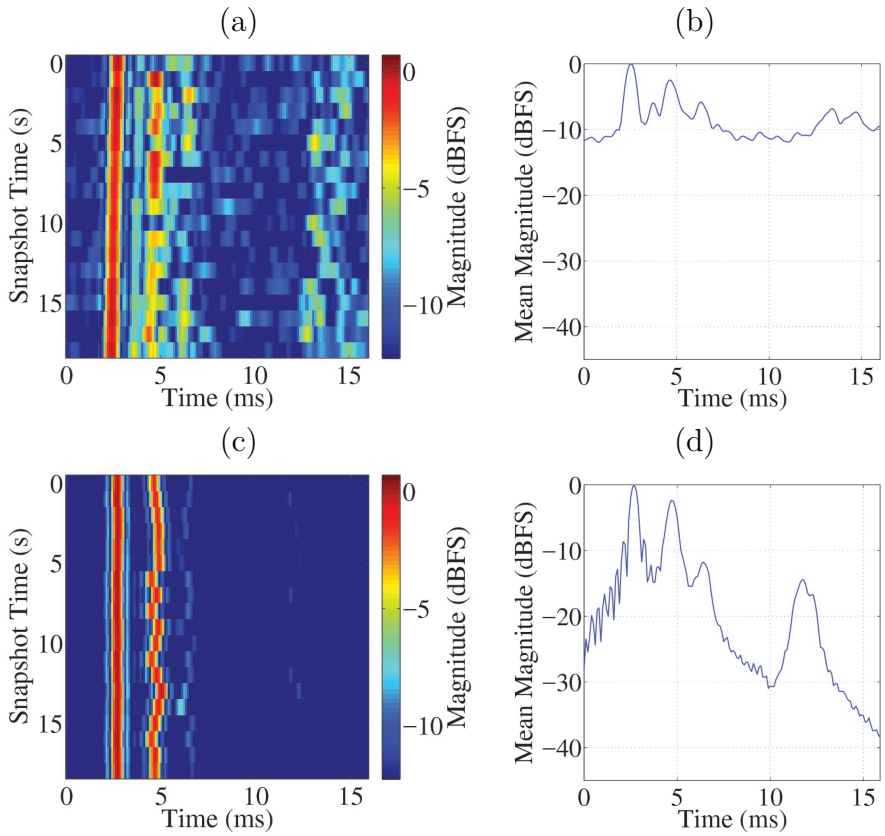

Figure 4.12: CIR for the data set #275 collected on May 27 at hydrophone 6 (54.1 m depth) estimated by pulse compression (a) and (b) and modeled through environmental focalization (c) and (d). Time-delay CIR representation (a) and (c) and average magnitude CIR (b) and (d). The colorbar shows normalized magnitude in dBFS.

Fig. 4.13 compares the baseband complex envelope estimated with PC with that obtained by environmental focalization for snapshot 4 of the data set #275, hydrophone 6. This

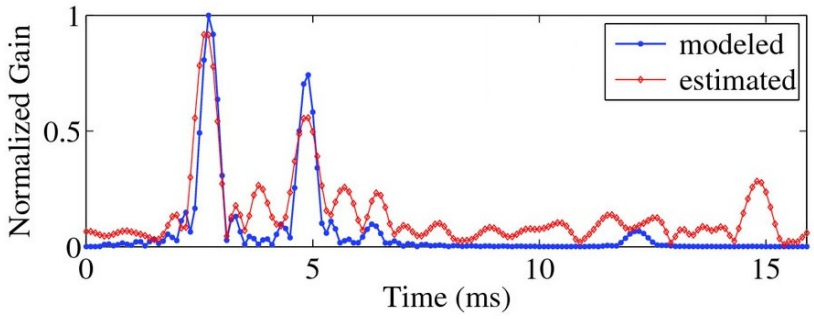

Figure 4.13: A CIR snapshot comparison: envelope of complex baseband equivalent CIR obtained by PC estimation (magenta) and by environmental focalization (blue), for hydrophone 6 of the data set #275, slot number 4.

comparison illustrates the much lower noise level on the "a posteriori" modeled CIR snapshot,

when compared to the corresponding pulse-compressed estimate and also the wrong estimate of the arrival time of the late path.

4.2.4 Communication performance analysis

In this subsection we will evaluate the performance of the communication system in recovering the transmitted message. This may be done in a variety of forms, one of which is by observing the received signal constellation diagram, as shown in Fig. 4.14 for the data set #241 processed with PC-PTR (a) and PC-EPTR (b) and for the data set #275 processed with PC-PTR (c) and PC-EPTR (d). It can be observed that the PC-EPTR constellations are better separated than the PC-PTR constellations. This assertion is striking for the data set #275, plots (c) and (d). This reduced cluster variance means a clear soft-decision improvement.

Another, possibly more objective, form for performance evaluation is through bit error rate (BER) and mean square error (MSE). Table 4.5 shows the values of MSE, BER and number of wrong symbols of these constellations over the whole data horizon, where it is observed that the PC-EPTR yields a considerable mean MSE gain of 0.93 dB and 3.67 dB over PC-PTR on May 24 and on May 27, respectively. Observing the constellations and

Table 4.5: Performance analysis of PC-PTR and EPTR.

May 24	**PC-PTR**	**EPTR**	**Gain** (dB)
MSE (dB)	-11.60	-12.53	0.93
BER	1.20×10^{-3}	3.64×10^{-4}	5.19
# **errors** (out of 71504)	86	26	
May 27			
MSE (dB)	-7.13	-10.80	3.67
BER	3.97×10^{-2}	2.92×10^{-3}	11.34
# **errors** (out of 71504)	2842	209	

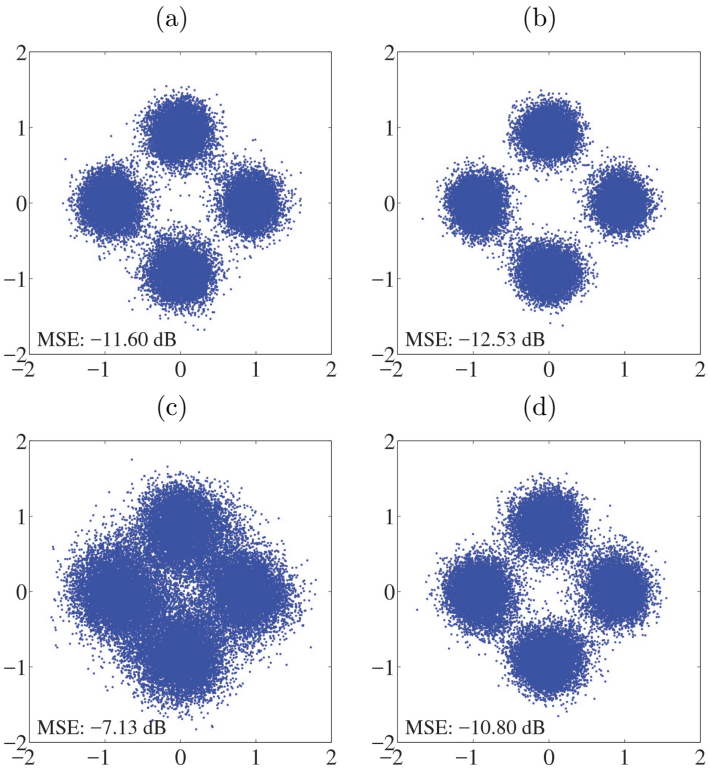

Figure 4.14: Constellation of the data set #241 received on May 24, after being processed with PC-PTR (a) and PC-EPTR (b), and for the data set #275 received on May 27, after being processed with PC-PTR (c) and PC-EPTR (d).

the numerical metrics it is clear that the performance of the system has been improved by using the EPTR processor.

Figure 4.15 shows, for each slot along the signal frame, the BER results of the data set #241 collected on May 24 after being processed by PC-PTR (magenta) and by PC-EPTR (red), and of the data set #275 collected on May 27 after being processed by PC-PTR (cyan) and by PC-EPTR (green). Observe that several slots of the data set #241 are error-free, both for the PC-PTR and the PC-EPTR, while the PC-EPTR results overcome the PC-PTR results in general, except for slot number 19. For data set #275, only the PC-EPTR yields error-free slots and its performance by far overcomes the results obtained with the PC-PTR.

Figure 4.16 shows the MSE results along the 20 slots of the signal frame, for data set #241 with PC-PTR processing (magenta circles/dashed line) and with PC-EPTR (red

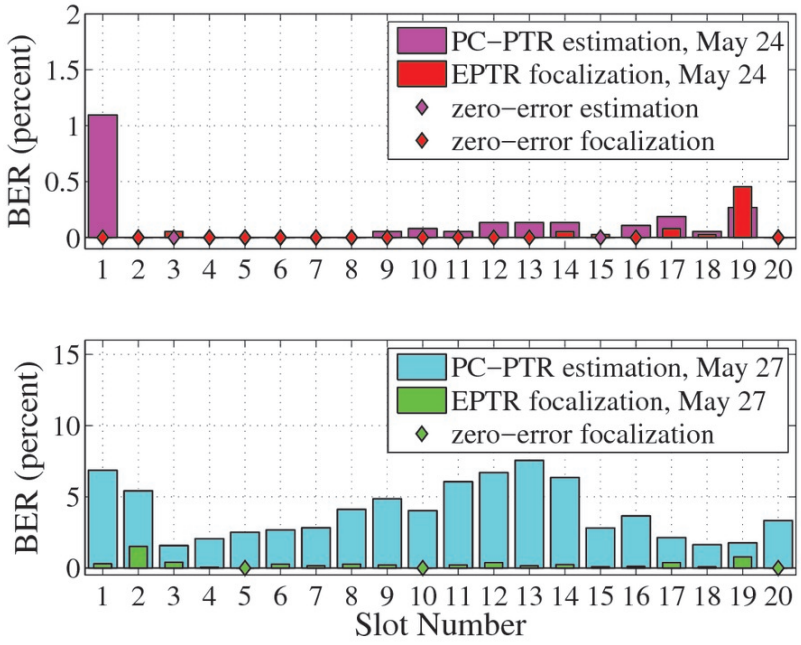

Figure 4.15: BER results per slot: May 24 data set #241 (upper subplot), PC-PTR (magenta) and PC-EPTR (red); May 27 data set #275 (lower subplot), PC-PTR (cyan) and PC-EPTR (green). The diamond marker denotes an error-free slot.

circles/dashed line), and for data set #275 with PC-PTR (cyan crosses/full line) and by PC-EPTR (green crosses/full line). The PC-EPTR results have a lower MSE then the PC-

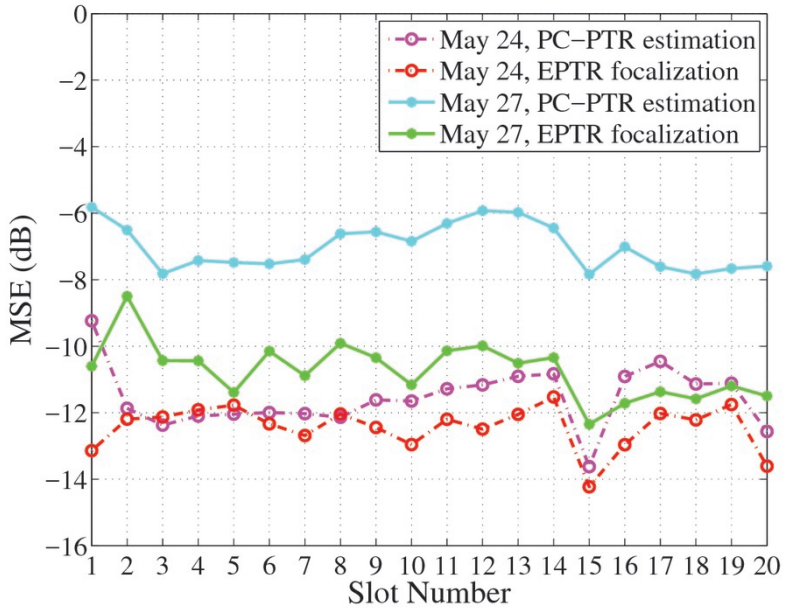

Figure 4.16: Mean square error of the received equalized communications signal for the full array. Results along the 20 slots in the data set #241 on May 24 with PC-PTR (magenta) and PC-EPTR (red), and in the data set #275 on May 27 with PC-PTR (blue) and PC-EPTR(green).

PTR both on May 24 and on May 27. In particular, on May 27, PC-EPTR outperforms PC-PTR by approximately 4 dB. Moreover, results shows a consistent improvement along the 20 seconds data frame.

4.2.5 Discussion

Sections 4.2.1 to 4.2.4 presented the results of coherent underwater acoustic communications that employ an environmental focalization algorithm for improving passive time-reversal performance. Environmental focalization works as a sub-processor that uses any available a priori or historical environmental information to search for numerical model outputs that best match the channel probe pulse compressed estimates. The fact that these model outputs are noise free while the originally used pulse compressed estimates are noisy, provides the potential for the processing gain.

The proposed EPTR algorithm is applied to real data sets acquired in two different days during the UAN'11 experiment carried out in Trondheim (Norway), over a range dependent shallow water 900 m long transect. QPSK modulated data packets were transmitted with a cNode-Mini Kongsberg modem at 4k bits/s during 20 s each day and were received on a 16 channel vertical array. The results obtained show that PC-EPTR outperforms standard PC-PTR by an amount varying from 1 to 4 dB, in MSE gain, over the two processed data records. The proposed method is shown to be robust yielding results that are nearly always equal or better than those provided by standard passive time-reversal, despite the considerable variation of channel responses both at micro-scale from second to second or from one day to the other. The results also show that the modeling errors (inevitably) present at the focalization algorithm output were small enough to still provide processing gain of the noise

present in the pulse-compressed channel estimate. To some extent the proposed method trades modeling errors for noise.

The focalization algorithm estimated CIR provides enough detail to capture and to follow over time the essence of channel variability. It is unknown whether that variability is due to sensor motion, surface agitation, currents or micro temperature changes, but a minimal set of physical parameters were able to track it and successfully undo channel paths by matched filtering the received signal on an array of receivers. The search space for the focalization was sufficiently small to be exhaustively covered, while still running in a reasonable time on a laptop computer.

To the authors best knowledge this is the first time that numerical modeling channel estimates were directly used for channel equalization of underwater acoustic communications with real data in an useful frequency range, say, over 20 kHz. In that regard, these results represent a step towards using the potential of connecting environment and channel compensation in field experiments.

4.3 Experimental results II: introducing the Reg-L1 in the comparison tests

In this section, coherent time-reversal underwater acoustic communications are tested with real data for performance comparison when using the following channel identification methods: pulse compression (PC), the $\ell 1$-norm regularization (RegL1) and the Environmental Focalization (EF) based on physical modeling. From the combination of these three methods with a time-reversal receiver, the following configurations are formed: PC-PTR, the RegL1-PTR and the EPTR. However, since the EF requires the use of observed CIR data (that can

be estimated by, *e.g.*, PC or RegL1) to serve as reference for optimization, then the EPTR can be be configured as PC-EPTR or RegL1-EPTR.

This section processes the data set #274 collected on May 27 (see Table 4.3), evaluating their MSE and bit error rate Bit Error Rate (BER) for performance analysis. Figure 4.17 shows for channel 8 the time variability of the estimated CIRs. Channel estimates are obtained with PC (a), modeled with environmental focalization based on PC (c), estimated with RegL1 (e) and modeled with environmental focalization based on RegL1 (g). Also, the mean magnitude of the CIRs is shown on the right column, for the four cases, PC (b), modeled based on PC (d), RegL1 (f) and modeled based on RegL1 (h).

Observe that the time-variant CIRs are sharper, *i.e.*, the path peaks have narrower lobes, when estimated with RegL1 than with PC. This is due to the sparse estimator design that includes $\ell 1$-norm regularization to better explore the sparsity of the CIR in shallow water. Further, note that, as expected, the modeled CIR generated by EF yields noiseless wavefronts and noiseless time-delay mean CIRs in comparison to PC, even though there are some delay mismatch for the later arrival. Despite this drawback, such mismatch tends to have a relatively small effect in the channel compensation processing because that delayed peak has a magnitude approximately 10 dB lower than the main peak. Also, one may observe that there is no significant difference comparing (d) and (h), for PC-EPTR and RegL1-EPTR, respectively.

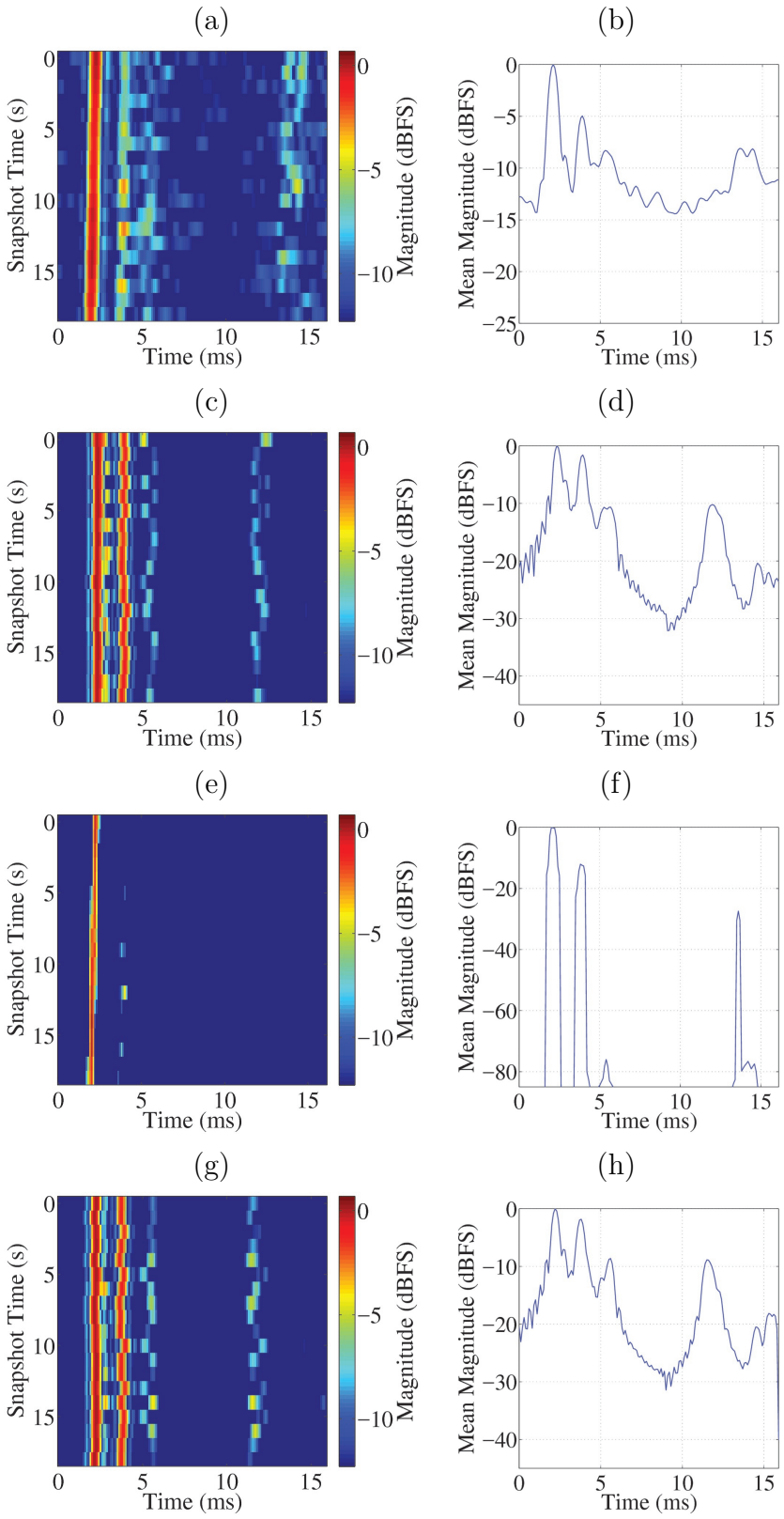

Figure 4.17: Channel number 8 estimated CIR from data set #274 with PC (a,b), modeled with environmental focalization by EPTR based on PC (c,d), with RegL1 (e,f) and modeled with environmental focalization by EPTR based on RegL1 (g,h). CIRs time variability (left) and mean power CIRs (right).

4.3.1 Results on communications performance

Figure 4.18 shows the results in terms of mean square error for the received signal after being processed by PC-PTR (blue crosses), with RegL1-PTR (red crosses), by PC-EPTR with PC environmental focalization (magenta circles) and by RegL1-EPTR with RegL1 environmental focalization (green stars), along 20 slots of the signal frame #274 containing the payload image data.

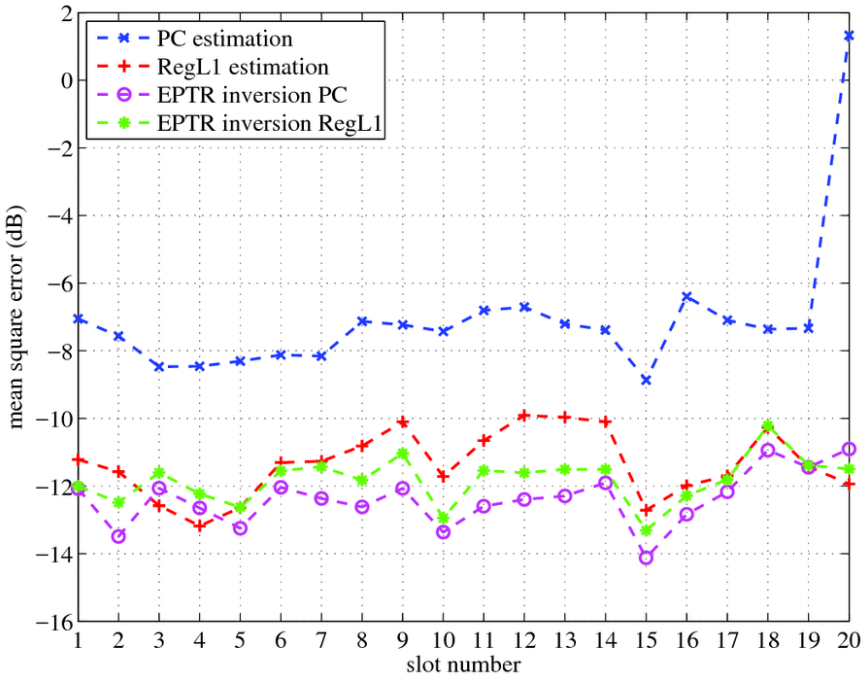

Figure 4.18: MSE results of May 27 data (signal identification number 274) with PC estimation (blue), RegL1 estimation (red), PC environmental focalization (magenta) and RegL1 environmental focalization (green).

The PC-EPTR yields the higher performance in terms of MSE for this data set #274. The RegL1-EPTR yields similar results to the PC-EPTR, but with slightly worse MSE performance of ∼1 dB. Also, the PC-EPTR reached a performance ∼4 dB superior to PC-PTR and marginally better (<1 dB) than RegL1-PTR.

The improvement of the PC-EPTR using environmental focalization over the PC-PTR

using pulse compression estimation can be explained by the fact that the channel replicas obtained with environmental focalization are noise-free while the pulse compression channel estimates are unavoidably noisy. Therefore, assuming that the environmental focalizer succeeds to mitigate the CIR modelling errors, a gain is generated for PC-EPTR over PC-PTR.

The focus now resides in comparing PC and RegL1 for both PTR and EPTR. The EPTR based on PC has improved performance relative to EPTR based on RegL1. This is due to the fact that RegL1 tends to suppress less significant paths, which can probably degrade the matching between observation and modeled replicas performed with the environmental focalization processor.

The PTR based on RegL1 has much better performance relative to PTR based on PC. This is due to the fact that RegL1, using sparse estimation techniques, significantly reduces the noise effects and side lobes relative to the noisy estimate obtained with PC.

Figure 4.19 shows the received symbols along time after being processed by the PC-PTR (a) and with the PC-EPTR (b). The figure shows that the symbols variance relative to the symbol map (marked as red lines) is clearly reduced in RegL1-PTR (plot c) relative to PC-PTR (plot a), as well as the EPTR (plots b and d, on the right) presents the highest improvement relative to PC-PTR. Also, the PC-EPTR and the RegL1-EPTR present similar results.

Figure 4.20 shows the transmitted low resolution image (a), and then the recovered image with: PC-PTR (b), RegL1-PTR (c) and after EPTR processing based on PC (d). The received image processed by the PC-PTR (b) presents several wrong pixels (1707 symbol errors). The image processed by RegL1-PTR (c) corrects significantly the errors, however

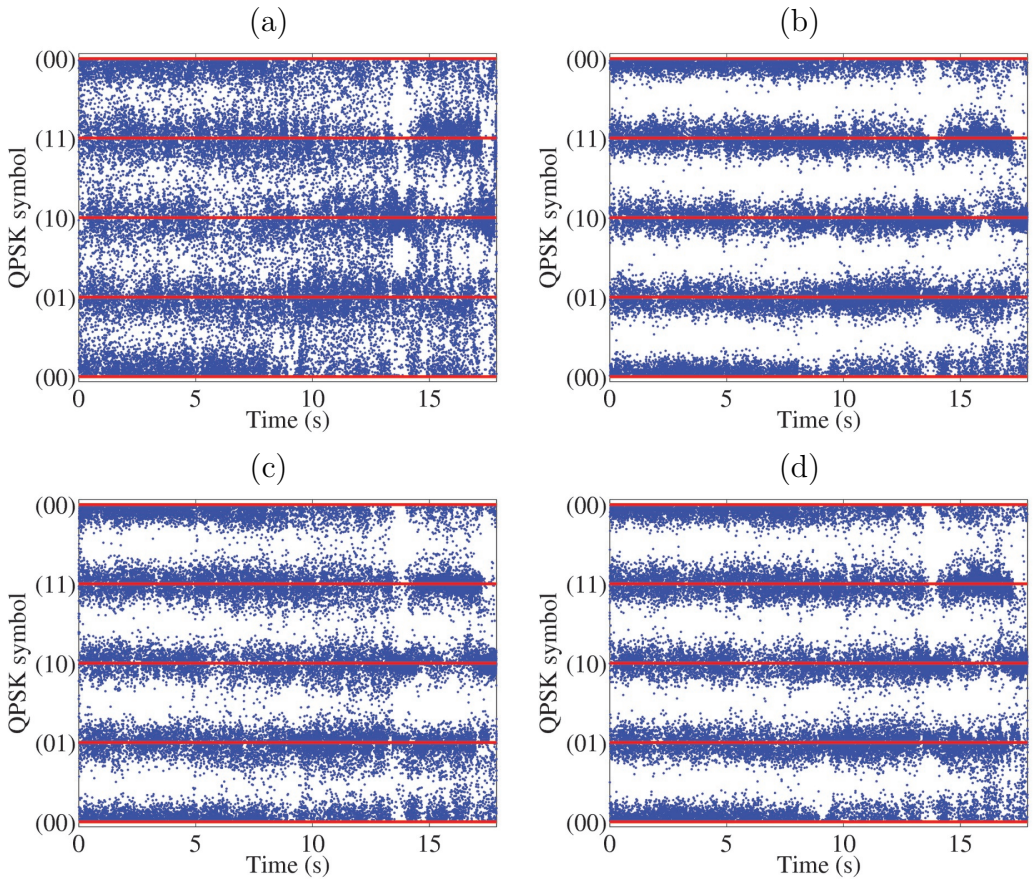

Figure 4.19: Received symbols along time after processing with the PC-PTR (a), PC-EPTR (b), RegL1-PTR (c) and RegL1-EPTR (d). The vertical axis denotes the bit pairs corresponding to the angles of recovered QPSK symbols. The horizontal axis is the effective time of payload transmission.

remaining 132 wrong symbols. The image processed by EPTR (d) corrects most of such errors (just 31 wrong symbols remain), yielding an image quite similar to the transmitted image of (a), thus presenting a clear communication performance improvement driven by the use of physical channel modeling coupled with environmental focalization.

4.3.2 Discussion

This subsection includes the RegL1 sparse estimator in the processing for PTR and EPTR for the data frame #274. The results obtained for RegL1-PTR and RegL1-EPTR were compared to the results of PC-PTR and PC-EPTR. The experimental results suggest that the RegL1 offers greater advantage in PTR and is not so advantageous in EPTR.

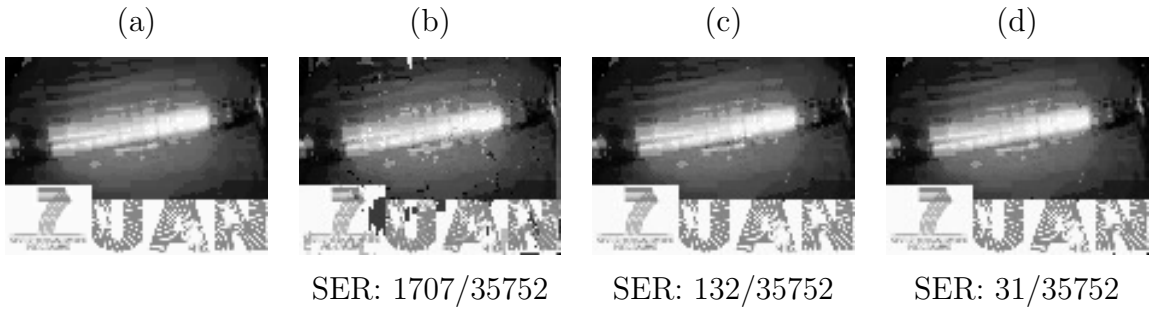

Figure 4.20: Transmitted low resolution image (a), and the recovered image: with PC-PTR estimation (b), with RegL1-PTR estimation (c), and after processing by EPTR focalization (d). The corresponding symbol error rates (SER) are given bellow the received images.

The comparison of RegL1-PTR to PC-PTR showed that the sparse approach reduces substantially the amount of symbol errors. This is due to the fact that the RegL1 explores the sparse nature of the CIR in the underwater waveguide channel, using the $\ell 1$-norm factor, to regularize the classical $\ell 2$-norm estimation. The results were presented to for a regularization factor (γ) of 2.3 (see Eq. 2.20), chosen empirically from previous simulations for the scenario of the UAN11 sea trial. The $\ell 1$-norm tends to give a higher weight to the strong paths in the sparse channel impulse response, reducing the effects of noise and side lobes in the CIR, which otherwise are unavoidable in PC estimation.

The comparison of RegL1-EPTR to PC-EPTR showed that their performance is similar, with the RegL1-EPTR presenting the disadvantage of an increase of the computational cost. The PC-EPTR appears to be the better option for applying the environmental focalization method.

Experimental results yield reasonably low mean square error, allowing to recover the transmitted image with low error, reaching an MSE of approximately -10 to -13 dB for RegL1-PTR and EPTR over a real channel of 890 m range and depth between 34 m and 98 m.

The results obtained from this data set show that the proposed environmental-based approach outperforms the other two channel identification methods. Nonetheless, as will be shown in the long term analysis (Sec. 5.4), this is not always the case.

The RegL1-EPTR will not be presented in the next section for long term analysis because its performance is similar to PC-RegL1 and its computational cost is higher. Therefore, for simplicity of notation, the PC-EPTR results are here after referred just as EPTR.

4.4 Experimental results III: long term analysis

This section presents the results of the PC-PTR, RegL1-PTR and PC-EPTR (here just referred to as EPTR) for a long term performance analysis. By long term we mean that there is a significant increase of the amount of data processed in comparison to to that analyzed in the last two sections. In this section ten data sets containing 200 slots and the total amount of five hundred thousand QPSK symbols (thus one million bits) are analyzed.

The transmissions were performed within a period of three days, being the first signal collected on May 24 at starting time 20h35m and the other nine signals mostly on May 27, with the last data set recording ending at 00h05m on May 28 (see Table 4.3). For all these data sets the results of EPTR are compared to the corresponding results of RegL1-PTR and PC-PTR, aiming at checking the performance of EPTR, its probable gain in a general wide view, and its robustness over time.

4.4.1 Performance analysis

The long term analysis is presented in terms of MSE performance of the standard PC-PTR, the sparse RegL1-PTR and the proposed EPTR for the ten data sets of Table 4.3. Figure 4.21 compares the results of the PC-PTR, RegL1-PTR and EPTR, in terms of MSE. The

symbol slots are denoted for PC-PTR (red triangles), RegL1-PTR (blue crosses) and EPTR (green diamonds).

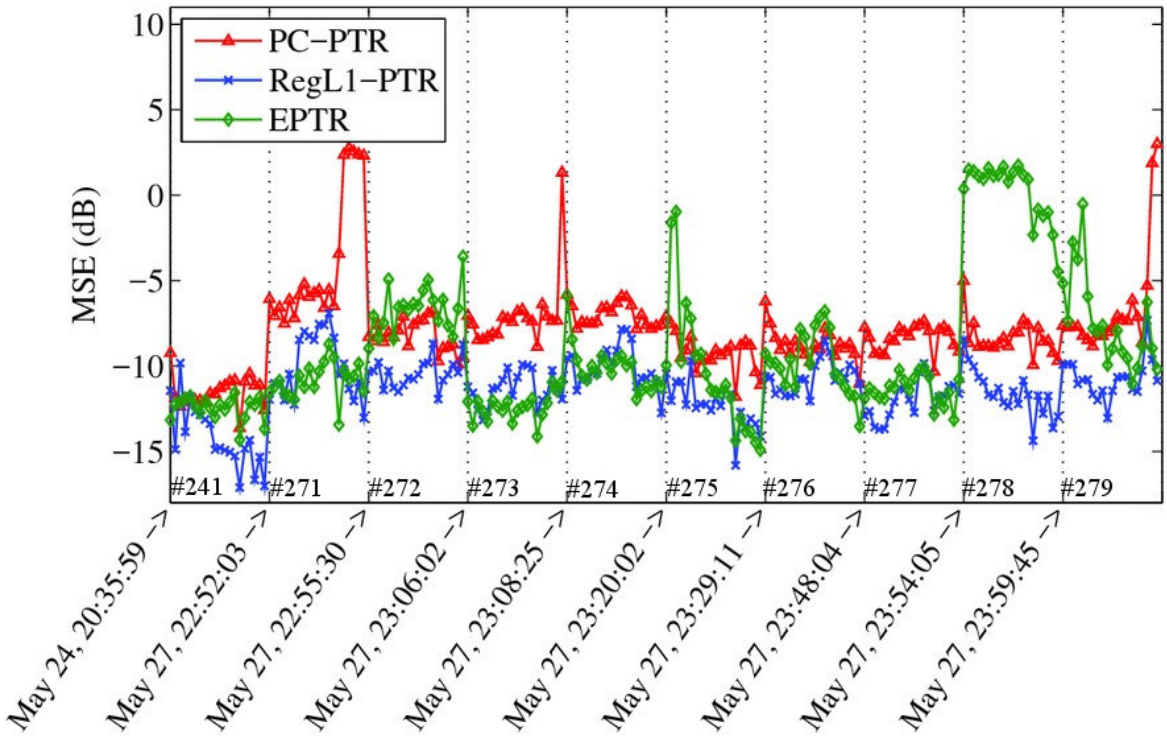

Figure 4.21: MSE of soft-decision recovered symbols obtained by EPTR (green diamonds), RegL1-PTR (blue crosses) and PC-PTR (red triangles) along ten data frames between May 24 and May 27.

Each green diamond, blue cross or red triangle represents a slot containing 1873 QPSK symbols of image message. The vertical dotted line separate the data sets, each one containing 20 slots (thus 35752 symbols of a whole image message).

The figure indicates that the MSE results of RegL1-PTR outperformed the conventional PC-PTR in most of the slots, *i.e.*, except 3 out of a total of 200, noting that each point (red triangle, blue cross or green diamond) shown in Fig. 4.21 represents a single slot. In terms of data sets (groups of 20 slots), theRegL1-PTR outperforms PC-PTR results for all the data. Also, the figure indicates that the EPTR (green diamonds) reasonably outperformed the conventional PC-PTR (red triangles) for seven of the total amount of ten data sets (#241,

#271, #273, #274, #276, #277 and #279). However, the EPTR had a performance lower than that of the RegL1-PTR (blue crosses) in seven of ten data sets (#241, #272 and #275 to #279).

Furthermore, for the sake of clarity in presenting the long term results, Figures 4.22 and 4.23 show the data results of Fig. 4.21 in sub-figures for each data set separately. Table 4.6 shows the MSE results for each data set after being processed by PC-PTR, RegL1-PTR and EPTR and the corresponding gain obtained with RegL1-PTR and EPTR.

Table 4.6: MSE with PC-PTR, RegL1-PTR and EPTR for ten signals collected in UAN11 experiment.

	MSE (*dB*)			**Gain ref. PC-PTR (*dB*)**	
Data set nr.	**PC-PTR**	**RegL1-PTR**	**EPTR**	**RegL1-PTR**	**EPTR**
241	-11.60	-13.86	-12.56	2.26	0.96
271	-1.89	-9.69	-10.88	7.80	8.99
272	-8.29	-10.62	-6.87	2.33	-1.42
273	-5.74	-11.39	-12.54	5.65	6.80
274	-7.13	-9.99	-10.04	2.86	2.91
275	-9.22	-12.21	-8.22	2.99	-1.00
276	-8.78	-10.74	-9.51	1.96	0.73
277	-8.48	-12.05	-11.53	3.57	3.05
278	-8.37	-11.55	-0.44	3.18	-7.93
279	-4.79	-10.75	-6.59	5.96	1.80

These results clearly indicate that the RegL1-PTR had the best performance, reaching results with MSE between -13.86 dB and -9.69 dB. The second best performance was achieved by the EPTR (except for the failed data set #278) with MSE in the range between -12.56 dB and -6.59 dB. The PC-PTR presented the worse performance with MSE in the range between -11.60 dB and -4.79 dB.

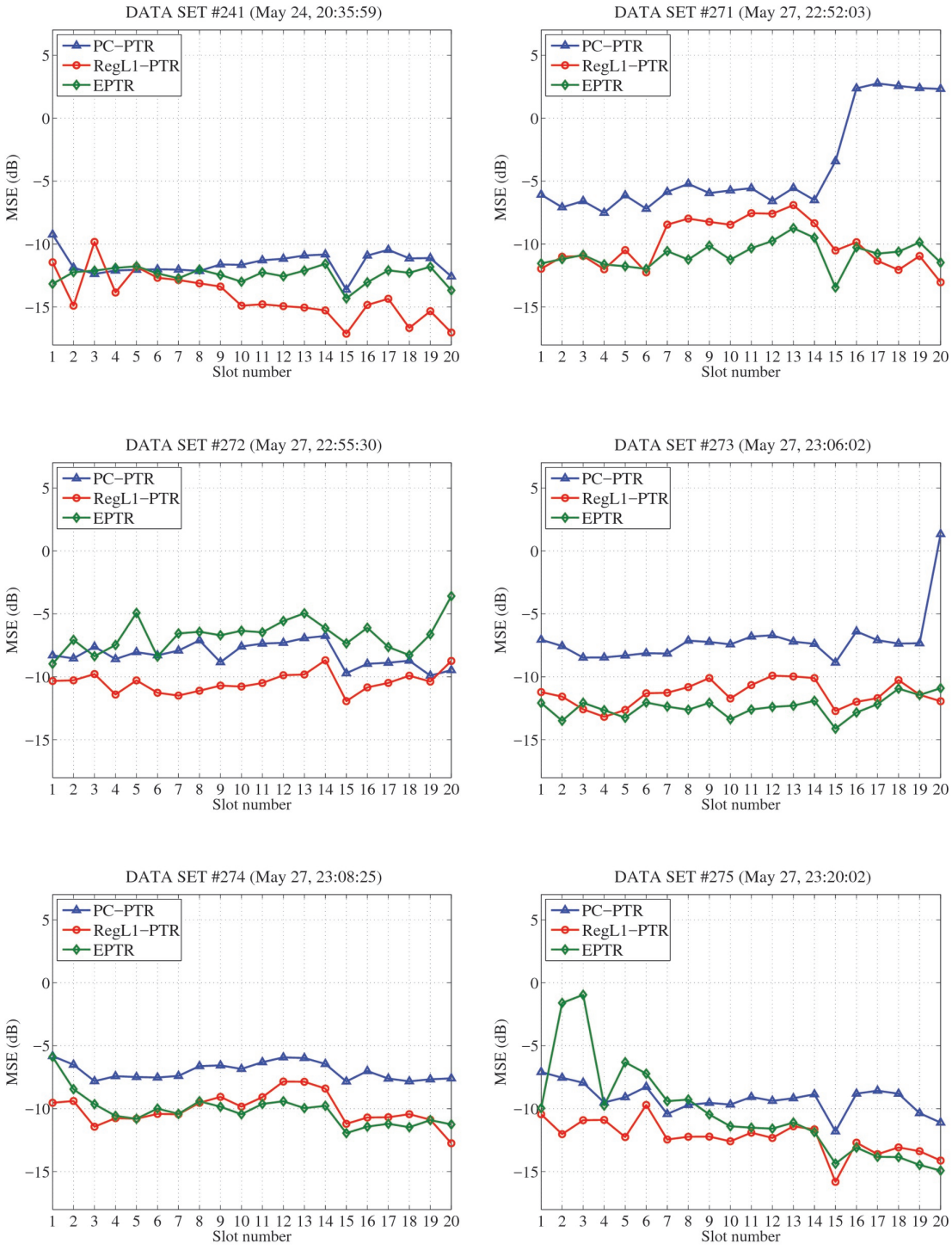

Figure 4.22: MSE of soft-decision recovered symbols for the data sets #241 and #271 to #275 after being processed by EPTR (green diamonds), RegL1-PTR (blue triangles) and PC-PTR (red circles).

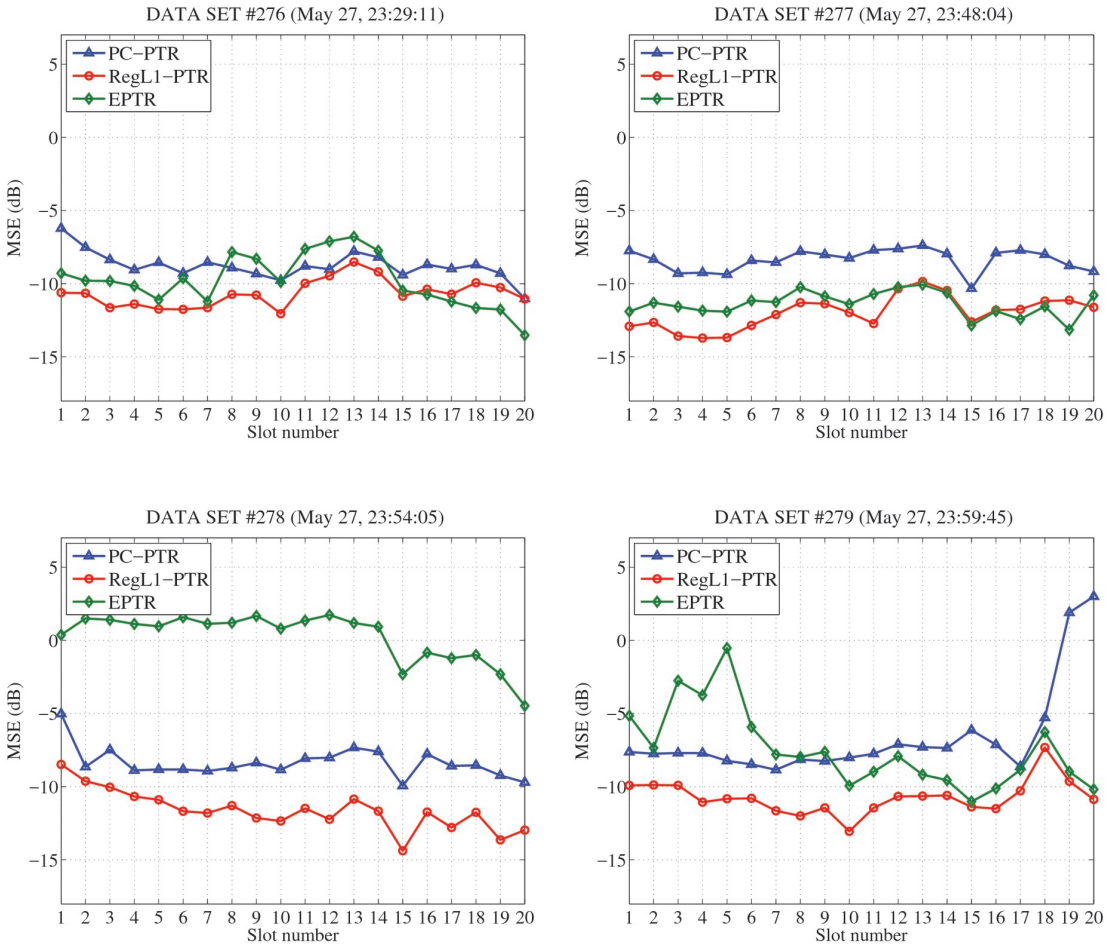

Figure 4.23: MSE of soft-decision recovered symbols for the data sets #276 to #279 after being processed by EPTR (green diamonds), RegL1-PTR (blue triangles) and PC-PTR (red circles).

4.4.2 Channel identification issues

The long term analysis showed that the EPTR MSE performance for the data set #278 severely failed, since most of the slots of this frame have a MSE of ∼0 dB (see Fig. 4.23). This fact may be due to a failure in the synchronization of the CIR snapshots, in the sense that the CIR replica from EF must be aligned to the CIR estimate used as reference by the Bartlett objective function for the CIR optimization. Although the procedure was successful for most the data sets, this was not the case for the data set #278. To illustrate this fact, Fig.4.24 shows the CIR replicas obtained with EF for the hydrophone 8 data set #278, where

the CIR alignment failed, and Fig.4.25 shows for the hydrophone 8 data set #274, where the CIR alignment was successful.

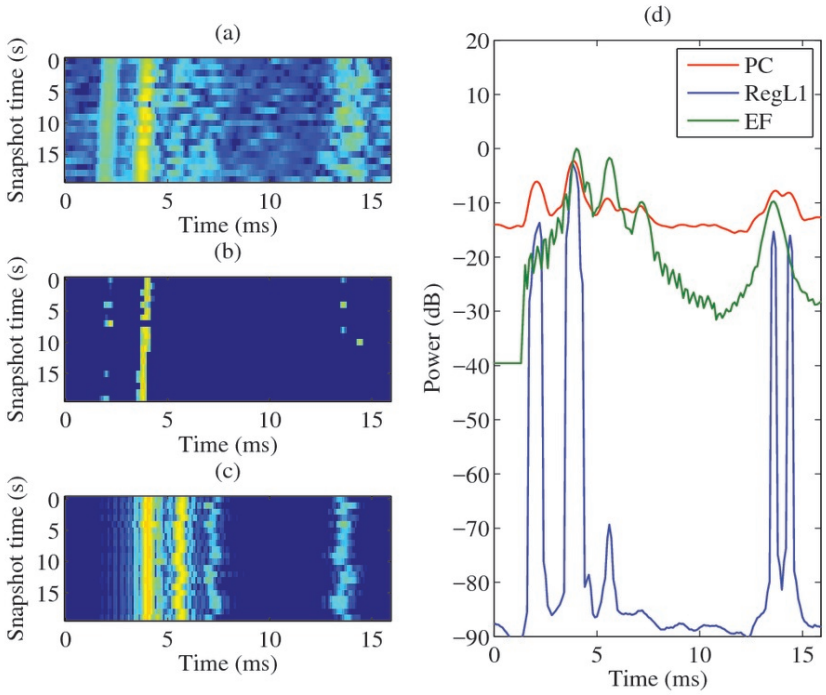

Figure 4.24: Failure in CIR alignment for the hydrophone 8 **data set #278**. Plots (*a*), (*b*) and (*c*) show the CIR in 2D representation for PC, RegL1 and EF, respectively. Plot (*d*) shows the average magnitude CIR computed with PC (red line), RegL1 (blue line) and EF (green line). The first path of EF channel replica wrongly aligned with the second path of PC channel estimate.

In the results of Fig. 4.24 obtained from data set #278, the first path delay for PC (*a* and *d*) and RegL1 (*b* and *d*) is at ∼0.2 ms while for EF (*c* and *d*) is at ∼0.4 ms, indicating a misalignment of higher amplitude paths in the EF case, which means that a synchronization failure occurred. This fact helps to explain the very low MSE performance of EPTR for the data set #278 shown (in green line) in Fig. 4.23. This loss of performance, caused by the synchronization failure, is most probably due to an estimation error of the relative amplitude of the two main peaks with the EF (see Fig. 4.24).

The synchronization processing of the complete set of data frames was done automatically, *i.e.*, without manual intervention, to test the capability and robustness of the system as a

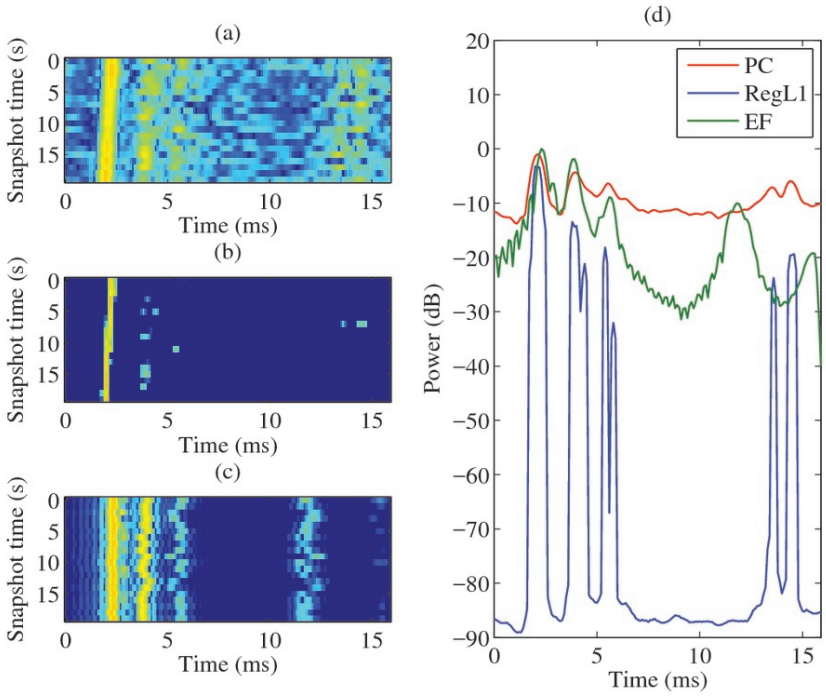

Figure 4.25: Correct CIR alignment, in the sense of an accurate time position of the main path, for the hydrophone 8 **data set #274**. Plots (*a*), (*b*) and (*c*) show the CIR in 2D representation for PC, RegL1 and EF, respectively. Plot (*d*) shows the average magnitude CIR computed with PC (red line), RegL1 (blue line) and EF (green line).

whole. Since in Fig. 4.24 the relative path delays are well estimated by the EF, it is expected that an improvement of the synchronization algorithm could recover, at least partially, the performance loss of EF for data set #278 in Fig. 4.23.

Fig. 4.25 (d) shows a reasonably good match between EF, RegL1 and PC for the path delays, except for a mismatch of the later arrival, which is not a severe issue since this arrival refers to a path with low amplitude (10 dB smaller than the main peak), having low influence in the time-reversal performance.

4.4.3 Discussion

In terms of robustness, the most stable results were reached in ascending order by: EPTR, PC-PTR and RegL1-PTR. This ranking is justified by the fact that RegL1-PTR was

successful in all data sets, the PC-PTR presented 8 failed slots and the EPTR presented 15 failed slots of a total amount of 200 slots processed (see Fig. 4.22 and 4.23). The assumption to define a failure is an MSE greater then -1 dB. Although EPTR was the less stable in terms of robustness, its results in terms of performance (with exception of the few failed data) showed a high level of data recovery. However, in 3 out of the 10 data set analyzed the EPTR did not outperform the PC-PTR (data sets #272, #275 and #278). The average gain achieved by EPTR over PC-PTR for the 7 data sets that were successful was 4.7 dB.

The probable reason for the EPTR failure in 15 out of 200 slots or, in other words, for not have outperformed the PC-PTR in the data sets #272, #275 and #278 may be due to a synchronization error in the alignment of the modeled replica to the reference CIR estimate or alternatively due to an insufficient resolution in the search space to represent the actual channel during the transmission time of a data set. The size of the "a priori" search space employed in the EF processor was 5000 replicas, as shown in Table 4.4, where it was assumed that this amount could be sufficient to generate a CIR replica candidate to successfully represent the channel for equalization while spending a tractable computational cost ($\sim$1 hour in a laptop with 4 cores). However, one may expect that increasing the "a priori" search space size, the "a posteriori" CIR replica probably may be improved. This test with a huge search space (and huge computational cost) was not performed in the present work, being intended to be done in future steps. Despite of that, in general, the EPTR results obtained in this work using a 5000 replicas search space were reasonably good, often outperforming a conventional PC-PTR. The lack in synchronization precision for some signals may be caused by path destructive interference in channels that have a

surface-reflected path arriving at approximately at the same time of the direct path in some sensors. This phenomenon may cause distortion in the amplitude of the CIR main path and thus produce inaccurate synchronization based in probe-based matched filter.

In terms of performance, the best results were reached in ascending order by: PC-PTR, EPTR and RegL1-PTR. This ranking is clearly indicated in Fig. 4.21. Both the RegL1-PTR (for all slots) and the EPTR (for the successful slots) show significant gain over the PC-PTR, reaching values in the interval of 1.96 dB to 7.80 dB for RegL1-PTR and of 0.73 dB to 8.99 dB for EPTR. Further, for seven data sets the RegL1-PTR has the best performance. But for the other three data sets (#272, #274, #275) the EPTR has the best performance, with gain up to $\sim$1 dB over the RegL1-PTR.

Moreover, beyond those particular results presented for the case of the UAN11 experiment, a remarkable point is that the EPTR does include physical information of the environment, thus creating a connection between the receiver and the location where it is employed. The issue of including the channel physics in the underwater acoustic channel equalization has not been well explored in underwater acoustic communications. However, it is an essential aspect to be considered for compensating the channel distortions over the received signal, in the sense that the sound speed profile, the source-receiver location and the geoacoustic parameters of the seabed, as well as the dynamic nature of the ocean environment, have a strong effect in the received communications signals.

As described in [77], the additive Gaussian noise channel model is seldom appropriate for representing signal propagation at communications carrier frequencies and perhaps the only exception to this are short-range direct path channels in the deep ocean. There are numerous acoustic propagation models of transmission loss and impulse responses, but they

have not been applied in a form useful for designing a communications system. Even so, a fundamental issue in underwater acoustic communications systems is to match the channel physics to the parameters of the system.

The EPTR aims to insert the channel physics through the usage of environmental focalization (EF). The EF is not independent of the channel estimation in the sense that it employs a CIR estimate in the objective function for optimization of a search space of "a priori" parameters that yields the "a posteriori" CIR replica. In spite off that, the EF showed in this work that the physical parameters of the channel can be usefully employed to improve underwater communications. Therefore, the EPTR represents a step forward in the direction for including channel physics to help in overcoming the severe difficulties often found in underwater channel equalization, specially in shallow water scenarios.

At the present status of this work, we did not search for physical parameter estimation, but for CIR modeling aiming at improving underwater communications. However, one may note that "a posteriori" parameters are generated as a by-product of EF. This feature is promissory in the sense that one may, in future, design an equalizer in which instead of using abstract coefficients, would use coefficients of environmental parameters. Thus, such type of equalizer would be able to simultaneously perform underwater communications and acoustic inversion.

Chapter 5
Conclusions

Preview *This chapter presents an overview of the work done in this thesis in the framework of previously reported results, as well as suggest future work. Section 5.1 presents the work overview with concluding remarks; Section 5.2 summarizes the work contributions; and Section 5.3 points out some possible future directions for tasks not covered in this thesis.*

5.1 Concluding remarks

This work addresses environmental model-based equalization of coherent underwater acoustic communication channels. Emphasis is given to shallow water scenarios where a natural waveguide is formed creating a complicated propagation pattern driven by multiple boundary reflections between the seabed and the sea surface. A proposal of digital equalization method based on joint physical modelling and environmental focalization is is made, as an enhancement of the Passive Time-Reversal (PTR) receiver.

The PTR requires the use of single-input-multiple-output link with a sufficiently dense receiver-array to capture the main propagating modes, as well as the usage of a probe signal in order to estimate the Channel Impulse Response (CIR) which is employed in time-reversal filtering. If the channel is stable along the transmission time and the CIR is accurate enough, then the PTR can significantly reduce the Inter-Symbol Interference (ISI). The precision of

the CIR is a fundamental point in PTR, since even small inaccuracies can cause sufficient mismatch in the time-reversal filters to severely decrease the communication performance.

Channel identification in PTR is usually done by Pulse Compression (PC), which performs matched filter based on the probe signal. In real data, PC channel estimates are usually affected by noise in the received probe signal. The PC is based on classical $\ell 2$-norm estimation and can be derived from the Minimum Variance Unbiased (MVU) estimator, which is robust but is not the most accurate method in the case of sparse channels. For such channels, there are sparse estimators that can generate CIR estimates with improved accuracy. This is the case of the Regularized $\ell 1$-norm (RegL1) method, which uses a technique inspired in compressive sensing to find an accurate sparse solution. The RegL1 is used in this work for shallow water channel estimation under the assumption that the CIR in shallow water environment is nearly sparse. These two methods, PC and RegL1, are tested in PTR with real communications data and are used as ground truth to the proposed method hereby named Environmental-based Passive Time-Reversal (EPTR).

The EPTR was designed in this work with the objective to improve time-reversal communications performance through the mitigation of noise effects on CIR identification. The proposed method inserts noise-free acoustic propagation modelled CIR replicas in time-reversal filtering, relying on an Environmental Focalization (EF) algorithm to sufficiently reduce modelling error. The EF algorithm tweaks the environmental parameters to obtain a noise-free physical model CIR that best matches the observed channel data. This process is inspired in Matched Field Processing (MFP), a well-known technique used in low frequency (less than 2 kHz) source localization problems. The EF is designed to operate in usual underwater acoustic communications frequencies, *i.e.*, between 10 kHz and 30 kHz, employ-

ing a ray/beam trace model to generate the CIR replicas for a search space of candidates driven by a set of "a priori" physical parameters. The focalization generates as output an "a posteriori" noiseless CIR replica with the best fitness in the Bartlett objective function sense that correlates modeled CIR candidates with a CIR estimate. Therefore, the noise error in CIR estimates is replaced by some degree of modeling error, which is expected to be small enough when the EF is successful, thus improving the communication performance. Also, the understanding on the influence of the acoustic propagation physical parameters in high-frequency underwater communications is essential to efficiently select an appropriate search space, increasing the chance of EF success to mitigate modelling error.

The EPTR processor was tested with real data, whose results indicated the feasibility of the method. In this sense, the EPTR contributes to a step forward in the direction on understanding of how physical modelling can help to estimate and compensate channels in real underwater acoustic communications. It has an innovative character in the sense that, for the best knowledge of the author, no report was found on equalization with real data using physical models. A drawback of the EPTR is the increased complexity, where the computational time depends of the number of "a priori" CIR replicas in the search space, which in our study was exhaustively searched for optimization. The advantages of the EPTR are (*i*) to increase the communications performance through the substitution of noise effects in channel estimates by the reduced modelling error, under the assumption that the EF is successful in tracking the actual channel; and (*ii*) to use the environmental information to improve channel identification in communications, thus contributing to make the system more robust for the employment in different scenarios.

Acoustic communication transmissions performed during the "Underwater Acoustic Net-

work 2011" experiment conducted on the coast of Trondheim (Norway) were used as test cases for the proposed algorithms. Several quadrature-phase-shift-key digitally modulated data sets containing a low-resolution image were transmitted at 4 kbit/s between a moored source and a 16-hydrophone vertical moored array situated at 890 meters range. The data sets collected in the sea trial are processed with EPTR, being then compared to RegL1-PTR and to a standard PC-PTR. The PC-PTR is the standard time-reversal receiver that uses pulse-compressed CIR estimates; the RegL1-PTR is a modified version of the PTR that employs sparse channel estimates obtained by $\ell 1$-norm regularization, the PC-EPTR is the proposed method of this work that employs EF based on physical modelling to feed the time-reversal filters, where EF is the environmental focalizer that generates the noise-free CIR that best matches a pulse-compressed CIR estimate; and RegL1-EPTR is a modified version of the PC-EPTR whose difference is to use a RegL1 CIR estimate, instead of a PC estimate, in the EF processor. The experimental results show that the proposed EPTR method (both using PC and RegL1 in EF) outperforms the conventional PC-PTR, robustly yielding mean square error gain in a range of approximately 1 to 8 dB.

The present work showed evidence to support that:

- The most important part of the seabed for the communication signals propagation at high frequency is the sediment layer. More specifically, the sediment compressional sound speed affects the CIR time-spreading and the path delays in the reduced-time axis, which is an important feature to consider when choosing candidates for the search space of EF, given that path delay is more important than path amplitude for channel compensation.

- The Sound Speed Profile (SSP) is known as an important parameter for acoustic propagation, but it was not inverted for in the EF tests of this work. Instead, it was used SSP data from an *in situ* CTD measurement, aiming to avoid generating unrealistic replicas. The EPTR performed well without the inversion of the SSP in this work, which infers that EF may be able to compensate the SSP variability with an artificial variability of the parameter being inverted. However, this conclusion may not be final because perhaps in another environment the EPTR may require SSP inversion to performed well, and therefore this issue must be treated with caution.

- The geometric parameters are those with a highest impact on the CIR and PTR processing. The movement of sensors or scatter points during the transmission time cause Doppler distortion, which can be severe even for small velocities. If not mitigated or compensated, Doppler effect can severely affect the communications performance. In case of non intentional motion applications (*e.g.*, fixed nodes), one may significantly reduce such effects by employing moored sensors and mitigating the residual distortion with resampling techniques. Further, the acoustic propagation is very sensitive to the variation of geometric parameters. In this sense, the EF should be set to have an "a priori" search space with high resolution for geometric parameters. Thus, a wide range of different modeled CIR candidates would be generated, increasing the chance of reaching a small misfit between the observed CIR and the "a posteriori" CIR replica.

- For environmental focalization, small wavelength effects suggest the usage of high resolution parametrization in the "a priori" geometric parameters of the search space; the low influence of sub-bottom parameters suggests their exclusion from the opti-

mization, thus saving computational cost without significant loss of communications performance; and the high sensitivity to sediment compressional sound speed suggests to increase its search space sampling, aiming to explore its delay shift feature. Such empirical knowledge, learned in Chap. 4 with the simulated sensitivity tests regarding the impact of environmental parameters variability on the CIR and time-reversal performance, was applied with real data to the EPTR in Chap. 5, achieving reasonably successful message recovery.

Moreover, a remarkable aspect of the EPTR resides in providing inverted physical parameters as output, since the EF algorithm works analogously to a standard acoustic inversion processor, but with the difference of employing reduced search space, small enough to be used with exhaustive search but with enough size to still generate an accurate CIR for time-reversal processing. The estimation of accurate "a posteriori" physical parameters was not the goal of this work, which concerns specifically to improve CIR identification for time-reversal communications.

The EF generates a set of physical parameters that optimize the objective function designed to select the CIR replica that best matches a CIR estimate used as reference, no matter if the obtained parameters represent the actual parameters of the environment. This is enough to increase PTR performance but it is not enough for acoustic inversion. In this sense, the author suggest that the EPTR design could be modified to include, in future work, large search spaces and a global optimization tool as, *e.g.*, genetic algorithm or simulated annealing. Such procedure could be useful to design a system able to jointly perform accurate acoustic inversion and underwater acoustic communications.

5.2 Contributions

The contributions of this work may be summarized as follows:

1. The physical parameters sensitivity was tested in high-frequency (12 kHz) shallow water communication simulations. The information reached are useful to get directions on how to appropriately set a input search space for high-frequency environmental focalization processing.

2. A new processor EPTR is proposed to improve PTR communications using a physical model-based approach for channel identification. The EF algorithm, inspired in matched field processing, is proposed as part of the EPTR.

3. Real data of coherent underwater acoustic communications at 4 kbit/s were successfully processed with EPTR, obtaining enhancement of performance, with results that outperform the conventional PC-PTR processor and, in few cases, also outperformed the sparse RegL1-PTR processor.

These contributions are summarized in the following published material:

1. L. P. Maia, A. Silva and S. M. Jesus, "Time-variant adaptive passive time-reversal equalizer and a perspective for environmental focusing method", in Proceedings of the *4th International Conference on Sensor Networks (SENSORNETS'15), Angers, France*, pages 103-108, February 2015.

2. L. P. Maia, A. Silva and S. M. Jesus, "A perspective for time-varying channel compensation with model-based adaptive passive time-reversal", *Sensors & Transducers Journal, ISSN: 2306-8515, e-ISSN 1726-5479*, vol.189 (6), pages 89-96, June 2015.

3. L. P. Maia, A. Silva and S. M. Jesus, "On equalization for mobile digital acoustic underwater communications", Poster in *Ciência 2016, Lisboa, Portugal*, July 2016.

4. L. P. Maia, A. Silva and S. M. Jesus,"Experimental results of environmental-based passive time reversal in underwater communications", *MTS/IEEE/OES Oceans'2017 Conference, Aberdeen, United Kingdom*, June 2017.

5. L. P. Maia, A. Silva and S. M. Jesus,"Environmental model-based time-reversal underwater communications", *IEEE Access Journal*, DOI 10.1109/ACCESS.2017.2724304, June 2017.

6. L. P. Maia, A. Silva and S. M. Jesus,"A long term analysis of environmental model-based time-reversal communications in the UAN'11 Experiment", *Journal of the Acoustic Society of America - Express Letters*, (submitted), September 2017.

5.3 Future work

Future directions are pointed as follows:

- To perform long term performance analysis of real data of other experiments for EPTR communications, testing the effects of different scenarios on the EF ability to generate realistic replicas to represent the actual channel. To test several scenarios with particular environmental parameters, bathymetry and transect ranges, as well as to test different configuration of communications parameters as, *e.g*, bit rate, digital modulation scheme, carrier frequency and pulse bandwidth;

- To implement other types of objective function than the Bartlett processor in the environmental focalization. To insert a global optimization algorithm in the process

to select the maximum "a posteriori" set of parameters from the "a priori" search space. The global optimizer would make it possible to extend the size of the search space, bringing probable advantages to the ability of the EF algorithm to generated CIR replica with very low modelling error.

- To design an algorithm to improve CIR synchronization, thus avoiding that the misalignment between the modeled CIR and the observed CIR performed during the processing of the EF may impair the performance of the EPTR.

Appendix A

Derivation of the minimum variance unbiased estimator

Classical channel estimation with ℓ_2-norm - MVU

Assume the system defined by (2.9). The multivariate probability density function when $\mathbf{w} \sim \mathcal{N}(\mathbf{0}, \sigma_w^2\mathbf{I})$ for the observed vector $\mathbf{y}$ given that true $\mathbf{g}$ occurs is

$$p(\mathbf{y};\mathbf{g}) = \prod_{n=0}^{N-1} \frac{1}{(2\pi\sigma_w^2)^{\frac{1}{2}}} \exp\left[-\frac{1}{2\sigma_w^2}\mathbf{w}^T\mathbf{w}\right]$$

$$= \frac{1}{(2\pi\sigma_w^2)^{\frac{N}{2}}} \exp\left[-\frac{1}{2\sigma_w^2}\sum_{n=0}^{N-1}(\mathbf{y}-\mathbf{S}\mathbf{g})^T(\mathbf{y}-\mathbf{S}\mathbf{g})\right] \tag{A.1}$$

where $\mathbf{w}$ denotes noise, σ_w^2 denotes the noise variance, $\mathbf{g}$ denotes the channel impulse response and $\mathbf{S}$ is a Toeplitz matrix of the transmitted signal $\mathbf{s}$.

If the Cramer-Rao Lower Bound theorem is satisfied, then it is possible to determine the optimal MVU estimator, as described in [35]. Such theorem defines that the MVU estimator exists if

$$\frac{\partial \ln p(\mathbf{y};\mathbf{g})}{\partial \mathbf{g}} = (\mathbf{C}_{\hat{\mathbf{g}}})^{-1}(\hat{\mathbf{g}}-\mathbf{g}) \tag{A.2}$$

where $\hat{\mathbf{g}}$ is the estimator and $\mathbf{C}_{\hat{\mathbf{g}}}$ denotes the covariance matrix of the estimator. Developing the left side of equation (A.2) one can deduce the estimator and its covariance, as follows

$$\frac{\partial}{\partial \mathbf{g}}\left[-\ln(2\pi\sigma^2)^{\frac{N}{2}} - \frac{1}{2\sigma^2}(\mathbf{y}-\mathbf{S}\mathbf{g})^T(\mathbf{y}-\mathbf{S}\mathbf{g})\right] =$$

$$= -\frac{1}{2\sigma^2}\frac{\partial}{\partial \mathbf{g}}[\mathbf{y}^T\mathbf{y} - 2\mathbf{y}^T\mathbf{S}\mathbf{g} + \mathbf{s}^T\mathbf{G}^T\mathbf{G}\mathbf{s}] \tag{A.3}$$

Employing the partial derivative identities $\frac{\partial \mathbf{b}^T\mathbf{x}}{\partial \mathbf{x}} = \mathbf{b}$ and $\frac{\partial \mathbf{x}\mathbf{A}\mathbf{x}^T}{\partial \mathbf{x}} = 2\mathbf{A}\mathbf{x}$ for $\mathbf{A}$ symmetric matrix yields

$$\frac{\partial \ln p(\mathbf{y};\mathbf{g})}{\partial \mathbf{g}} = \frac{1}{\sigma_w^2}[\mathbf{S}^T\mathbf{y} - \mathbf{S}^T\mathbf{S}\mathbf{g}] \tag{A.4}$$

$$= \frac{\mathbf{S}^T\mathbf{S}}{\sigma_w^2}[(\mathbf{S}^T\mathbf{S})^{-1}\mathbf{S}^T\mathbf{y} - \mathbf{g}] \tag{A.5}$$

assuming that $\mathbf{S}^T\mathbf{S}$ is invertible. Therefore the MVU estimator of the time-invariant impulse response is

$$\hat{\mathbf{g}} = (\mathbf{S}^T\mathbf{S})^{-1}\mathbf{S}^T\mathbf{y} \tag{A.6}$$

and its covariance matrix is

$$\mathbf{C}_{\hat{\mathbf{g}}} = \sigma_w^2(\mathbf{S}^T\mathbf{S})^{-1} \tag{A.7}$$

The estimator variance depends on the input signal matrix $\mathbf{S}^T\mathbf{S}$. Aiming at minimizing the variance of the MVU estimator, the input vector $\mathbf{s}$ must be chosen to make $\mathbf{S}^T\mathbf{S}$ as near to a diagonal matrix as possible. Given the notation $[\mathbf{S}]_{ij} = s[i-j]$, one can write

$$[\mathbf{S}^T\mathbf{S}]_{ij} = \sum_{n=1} N s[n-i]s[n-j] \qquad i = 1,2,...,p;\ j = 1,2,...,p \tag{A.8}$$

For N large, the approximation bellow is valid and can be seen as a correlation function of the deterministic sequence $s[n]$ of the elements of input vector $\mathbf{s}$.

$$[\mathbf{S}^T\mathbf{S}]_{ij} \approx \sum_{n=0}^{N-1-|i-j|} s[n]s[n-|i-j|] \tag{A.9}$$

Therefore, matrix $\mathbf{S}^T\mathbf{S}$ has now the form of a symmetric Toeplitz autocorrelation matrix. Since the input autocorrelation is given by

$$r_{ss}[k] = \frac{1}{N}\sum_{n=0}^{N-1-k} s[n]s[n+k] \tag{A.10}$$

then one can write

$$\mathbf{S}^T\mathbf{S} = N \begin{bmatrix} r_{ss}[0] & r_{ss}[1] & ... & r_{ss}[p-1] \\ r_{ss}[1] & r_{ss}[0] & ... & r_{ss}[p-2] \\ \vdots & \vdots & \ddots & \vdots \\ r_{ss}[p-1] & r_{ss}[p-2] & ... & r_{ss}[0] \end{bmatrix} \tag{A.11}$$

and for $\mathbf{S}^T\mathbf{S}$ to be diagonal, it is required $r_{ss}[k] = 0 \quad k \neq 0$. In other words, the choice of the probe signal in MVU is concerned with a signal with high autocorrelation and very low cross-correlation.

Appendix B

Derivation of the regularized $\ell 1$-norm estimator

The sparse solution for an under-determined linear system [78] as in (2.9) requires to solve the optimization problem over the $\ell 0$-norm

$$\hat{\mathbf{g}} = \arg \min_{\mathbf{g} \in \mathbb{C}^{J \times 1}} \|\mathbf{g}\|_0 \{s.t.\} \mathbf{y} = \mathbf{S}\mathbf{g} \tag{B.1}$$

under the assumption that the $\mathbf{g}$ is sparse, *i.e.*, if $\|\mathbf{g}\|_0 \ll J$, where J is the length of $\mathbf{g}$ and the $\ell 0$-norm represents the number of non-zero elements in the vector $\mathbf{g}$, that is

$$\|\mathbf{g}\|_0 = \{\#\ of\ n\ :\ h(n) \neq 0\} \tag{B.2}$$

This is a NP-hard problem [79] , whose computational complexity is $O(2^n)$, thus non-practical when n is large. If the signals is sparse ($\|\mathbf{g}\|_0 \ll J$) then the problem is tractable as the solution to

$$\hat{\mathbf{g}} = \arg \min_{\mathbf{g} \in \mathbb{C}^{J \times 1}} \|\mathbf{g}\|_0 \{s.t.\} \|\mathbf{S}\mathbf{g} - \mathbf{y}\|_2 < \epsilon_w \tag{B.3}$$

where $\epsilon_w > 0$ is a threshold error. However, both problems (B.1) and (B.3) are non-convex. In fact, for the ℓp-norm with $0 < p < 1$, the problem belongs to the class of non-convex optimization problems, much harder to solve than convex optimization. Feasibility rules must be observed, obeying criteria as, *e.g.*, the Restricted Isometry defined in [51] as follows:

Definition (Restricted Isometry Constants):
Let F be a matrix with the finite collection of vectors $(v_j)_{j \in J} \in \mathbb{R}^p$ as columns. For

every integer $1 < S < |J|$*, we define the restricted isometry constants to be the smallest quantity* δ_S *such that* F_T *obeys*

$$(1 - \delta_S)\|^2 \leq \|F_T c\|^2 \leq (1 + \delta_S)\|^2 \tag{B.4}$$

for all subsets $T \subseteq J$ *of cardinality at most* S*, and all real coefficients* $(c_j)_{j \in T}$*.*

Aiming at avoiding the difficulty on non-convexity and ensure a unique solution, one can find a suboptimal solution by relaxing the non-convex $\ell 0$-norm into a convex norm. In particular, the interest is in the $\ell 1$-norm since is the smaller norm that is still convex. Thus, relaxing the $\ell 0$-norm to the $\ell 1$-norm, a straightforward suboptimal solution is yielded if RIP is verified. The method that solves the minimization problem is named Basis Pursuit [52], being stated as

$$\hat{\mathbf{g}} = \arg \min_{\mathbf{g} \in \mathbb{C}^{J \times 1}} \|\mathbf{g}\|_1 \{s.t.\} \, \mathbf{y} = \mathbf{S}\mathbf{g} \tag{B.5}$$

Or using sparse approximation to make the problem more tractable as

$$\hat{\mathbf{g}} = \arg \min_{\mathbf{g} \in \mathbb{C}^{J \times 1}} \|\mathbf{g}\|_1 \{s.t.\} \, \|\mathbf{S}\mathbf{g} - \mathbf{y}\|_2 \leq \epsilon_w \tag{B.6}$$

These convex optimization solutions can adopt an interior point method [53] or a greedy algorithm. Greedy pursuit algorithms attempt to find an approximate solution for the sparse optimization problem. They are faster than convex optimization but slightly less precise. Some of the greedy pursuit algorithms are in the family of Matching Pursuit (MP) [80] as, e.g., Orthogonal MP [81], Gradient MP [82] and Compressive Sampling MP [83], among others.

Out of the MP family but also solvable with greedy algorithms are the LARS [54] and LASSO [55]. In particular, LASSO proposes to minimize the least square error subject to the $\ell 1$-norm of the solution vector that should be smaller than some noise threshold ϵ_w, and

it is stated as

$$\hat{\mathbf{g}} = \arg \min_{\mathbf{g} \in \mathbb{C}^{J \times 1}} \|\mathbf{y} - \mathbf{S}\mathbf{g}\|_2^2 \, \{s.t.\} \, \|\mathbf{g}\|_1 < \epsilon_w \tag{B.7}$$

Equation (B.7) can be equivalently rewritten as an unconstrained optimization problem, yielding the core of the RegL1 estimator, that is

$$\hat{\mathbf{g}} = \arg \min_{\mathbf{g}} \{\frac{1}{2}\|\mathbf{S}\mathbf{g} - \mathbf{y}\|_2^2 + \gamma \|\mathbf{g}\|_1\} \tag{B.8}$$

where the scalar γ is a regularization parameter contained in the interval $[0, \infty)$.

A greedy algorithm must update the entries of the solution vector $\mathbf{g}$ by solving a penalized least squares problem, projecting the measurement vector $\mathbf{y}$ onto the space spanned by the active columns of S plus a penalization term. A suitable algorithm to solve this problem, among others options, is the IRLS [56]. Assume $\mathbf{G}$ as a diagonal matrix with $diag(\mathbf{G}) = |\mathbf{g}|$, thus we have $\|\mathbf{g}\|_1 \simeq \mathbf{g}^T \mathbf{G}^{-1} \mathbf{g}$. Note that the ℓ_1-norm is showed here as an adaptively-weighted version of the squared ℓ_2-norm. With this approximation, the estimator is given by

$$\hat{\mathbf{g}} = \arg \min_{\mathbf{g}} \{\gamma \, \mathbf{g}^T \mathbf{G}_{k-1}^{-1} \mathbf{g} + \frac{1}{2}\|\mathbf{S}\mathbf{g} - \mathbf{y}\|_2^2\} \tag{B.9}$$

Appendix C

Outliers sensors blocker

Doppler Spectrum (DS) is defined by the sum over the delay-axis of a Doppler Spreading Function (DSF) [66]. Given the impulse response $h_l[n,k]$ of the $l-th$ channel, the DSF is

$$S_l[\xi,k] = \sum_{n=0}^{N-1} h_l[n,k] e^{-j(2\pi/N)\xi n} \tag{C.1}$$

and the DS is

$$\tilde{S}_l[\xi] = \frac{1}{K} \sum_{k=0}^{K-1} S_l[\xi,k] \tag{C.2}$$

The EPTR is designed to reject sensors with outliers in the DS maximum peak. The rejection is based on verifying if the frequency shift of the DS main peak is within an arbitrary threshold of error on the frequency axis. The thresholds defining the frequency range in this work is set to be one quarter of the whole region available on the frequency axis, centered at zero frequency. The underlying assumption to this choice is that the threshold is expected to be close to zero frequency because an hypothetically perfect time compression/dilation compensation would ideally generate a spectrum without any frequency offset.

Figure C.1 shows, for a signal collected on May 24, the DSF (a) and the DS (b) relative to a sensor whose the signal has successful resampling compensation (hydrophone 7 at 50.1 m depth) and the ill-posed DSF (c) and DS (d) relative to a sensor with failed compensation (hydrophone 16 at 14.1 m depth). One can see that the maximum peak is at almost zero

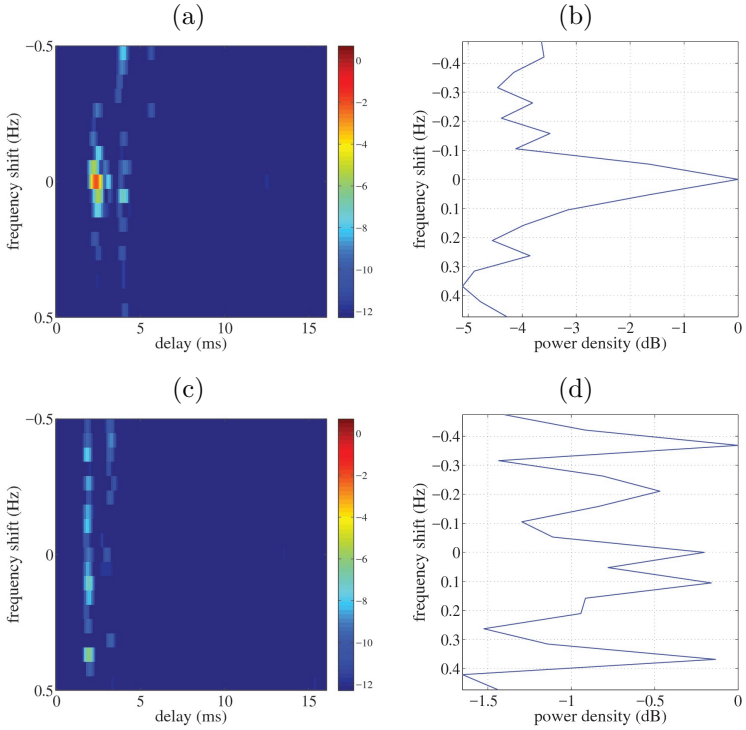

Figure C.1: DSF (a) and the DS (b) relative to a sensor whose the signal has successful resampling compensation (hydrophone 7 at 50.1 m depth). Ill-posed DSF (c) and DS (d) relative to a sensor with failed compensation (hydrophone 16 at 14.1 m depth).

frequency in the sensors with successful compensation and has several undefined strong peaks for the sensor with failed compensation, being its maximum peak out of the thresholded region. This means that, in the latter case, there is still an excessive uncompensated Doppler. Sensors with this characteristics, expected to be in small number, are assumed as outliers and are excluded from PTR processing.

Figure C.2 shows the DS maximum peak of all hydrophones, for the data collected on May 24 (a) and on May 27 (b). The two dashed lines denotes the threshold limiting a quarter of the available frequency in the vertical axis, centered at the zero-frequency. The red circles shows the outliers and the green circles the accepted sensors. One can observe that the hydrophone number 16 at 14.1 m and the hydrophone number 3 at 66.1 m in the Fig. C.2 (a) are the rejected sensors by the outliers blocker due to strong DS peak distortion. All

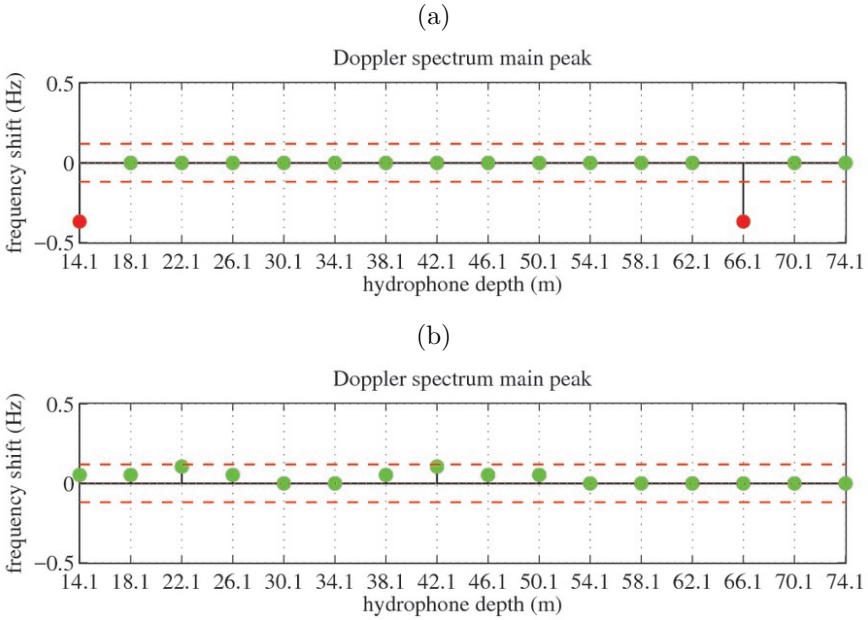

Figure C.2: Outliers rejection for PTR for data collected on May 24 (a) and May 27 (b). Each circle corresponds to the Doppler spectrum maximum peak estimated at each hydrophone. The marks filled with red color denote the outliers and the marks filled with green color denotes the accepted sensors. The two dashed lines shows the thresholds for rejection.

the others sensors have DS peak inside the thresholded frequency region, having sufficiently small frequency shift, thus being accepted to be employed in the PTR processing. Table C.1 shows the number of rejected outliers sensors for each data set.

Table C.1: Blocked sensors per data set in the 16-hydrofones VLA.

Signal ID number	**blocked hyd. PC**	**blocked hyd. RegL1**
241	2 (14.1m and 66.1m)	3 (14.1m, 62.1m and 66.1m)
271	0	0
272	0	0
273	0	0
274	0	0
275	0	1 (hyd. 74.1m)
276	0	1 (hyd. 70.1m)
277	0	0
278	0	0
279	0	0

Appendix D

Bi-static scattering geometry

This appendix is inspired by the bi-static scattering geometry model described in details in [65]. A closed form expression can be derived for a simplified time-variant underwater waveguide with iso-velocity SSP and whose rays connecting source and receiver have a single reflection on boundaries. The scenario is based on the bi-static scattering geometry, from which can be calculated the time compression/stretch factor, the time delay and the Doppler shift expressions. Figure D.1 shows the bi-static scattering geometry, where $R_{o,t}$ is the transmitter-to-scatter-point initial range, R_{o_r} is the scatter-point-to-receiver initial range and $\vec{V}_X \bullet \hat{n}_X$ represents the projection of a given velocity vector ($\vec{V}_t$, $\vec{V}_r$ or $\vec{V}_s$) in the propagation path direction. The corresponding unitary vectors are represented by $\hat{n}_t$ and $\hat{n}_r$.

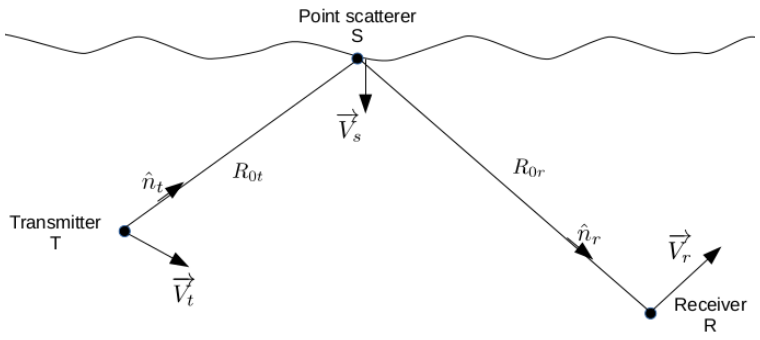

Figure D.1: Bi-static scattering geometry. The transmitter, the point scatterer and the receiver are moving with constant velocity.

The complex envelop of a passband signal transmitted in the scenario of bi-static scat-

tering geometry, at which there are source motion, receiver motion and scatter point motion with constant velocity, is given by [65]

$$y(t) = s(\alpha(t - \tau_A))e^{j2\pi\Phi_A t} \tag{D.1}$$

where the compression/stretch factor is α, the Doppler frequency shift is Φ_A and τ_A denotes the time delay after the ray travel from the source to the receiver. They are defined as follows

$$\alpha = \frac{(1 - \vec{V}_s \bullet \frac{\hat{n}_t}{c})(1 - \vec{V}_r \bullet \frac{\hat{n}_r}{c})}{(1 - \vec{V}_s \bullet \frac{\hat{n}_r}{c})(1 - \vec{V}_t \bullet \frac{\hat{n}_t}{c})} \tag{D.2}$$

The time delay is given by

$$\tau_A = \frac{\frac{1 - \vec{V}_s \bullet \frac{\hat{n}_r}{c}}{1 - \vec{V}_s \bullet \frac{\hat{n}_t}{c}} R_{o,t} + R_{o,r}}{(1 - \vec{V}_r \bullet \frac{\hat{n}_r}{c})c} \tag{D.3}$$

and Doppler frequency shift is

$$\Phi_A = -(1 - \alpha)f_c \tag{D.4}$$

where the sound speed in the medium is c, the carrier frequency is f_c and the symbol $\bullet$ denotes dot product.

For more concise formulation, consider the compression/stretch factor redefined as $\beta = \alpha - 1$ and substitute Φ_A in (D.2), which yields

$$y(t) = s((1 + \beta)(t - \tau_A))e^{j2\pi f_c \beta t} \tag{D.5}$$

Thus, the received signal, after disregard the travel time under the assumption of perfect synchronization, is

$$y(t) = s((1 + \beta)t)e^{j2\pi f_c \beta t}; \tag{D.6}$$

where the compression/stretch factor β is

$$\beta = \frac{(1 - \vec{V}_s \bullet \frac{\hat{n}_t}{c})(1 - \vec{V}_r \bullet \frac{\hat{n}_r}{c})}{(1 - \vec{V}_s \bullet \frac{\hat{n}_r}{c})(1 - \vec{V}_t \bullet \frac{\hat{n}_t}{c})} - 1 \tag{D.7}$$

Extension to a short range isovelocity SSP time-variant waveguide

The bi-static scattering geometry model can be extended to a short range time-variant waveguide with one reflected path for each boundary. This is an attractive procedure since the scenario is similar to a simplified shallow water waveguide with nearly isovelocity SSP and single reflection in the boundaries. Figure D.2 shows the simplified waveguide scenario. The

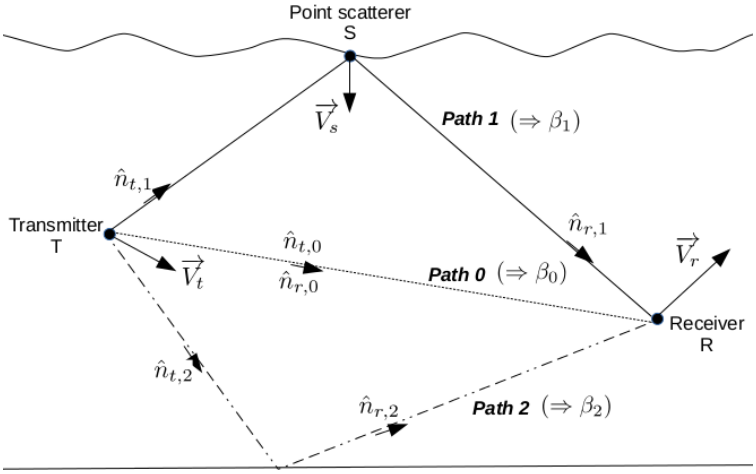

Figure D.2: A simplified underwater waveguide with isovelocity SSP and single reflection in the boundaries.

path 0 is the direct, the path 1 is surface-reflected and the path 2 is bottom-reflected. The time-variant CIR in baseband equivalent representation, assuming the approach described in [14], is given by

$$h(t,\tau) = \sum_p \frac{1}{1+\beta_p} A_p \delta\left(\frac{\tau + \beta_p t - D_p}{1+\beta_p}\right) e^{j2\pi f_c \frac{\beta_p}{1+\beta_p}(t-\tau)}; \quad p = 0,1,2. \tag{D.8}$$

where A_p denotes path gain and D_p denotes path delay, which can be appropriately computed using a ray tracing model. The complex envelope of the received signal after cross the time-variant waveguide with equivalent baseband impulse response $h(t,\tau)$ is

$$y(t) = \int s(t-\tau)h(t,\tau)d\tau \tag{D.9}$$

where $s(t)$ is the complex envelope of the transmitted signal.

Depending of the path type, the compression/stretch factor for the direct path (β_0), the surface-reflected path (β_1) and bottom-reflected path (β_2) are, respectively, given by

$$\beta_0 = \frac{1 - \vec{V}_r \bullet \frac{\hat{n}_{R,0}}{c}}{1 - \vec{V}_t \bullet \frac{\hat{n}_{R,0}}{c}} - 1 \tag{D.10}$$

$$\beta_1 = \frac{(1 - \vec{V}_s \bullet \frac{\hat{n}_{T,1}}{c})(1 - \vec{V}_r \bullet \frac{\hat{n}_{R,1}}{c})}{(1 - \vec{V}_s \bullet \frac{\hat{n}_{R,1}}{c})(1 - \vec{V}_t \bullet \frac{\hat{n}_{T,1}}{c})} - 1 \tag{D.11}$$

$$\beta_2 = \frac{1 - \vec{V}_r \bullet \frac{\hat{n}_{R,2}}{c}}{1 - \vec{V}_t \bullet \frac{\hat{n}_{T,2}}{c})} - 1 \tag{D.12}$$

In the particular case of assuming a moving source with constant velocity $\vec{V}_t$, an static array ($\vec{V}_r = \vec{0}$) and flat static surface ($\vec{V}_s = \vec{0}$), the factor β_p, where p represents the path, becomes

$$\beta_p = \frac{1}{1 - \vec{V}_t \bullet \frac{\hat{n}_{t,p}}{c}} - 1 \qquad \Rightarrow \quad \beta_p = \frac{1}{1 - \frac{\|\vec{V}_t\| cos\theta_p}{c}} - 1 \tag{D.13}$$

where θ_p is the launching angle of the path relative to the source velocity direction.

Since each path have a different β_p, it results that each path is affected by a different amount of Doppler.

Bibliography

[1] M. Stojanovic, "Underwater Acoustic Communication," tech. rep., Northeastern University, Department of Electrical and Computing Engineering, 1998.

[2] R. Derecin, "Radio Communications of German U-boats in WWI and WWII." `http://uboat.net/articles/index.html?article=35`. Accessed 2017-06-28.

[3] G. Louis A, "Evolution of naval radio-electronics and contributions of the naval research laboratory." `http://www.navy-radio.com/xmtr-vlf.htm`, 1979. Accessed 2017-07-08.

[4] "Underwater Electromagnetic Propagation." `https://www.hydro-international.com/content/article/underwater-electromagnetic-propagation`. Accessed 2017-06-29.

[5] "Optical Communications, Woods Hole Oceanographic Institution." `http://www.whoi.edu/website/optical-communications`. Accessed 2017-06-29.

[6] N. Fair, A. Chave, L. Freitag, J. Preisig, S. White, D. Yoerger, and F. Sonnichsen, "Optical modem technology for seafloor observatories," in *IEEE/MTS Oceans*, pp. 1–6, 2006.

[7] M. Doniec, I. Vasilescu, M. Chitre, C. Detweiler, M. Hoffmann-Kuhnt, and D. Rus, "Aquaoptical: A lightweight device for high-rate long range underwater point-to-point

communication," in *IEEE/MTS Oceans*, pp. 1–6, 2009.

[8] "Woods Hole Oceanographic Institution (WHOI), Optical Communications." `https://www.sonardyne.com/product/bluecomm-underwater-optical-communication-system`. Accessed 2017-06-29.

[9] M. Doniec and D. Rus, "Bidirectional optical communication with aquaoptical ii," in *IEEE International Conference on Communication Systems*, pp. 390–394, 2010.

[10] B.Li, J. Huang, K. Ball, M. Stojanovic, L. Freitag, and P. Willett, "Mimo-ofdm for high rate underwater acoustic communications," *IEEE Journal of Oceanic Engineering*, vol. 34, pp. 634–644, 2009.

[11] J. G. Proakis, *Digital Communications*. McGraw Hill, 2008.

[12] D. Jackson and D. Dowling, "Phase conjugation in Underwater acoustics," *Journal of Acoustical Society of America*, no. 89, pp. 171–181, 1991.

[13] D. Roussef, J. Flynn, J. Ritcey, and W. Fox, "Acoustic communication using time-reversal signal processing: spatial and frequency diversity," in *High frequency ocean acoustics* (M. Porter, M. Siderius, and W. Kuperman, eds.), American Institute of Physics, AIP, 2004.

[14] J. Gomes, A. Silva, and S. Jesus, "Adaptive spatial combining for passive time-reversed communications," *Journal of Acoustical Society of America*, pp. 1038–1053, August 2008.

[15] R. G. Baraniuk, "Compressive sensing," *IEEE Signal Processing Magazine*, pp. 119–124, July 2007.

[16] E. Candes and J. Romberg, "Sparsity and incoherence in compressive sampling," *Inverse Problems I.O.P. Publishing*, pp. 969–985, July 2007.

[17] D. W. Painter, "Underwater acoustic communications," *Oceanology International, Naval Engineers Journal*, vol. 3, pp. 1980–1983, July 1968.

[18] J. G. Proakis and M. Salehi, *Contemporary Communication Systems Using MATLAB*. PWS Publishing Company, 1998.

[19] W. A. Kuperman, W. Hodgkiss, H. C. Song, T. Akal, C. Ferla, and D. R. Jackson, "Phase conjugation in the ocean: Experimental demonstration of an acoustic time-reversal mirror," *Journal of Acoustical Society of America*, vol. 102, pp. 1–16, December 1998.

[20] S. Hinedi and W. Lindsey, "ISI effects on BPSK and QPSK carrier tracking loops," *IEEE Transactions on Communications*, vol. COMM 39, pp. 1255–1265, August 1991.

[21] M. Stojanovic, J. A. Catipovic, and J. G. Proakis, "Phase Coherent-Digital Communications for Underwater Acoustic Channels," *IEEE Journal of Oceanic Engineering*, vol. v. 19, January 1994.

[22] A. Silva, S. Jesus, and V. Barroso, "Underwater acoustic communication unsing a virtual electronic time reversal mirror approach," in *V European Conference on Underwater Acoustics - Lyon, France* (P. Chevret and M. Zakharia, eds.), 2000.

[23] D. Rouseff, D. Jackson, W. Fox, C. Jones, J. Ritcey, and D. Dowling, "Underwater acoustic communications by passive-phase conjugation: Theory and experimental results," *IEEE Journal of Oceanic Enginnering*, vol. 26, no. 4, pp. 821–831, 2001.

[24] G. F. Edelmann, T. Akal, W. S. Hodgkiss, K. Seongil, W. A. Kuperman, and S. H. Chun, "An initial demonstration of underwater acoustic communication using time reversal," *IEEE Journal of Oceanic Enginnering*, no. 27, pp. 602–609, 2002.

[25] G. Zhang, "Coherent underwater communication using passive time reversal over multipath channels," *Journal Elsevier Physical Communications*, vol. 72, pp. 412–9, 2011.

[26] J. Gomes, A. Silva, and S. Jesus, "Joint passive time reversal and multichannel equalization for underwater communications," in *IEEE/MTS OCEANS*, pp. 1–6, 2006.

[27] M. Quinteros, E. Kaminski, and K. Cartwright, "A trellis-coded modulation scheme with a novel expanded 16-dimensional constant envelope qpsk constellation," in *IEEE GLOBECOMM 09*, 2009.

[28] T. C. Yang, "Environmental effects on phase coherent underwater acoustic communications: a perspective from several experimental measurements," in *High frequency ocean acoustics* (M. S. M. Porter and W. Kuperman, eds.), American Institute of Physics, 2004.

[29] M. Stojanovic, J. Catipovic, and J. G. Proakis, "Adaptive multichannel combining and equalization for underwater acoustic communications," *Journal of Acoustical Society of America*, vol. 94, pp. 1621–1631, September 1993.

[30] A. Song, M. Badiey, and V. McDonald, "Multichannel combining and equalization for underwater acoustic mimo channels," in *IEEE/MTS Oceans'08*, 2008.

[31] H. C. Song, W. A. Kuperman, W. S. Hodgkiss, T. Akal, and C. Ferla, "Iterative time reversal in the ocean," *Journal of Acoustical Society of America*, vol. 105, pp. 3176–3184, June 1999.

[32] A. Silva, *Environmental-based underwater communications*. PhD thesis, Instituto Superior Técnico da Universidade Técnica de Lisboa, 2009.

[33] M. Stojanovic, "Retrofocusing techniques for high rate acoustic communications," *Journal of Acoustical Society of America*, vol. 117, no. 3, pp. 1183–1185, 2005.

[34] S. Siddiqui, "Arrival-based equalizer for underwater communication systems," Master's thesis, University of Algarve, 2012.

[35] S. Kay, *Fundamentals of Statistical Signal ProcesTheory, Estimation Theory*, vol. 1. Prentice Hall, 1993.

[36] M. J. Hinich, "Maximum-likelihood signal processing for a vertical array," *Journal of Acoustical Society of America*, vol. 54, pp. 499–503, 1973.

[37] C. Clay, "Optimum time domain signal transmission and source location in a waveguide," *Journal of Acoustical Society of America*, 1987.

[38] A. Tolstoy, *Matched Field Processing for Underwater Acoustics*. Singapore: World Scientific, 1993.

[39] A. B. Baggeroer, W. A. Kuperman, and P. N. Mikhalevsky, "An overview of matched field methods in ocean acoustics," *IEEE Journal of Oceanic Engineering*, vol. 18, pp. 401–424, October 1993.

[40] W. Munk and C. Wunsch, "Ocean acoustic tomography: A scheme for large scale monitoring," *Deep Sea Research*, vol. 26, no. A, pp. 123–161, 1979.

[41] W. Munk, P. Worcester, and C. Wunsch, *Ocean Acoustic Tomography*. Cambridge Monographs on Mechanics, 1995.

[42] Z. H. Michalopoulou, "Robust multi-tonal matched-field inversion: A coherent approach," *Journal of Acoustical Society of America*, vol. 104, pp. 160–170, 1998.

[43] M. D. Collins and W. A. Kuperman, "Focalization: environmental focusing and source localization," *Journal of Acoustical Society of America*, vol. 90, pp. 1410–1422, September 1991.

[44] N. E. Martins, *Acoustic-oceanographic data fusion for prediction of oceanic acoustic fields*. PhD thesis, Faculty of Sciences and Technology, University of Algarve, 2014.

[45] E. L. Hamilton, "Geoacoustic modeling of the sea floor," *Journal of the Acoustical Society of America*, vol. 68, pp. 1313–1340, 1980.

[46] M. B. Porter, *The BELLHOP Manual and Users Guide*. Heat, Light, and Sound Research, Inc., La Jolla, CA, USA, January 2011.

[47] M. B. Porter, "The KRAKEN normal mode program," Tech. Rep. SM–245, SACLANTCEN Undersea Research Centre Memorandum, La Spezia, Italy, September 1991.

[48] S. Jesus and A. Silva, "Time reversal and spatial diversity: issues in a time varying geometry testing," in *Conference on High Frequency Ocean Acoustics*, (San Diego, USA), March 2004.

[49] O. Taheri and S. Vorobyov, "Reweighted l1-norm penalized lms for sparse channel estimation and its analysis," *Signal Processing Journal*, pp. 70–79, November 2014.

[50] E. Candes and M. Wakin, "An introduction to compressive sampling," *IEEE Signal Processing Magazine*, pp. 21–30, March 2008.

[51] E. Candes and T. Tao, "Decoding by linear programming," *IEEE Transactions on Information Theory*, vol. 51, pp. 4203–4215, March 2005.

[52] S. Chen, D. Donoho, and M. Saunders, "Atomic decomposition by basis pursuit," *SIAM Journal on Scientific Computing*, vol. 20, no. 1, pp. 33–61, 1998.

[53] S. Boyd and L. Vandenberghe, *Convex Optimization*. Cambridge University Press, 2004.

[54] R. Tibshirani, T. Hastie, I. Johnstone, and B. Efron, "Least angle regression," *The Annals of Statistics*, vol. 32, pp. 407–451, April 2004.

[55] R. Tibshirani, "Regression shrinkage and selection via the lasso," *Journal of the Royal Statistical Society*, vol. 58, no. 1, pp. 267–288, 1996.

[56] J. A. Barreto and C. S. Burrus, "Complex approximation using iterative reweighted least squares for fir digital filters," in *In Proceedings of the IEEE International Conference on Acoustics, Speech, and Signal Processing*, vol. 3, (Adelaide, Australia), pp. 545–548, IEEE ICASSP-94, April 1994.

[57] M. Lanzagorta, *Underwater Communications*. No. 6, Morgan and Claypool, 2013.

[58] F. B. Jensen, W. A. Kuperman, M. B. Porter, and H. Schmidt, *Computational Ocean Acoustics*. 2nd Edition, Series in Modern Acoustics and Signal Processing, Springer, NY, 2011.

[59] " - HLS Research, U.S. Office of Naval Research." `http://oalib.hlsresearch.com`. Accessed 2017-06-06.

[60] "Signal Processing Laboratory - University of Algarve." `http://www.siplab.fct.ualg.pt`. Accessed 2017-06-06.

[61] M. Chitre, "A high-frequency warm shallow water acoustic communications channel model and measurements," *Journal of Acoustical Society of America*, vol. 122, pp. 2580–2586, November 2007.

[62] R. Mellen, "On underwater sound scattering by surface waves," *IEEE Journal of Oceanic Engineering*, vol. 14, July 1989.

[63] A. Jones, J. Sendt, A. Duncan, P. Clarke, and A. Maggi, "Modelling the acoustic reflection loss at the rough ocean surface," in *ACOUSTICS 2009*, 2009.

[64] O. Rodriguez, A. Silva, J. P. Gomes, and S. Jesus, "Modeling arrival scattering due to surface roughness," in *10th European Conference on Underwater Acoustics*, 2010.

[65] L. J. Ziomek, *Fundamentals of Acoustic Field Theory and Space-Time Signal Processing*. CRC, 1995.

[66] R. O. P. van Walree, T. Jenserud, "Stretched-exponential doppler spectra in underwater acoustic communication channels," *Journal of Acoustical Society of America - Express Letters*, vol. 128, September 2010. Norwegian Defence Research Establishment.

[67] M. Stojanovic, M. Zakharia, J. Chantillon, R. Istepanian, H. Sari, and B. Woodward, *Underwater Acoustic Digital Signal Processing and Communication Systems*. Kluwer Academic Publishers, 2002.

[68] G. M. Wentz, "Acoustic ambient noise in the ocean: Spectra and sources," *Journal of Acoustical Society of America*, vol. 34, pp. 1936–1956, October 1962.

[69] C. Soares, *Broadband Matched-field tomography using simplified acoustic systems*. Faro, Portugal: PhD thesis, Universidade do Algarve, 2007.

[70] V. Meyer and C. Audoly, "A comparison between experiments and simulation for shallow water short range acoustic propagation," in *IEEE International Cogress on Sound and Vibration*, pp. 1–8, DCNS Research, 2017.

[71] O. C. Rodriguez and A. J. Silva, *The Time Variable Acoustic Propagation Model (TV-APM)*. Signal Processing Laboratory, FCT, Universidade do Algarve, http://www.siplab.fct.ualg.pt/tvapm.shtml, May 2012.

[72] A. Caiti, K. Grythe, J. M. Hovem, S. M. Jesus, A. Lie, A. Munafò, T. A. Reinen, A. Silva, and F. Zabel, "Linking Acoustic Communications and Network Performance: Integration and Experimentation of an Underwater Acoustic Network," *IEEE Journal of Oceanic Engineering*, vol. 38, pp. 758–771, October 2013.

[73] CINTAL, "Wp4 deliverable 4.3 hardware prototype," tech. rep., University of Algarve, March 2010.

[74] T. Husoy, M. Pettersen, B. Nilsson, T. Oberg, N. Warakagoda, and A. AbdiLie, "Implementation of an underwater acoustic modem with network capability," in *IEEE Oceans Conference*, (Spain), April 2011.

[75] C. Soares, S. M. Jesus, and E. Coelho, "Environmental inversion using high-resolution matched-field processing," *Journal of Acoustical Society of America*, vol. 122, no. 6, pp. 3391–3404, 2007.

[76] S. E. Dosso and P. Zakarauskas, "Matched-field inversion for source location and equivalent bathymetry," in *Full Field Inversion Methods in Ocean and Seismo-Acoustics (H. Diachok, O. and Caiti, A. and Gerstoft, P. and Schmidt, ed.)*, vol. 12 of *Modern approaches in geophysics*, Springer Netherlands, 1995.

[77] D. Kilfoyle and A. Baggeroer, "The state of the art in underwater acoustic telemetry," *IEEE Journal of Oceanic Engineering*, vol. 25, January 2000.

[78] D. Donoho, Y. Tsaig, I. Drori, and J. Starck, "Sparse solution of underdetermined systems of linear equations by stagewise orthogonal matching pursuit," *IEEE Transactions on Information Theory*, vol. 58, pp. 1094–1121, February 2012.

[79] G. Murthy, "Optimization of quadratic forms: Np hard problems," in *International Symposium on Computational and Business Intelligence*, (New Delhi, India), July 2013.

[80] S. Mallat and Z. Zhang, "Matching pursuits with time-frequencydictionaries," *IEEE Transactions on Signal Processing*, vol. 41, pp. 3397–3415, December 1993.

[81] Y. Pati, R. Rezaiifar, and P. Krishnaprasad, "Orthogonal matching pursuit: recursive function approximation with applications to wavelet decomposition," in *The Twenty-Seventh Asilomar Conference on Signals, Systems and Computers*, November 1993.

[82] T. Blumensath and M. Davies, "Gradient pursuits," *IEEE Transactions on Signal Processing*, vol. 56, pp. 2370–2382, June 2008.

[83] D. Needell and J. Tropp, "Cosamp: Iterative signal recovery from incomplete and inaccurate samples," *Applied and Computational Harmonic Analysis*, vol. 26, pp. 301–321, May 2009.